Max-Planck-Institut
für Plasmaphysik

Abschlussarbeit im Masterstudiengang Physik

Non-Linear MHD Simulations of Mode Locking and Disruption Onset in Tokamaks

Fabian Wieschollek

15. März 2019

Erstgutachterin: Prof. Dr. Sibylle Günter
Zweitgutachter: Dr. Stefan Recksiegel
Betreuer: Dr. Matthias Hölzl

Technische Universität München
Fakultät für Physik

durchgeführt am Max-Planck-Institut für Plasmaphysik,
Garching bei München

Abstract

Disruptions are events that occur in tokamak experiments, which lead to the loss of magnetic confinement within a fraction of a second. As a precursor, usually large magnetic islands are formed as a result of neoclassical tearing modes, which stop rotating by locking to conducting structures, overlap and enforce a stochastisation of the field lines. Both islands and stochastisation lead to a strong radial heat transport, which flattens the temperature profile. Enhanced by further effects like impurity background radiation, the temperature of the whole plasma drops, often to the order of a few electronvolt. Due to this so called "thermal quench", the plasma resistivity increases and the plasma current decays, which is referred to as the "current quench". The consequences of disruptions are massive heat loads, mechanical loads during vertical displacement events or the generation of relativistic runaway electrons which threaten wall components and supporting structures. Therefore, disruptions are a major concern for tokamak experiments and require a more detailed understanding, to improve predictions of disruption dynamics in ITER and future reactors and to develop possible mitigation and avoidance strategies.

In this thesis, simulations of several aspects, crucial for the understanding of the disruption onset are carried out for the first time with the non-linear magnetohydrodynamics code JOREK-STARWALL in realistic tokamak X-Point geometry. Since disruptions predictions require a precise interpretation of diagnostic signals, firstly virtual diagnostic coils are built into the code and used to analyse the signals of a typical magnetic island.

Secondly, the evolution of a $(2/1)$ neoclassical tearing mode into a partial thermal quench is investigated in detail. This involves the study of mode coupling by toroidicity induced effects as well as by non-linear terms in the equations. The onset of stochastisation by island overlapping and the influence of simplified conducting structures onto the mode dynamics is investigated. The resulting impact onto the evolution of the temperature is studied in comparison to theoretical predictions of the anisotropic heat transport in a plasma with magnetic islands and stochastic layers, as well as to experimental observations. The amplitude evolution of the $(2/1)$ mode is compared to empirical experimental predictions for the threshold of thermal quench onset and possible improvements for this empirical description are discussed.

As third part of this thesis, a plasma unstable against a $(2/1)$ mode and additionally exhibiting a slow poloidal rotation is considered. The locking mechanism with the vacuum vessel, during which a rotating magnetic island comes to rest in the lab frame, is studied and compared to theoretical predictions.

Contents

1. Introduction

After the formulation of special relativity which pointed out the equivalence of matter and energy and first nuclear physics experiments in the beginning of the last century, different approaches have been carried out for a civil use of these findings since the end of 1940s. While energy production by the fission of heavy nuclei has reached commercial breakthrough decades ago, nuclear fusion is still a field of ongoing research. Magnetic confinement fusion within the tokamak is currently the most developed and promising concept. However, the tokamak concept still has some serious open issues to be resolved, which need extensive theoretical and experimental investigation in order to qualify the concept for a commercial power plant. One such issue are disruption events, in which the plasma confinement is lost in within fractions of a second, ending the fusion process immediately. In this thesis, simulations are carried out with a magnetohydrodynamics model for the onset and evolution of so called locked-mode disruptions to enhance the understanding of the involved physical processes.

This introduction will at first give a short overview of the nuclear physics relevant for fusion energy and the basic properties of the plasma state. The tokamak and its features are presented in 1.3. Next, a review of the disruptive instability, its underlying causes, consequences, and mitigation or avoidance techniques is given. The chapter closes with a summary of the objectives of this thesis.

1.1. Basics of nuclear fusion research

A sufficient estimate of the interacting forces between protons and neutrons inside an atomic nucleus is given by the Bethe-Weizsäcker-formula.[87] It leads to the fact, that the binding energy per nucleon is the highest for $^{56}\mathrm{Fe}$. Therefore, the fission of nuclei as well as the fusion of lighter nuclei will give rise of a net energy release. A possible reaction is given by the fusion of Deuterium and Tritium:

$$\mathrm{D} + \mathrm{T} \rightarrow {}^{4}\mathrm{He} + \mathrm{n} + 17.6\,\mathrm{MeV} \tag{1.1}$$

In total, $17.6\,\mathrm{MeV}$ is released in the form of kinetic energy of the products. However, the fusion of the two elements requires a significant overlapping of their wave functions, which requires the overcoming of their Coulomb Barrier. The cross-section for DT-fusion reaches a maximum for a center-of-mass energy of $64\,\mathrm{keV}$. A naive approach of shooting a beam of Deuterium with $64\,\mathrm{keV}$ onto a resting Tritium target would not lead to a sufficient fusion rate, since the competing elastic Coulomb collisions would dominate the fusion reactions. A solution is given by heating up both species to the plasma state and confining them over long time scales. The particle energy distribution will then be Maxwellian and the quantity determining the likelihood of the fusion process is the reaction rate $\langle \sigma v^2 \rangle$, where $\langle ... \rangle$ is the averaging over velocity space. The maximum of fusion rate is reached at about $10\,\mathrm{keV}$, which corresponds to a plasma temperature of about a hundred million Kelvin.

An efficient fusion rate requires not only the high temperature as pointed out above but also a sufficiently large confinement time. Otherwise energy and particles are lost before fusions process have taken place. The confinement of a plasma is possible by magnetic fields.

1.2. Properties of a plasma

On the contrary to classical states, there is no distinct phase transition from gas to plasma. Instead it is convenient to define the degree of ionization of a gas α, which is strongly dependent on temperature T and also the ionization energy W_{ion}:

$$\alpha = \frac{n_i}{n_n} \propto \frac{T^{3/2}}{n_i} \exp^{-W_{\mathrm{ion}}/T} \tag{1.2}$$

For α of a few percent, the plasma properties discussed below already dominate and one speaks of a plasma instead of a gas. So, unless fully ionized a plasma consists of ions, electrons and neutrals. A magnetic fusion hydrogen plasma has a typical density of about $n_e \sim 10^{20}\mathrm{m}^{-3}$ and is fully ionized already for $T \lesssim 100\,\mathrm{eV}$. By decreasing the temperature below $W_{\mathrm{ion}} \sim 10\,\mathrm{eV}$, recombination dominates and the plasma falls back into the gaseous state.

Debye shiedling If the density of free electrons in the plasma is sufficient high they will shield the Coulomb Potentials of the much slower moving ions. Their effective "Debye-Hückel" potentials decreases exponentially as a consequence, on a length scale of the Debye length $\lambda_D \approx 7.43\sqrt{\frac{\epsilon_0 T}{e^2 n_e}}$. Because of that a plasma of volume $L^3 \gg \lambda_D^3$ appears to be quasi neutral on a macroscopic scale. The condition for quasi neutrality is that the time averaged number of electrons within the Debye Sphere around each ion is much greater than one: $n_e 4/3\pi\lambda_D^3 \gg 1$.

Magnetized plasma Consisting of charged particles, a plasma interacts with electromagnetic fields. If its motion is heavily influenced by that field it is called a magnetized plasma. While particles can still move freely parallel to (homogeneous) magnetic field lines, its perpendicular motion is restricted by the Lorentz forces. In fact particles rotate with the gyration frequency $\omega_c = q_\alpha B/m_\alpha$, where $\alpha \in e, i$ around the field lines on circles of the Lamour radius $\rho_L = \frac{\sqrt{2m_\alpha T}}{|q_\alpha|B}$ in average. The centre of that circular trajectories is called the guiding centre.

Particle drifts If an external force $\vec{F}$ is applied perpendicular the magnetic field, the position of the guiding centre will drift away perpendicular both to force and magnetic field. This drift velocity is given by:

$$\vec{v} = \frac{1}{q_\alpha}\frac{\vec{F}\times\vec{B}}{B^2} \tag{1.3}$$

If the force field corresponds to an applied external electric field, (1.3) reduces to the charge independent "E-cross-B" drift:

$$\vec{v}_E = \frac{\vec{E}\times\vec{B}}{B^2} \tag{1.4}$$

An inhomogeneity of $\vec{B}$ also leads to a drift:

$$\vec{v}_{\nabla B} = \frac{K_\perp}{qB}\frac{\vec{B}\times\nabla B}{B^2}, \quad K_\perp = \frac{1}{2}mv_\perp^2 \tag{1.5}$$

In terms of magnetohydrodynamics (see 2.1), where the plasma pressure has been defined, the diagmagnetic drift can be described. It is not an actual drift of particles but results in a variation of the net fluid velocities or densities:

$$\vec{u}_D = -\frac{\nabla p \times \vec{B}}{qnB^2} \tag{1.6}$$

For more informations about plasma physics, see for example [20].

1.3. Magnetic confinement in a tokamak

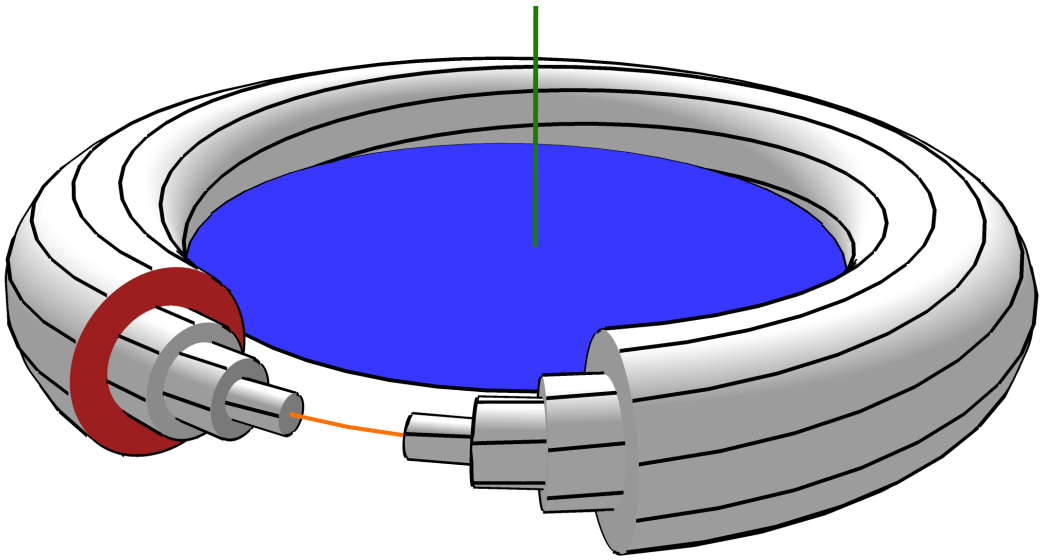

Figure 1: Schematic sketch of flux surfaces within a tokamak. Black lines represent the helical field lines on some flux surfaces (white). Flux Ψ of the uttermost flux surface is defined as the flux going through the blue area, while flux Φ is defined by the red area. The magnetic axis is marked in orange. The central solenoid lies on the torus axis (green).

The aforementioned homogeneous magnetic field lines restrict the motion of charged particles well in the perpendicular plane but can not limit the spatial expansion of a plasma in parallel direction. The approach followed in today's large scale experiments to overcome this problem is to make use of toroidal magnetic configurations. However a configuration consisting only of planar field coils generating a purely toroidal field would not lead to confinement: Because of divergence freeness of the magnetic field, $\nabla \cdot B_\phi = 0$, it decreases radially[1] with $B_\phi \approx 1/R$. This would give rise to a gradient-B drift which drives a charge separation in Z direction in turn. Obviously an incipient E-cross-B drift pointing outwards in R direction will force the plasma to move out of the configuration. The confinement would be lost within a fraction of a second.

[1] Coordinates and some definitions used in the course of this thesis are listed in Appendix A

The charge separation, however, can be avoided by an additional magnetic field B_θ in poloidal direction. Superposition of B_ϕ and B_θ yields helical field lines. In a tokamak, B_θ is mostly produced by the toroidal plasma current I_P. The generation of helical field lines using non-planar field coils, is a main feature of the stellarator concept which is being under development in parallel to tokamak devices. The classical tokamak concept builds up I_P by induction: The plasma behaves as a secondary coil of a transformer with only one winding while a primary coil is installed next. The central solenoid out of a ferromagnetic material that transports the time varying magnetic flux into the machine is therefore a crucial component.

The high turns ratio makes the amplification of the primary current to $I_P \sim 1\,\mathrm{MA}$ possible. Since inductive currents only sustain as long as the current on the primary side keeps changing classical tokamaks enable pulsed-mode operation only. Pulses are usually in order of seconds. Concepts of making use of neoclassical currents presented in 2.2.3 in a different context are under investigation as well as other current drive techniques, e.g. by electromagnetic waves.

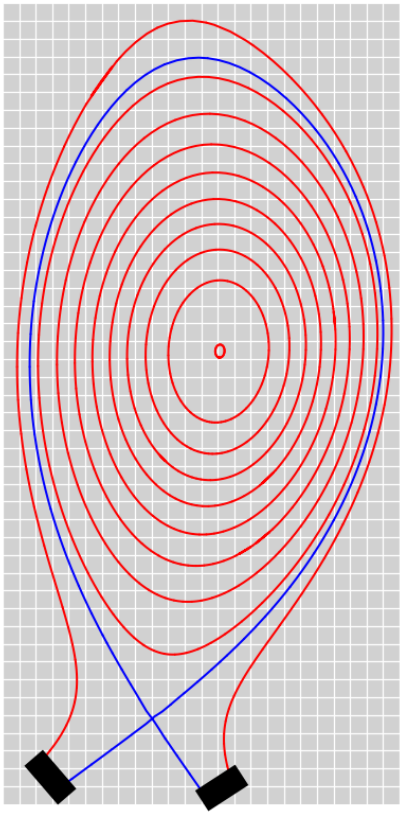

Figure 2: Poloidal cross section of flux surfaces of a plasma in divertor configuration. The plasma is divided by the separatrix (blue) into the inner region of closed magnetic field lines and the outer region of open field lines. Field lines outside the separatrix hit the divertor plates (black).

The helical field lines form nested toroidal flux surfaces. The perpendicular component of the magnetic field through a surface in the toroidal plane enclosed by a flux surface (see figure 1), B_θ, determines the poloidal flux Ψ assigned to that flux surface. An analogous definition applies for the toroidal flux Φ and B_ϕ. The safety factor[23] q, which is the ratio of the number of toroidal turns of a field line per poloidal turns, is then defined as:

$$q = \frac{\mathrm{d}\Phi}{\mathrm{d}\Psi} \approx \frac{rB_\phi}{RB_\theta} \tag{1.7}$$

The approximation holds if B_ϕ and B_θ are about constant on a flux surface.

If q is a rational number, $q = n/m$ the field lines close in themselves and the corresponding flux surface is called rational or resonant surface (n/m). The central poloidal axis of the tokamak, where B_θ vanishes is called the magnetic axis. The safety factor close to the magnetic axis is usually referred as q_0.[2] Further details of the magnetic field configuration were summarized by Boozer [7, Chapter III].

The magnetic configuration explained above is also called the circular tokamak. Improvements in operation performance suggested a shaping of the poloidal cross section of the flux

[2] Further definitions describing a plasma configuration that are used within this thesis are listed in Appendix A

surfaces, so that it differs from the cylindrical shape. The shaping is realized by an additional poloidal magnetic field. One common configuration is the divertor plasma (see figure 2). More details about tokamaks can be found in [90].

Like all magnetic confinement concepts which have been developed, the tokamak too is prone to plasma instabilities of various kinds. An instability is a self-reinforcing perturbation or "mode" caused by an arbitrary small force acting on a plasma in equilibrium. Many instabilities can be described well by the magnetohydrodynamics (MHD) description and therefore are classified as MHD instabilities. As long as a perturbation is small the problem can be linearised and treated using an energy principle similar to minimization of the potential energy of a system in classical mechanics[4],[22].

1.4. The disruption

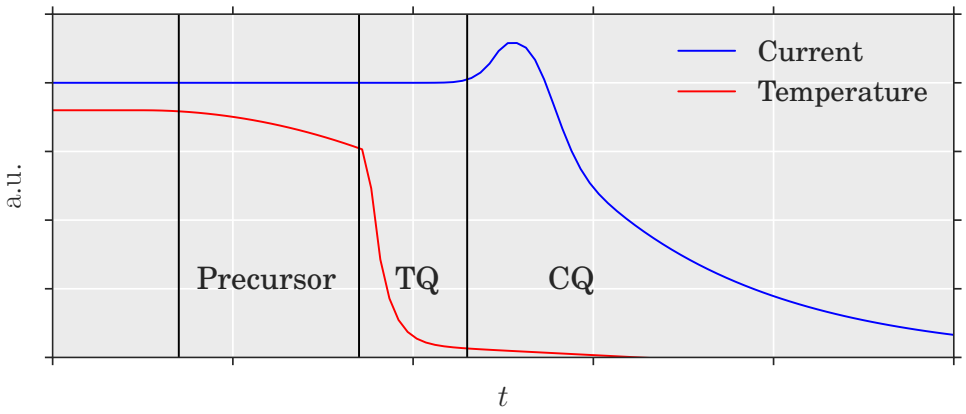

Figure 3: Schematic sequence of events during a disruption.

The disruptive instability commonly known just as a disruption is the complete loss of the energy and magnetic confinement of the plasma within the order of a few milliseconds to about one second. The nature of a disruption is highly varying but there are three main features observed in every disruption's sequence (see figure 3): first, some precursor instabilities occur driving the plasma to the onset of a disruption. This process can be rather complex and last up to a few hundred milliseconds. Second, the sudden loss of the thermal energy stored within the plasma, which is referred to as thermal quench (TQ). This can result in temperatures dropping by several orders of magnitude to just a few eV even in the plasma centre. Third, due to the low temperature, the resistivity rapidly increases due to its strong dependency on the temperature[12] and therefore the plasma current decays. This is referred to as current quench (CQ).

It does not only mean an immediate end of the fusion process but also massive stress on the machine, i.e. heat loads on first wall components and enormous Lorentz forces caused by induced halo and eddy currents acting on the vacuum vessel during the current quench[32]. This can lead to serious damage of first wall, vacuum vessel and further structures. Because of that, several approaches are under investigation which may predict, avoid or at least mitigate disruptions. The damage potential of disruptions scales with the machine size and therefore they must be treated effectively in ITER and future devices. It is expected that none at all or

only a few uncontrolled disruptions can be tolerated by a fusion reactor during its full lifetime. Nevertheless, it has been shown that disruptions already pose a serious issue in today's devices. Because of this, disruption mitigation and avoidance techniques are standard tools today for plasma experiments. Their effectiveness also for ITER at full operation is not yet clear however. An overview of disruptions with a focus on ITER is given by Hender et al. [35, Chapter 3].

Fundamental MHD activity of the disruption onset Disruptions have been observed even in the early stages of tokamak research and were firstly described as a hard alteration of the electron density and "diffusion of charged particles to the chamber walls"[27]. A deeper insight into their causes and consequences only became possible by an improvement of diagnostic tools, namely external coils for the identification of MHD-modes[83],[68] and a deeper understanding of MHD itself. From that, it was accepted that current driven MHD instabilities play a crucial role during the disruption onset. That is the tearing mode on the one hand: due to finite plasma resistivity magnetic field lines around a $q = m/n$ rational surface reconnect changing the topology of the magnetic confinement with toroidal periodicity n and poloidal periodicity m[24],[23]. The newly formed so called magnetic islands reduce energy confinement of the plasma.

On the other hand, if a rational surface lies outside or on the surface of the plasma, the corresponding instability is called external kink mode. A surface kink leads to a torque which deforms the plasma periodically[88]. From stability analysis of the kink mode, it has already been derived during the earlier times of fusion research[48],[73] that the pinch and toroidal geometries would be unstable against kink modes with mode numbers $m = 1$ and $m = 2$. Further calculations for a broad range of possible current profiles[10] have shown that a plasma will be unstable to (m/n) tearing or kink modes if $(m-1) < nq_0 < nq_a < m$. A further general prediction from theory is that a mode tends to be unstable always if the relative current gradient $\frac{1}{j}\frac{\mathrm{d}j}{\mathrm{d}r}$ is steep. Therefore, due to the low current density on the plasma surface the confinement is always prone to instabilities if a rational surface is close to the surface[10],[6].

Experimental studies[68] and simulations[91] for various disruptive plasma discharges with $q(a) > 2$ have shown that the $(2/1)$ tearing mode commonly plays a crucial role during disruption onset. Over years, it has been experimentally proven[55],[31],[2] that the $(2/1)$ external kink also triggers disruptions. Therefore $q(a) < 2$ was identified as hard limit to avoid this type of disruptions.

The density limit This raises the question why a tearing mode grows if the initial current profile was stable against any modes. An explanation comes from the assumption that the edge plasma (i.e. for $q > 2$) gets cooled down and due to the increase of resistance the current density gradient outside of the $q = 2$ surface steepens destabilizing the $(2/1)$ tearing mode. A common cause for that cooling is the radiation instability: if the plasma is in a thermodynamic equilibrium, radiative losses are proportional to the square root of the temperature and compensated by heating power. In a fully ionized plasma the radiative losses are due to bremsstrahlung. Partly ionized elements lead to additional temperature dependent radiation losses. This is a concern even for low-Z impurities in the outer region, where they can change the thermal equilibrium significantly. In an extreme case, the temperature of the plasma edge is lowered to tenths of eV in a poloidally asymmetric region, mostly located around the divertor, due to the decrease of thermal conductivity. This instability is called a MARFE[51] which

often occurs during a disruption, triggering $(3/1)$ and $(4/1)$ modes.

These radiation losses scale with n_e^2 for given heating power and extensive research about a density limit for safe reactor operation has been carried out over the years[29],[28] considering more effects besides radiation collapses. However, due to the lack of understanding of the underlying physics a general scaling law for the density limit could not be derived yet. Yet, a parameter space for tokamak operation can roughly be isolated and is often depicted as the Hugill diagram (see [29], [89], etc.) . A low density limit, which is mainly important for startup scenarios only, can be derived if we take generation of runaway electrons (REs) into account. REs are a result of the interplay between the toroidal electric field that accelerates the plasma electrons and the decelerating friction due to collisions: below a critical density, the friction forces become small enough, that a specific fraction of the electrons is accelerated towards relativistic velocities.[49]. In virtue of their high energies REs have a huge damaging potential on plasma facing component[25]. The generation of REs often sets in during the later phase of a disruption, too.

Mode locking Based on the reached limit, disruptions were mainly categorized into two categories[89]: If the density limit is reached, the initial $(2/1)$ tearing mode starts to grow and still rotates with the rest of the plasma at frequencies of up to some kHz. After the perturbation reaches a critical amplitude, interaction with the wall by $j \times B$ forces results in a significant deceleration of plasma rotation. This further destabilizes the mode and finally leads to mode locking. Meanwhile, non-linear coupling will destabilize more modes and if neighbouring islands overlap magnetic field lines will become stochastic[67],[11]. Experiments have shown that modes like the $(3/1)$, $(3/2)$[78] $(1/1)$ or even $(5/3)$[68] get excited. Both the existence of islands itself and also the stochastization increase the radial heat transport and cause a flattening of temperature profiles in the affected region. This process takes place typically in ms and may lead first to a minor disruption, that is an incomplete TQ, from which the temperature profile recovers. When q_0 drops below unity due to current peaking in the centre, as a result of minor disruptions, the $(1/1)$ internal kink mode gets destabilized, which leads to a full stochastization of the plasma. Plasma current decays due to the rapid increase of resistivity. The exact physics of TQ and CQ phases remain not fully understood.

Other disruption types like low-q disruptions, in which the $(1/1)$ external kink mode plays a crucial role, exists but are not the target of this thesis. An axisymmetric instability called "vertical displacement event", which is the loss of control of vertical position in an elongated plasma, can also lead into a disruptive situation: if the plasma moves into the first wall, a major disruption will arise, where thermal and current quench set in simultaneously. On the other hand VDEs can also be the consequence of density limit or locked mode disruptions.

Prediction, mitigation and avoidance Due to their impact on the machine, disruptions need sophisticated handling strategies. The first step is to identify a disruption during its onset and to predict its harmfulness. This needs an estimation of thresholds of plasma parameters, for which the likelihood for a disruption gets significant. Apparently signals of $(2/1)$ modes are of great relevance here. Due to the lack of detailed understanding of the disruption onset the precise determination of these thresholds is still a field of theoretical and experimental[63],[86],[79] research. The plasma state needs to be updated in real time, i.e. in the order of a few ms, to decide ideally within a minimum warning time[85], which actions need to be taken:

If a disruption is predicted to be small or could have been identified in a very early stage it is more likely to fully avoid its further development. Avoidance can be possible by changing the plasma parameters through the control systems to move the plasma into a more stable operational regime. Stabilization of neoclassical tearing modes (see 2.2.3) by compensating for the missing bootstrap current using electron cyclotron current drive is currently considered a promising technique for disruption avoidance.[42],[74]

In other cases disruptions are not avoidable and disruption mitigation systems (DMS) are activated to reduce the consequences of the disruption to a level which can be tolerated by the machine. Therefore DMSs aim to convert plasma energy into electromagnetic radiation to lower thermal heat loads, minimize mechanical loads during VDEs and avoid the generation of REs.[50],[82] Mitigation can be achieved by massive injection of deuterium and high-Z impurities, like Argon or Neon. The most explored technique is called massive gas injection,[64],[39] another concept is the injection of material in form of shattered pellets.[13]

1.5. Numerical simulations in fusion research

A crucial tool of today's research The limitations of diagnostics and the high complexity of experiments have motivated the need for simulations. Based on an appropriate physics model, observations in experiments can be reproduced. If a simulation passes a detailed validation on the basis of experimental results, it gives the possibility to obtain information about experiments, which cannot directly be measured. For example an experiment can only measure temperatures at some points limited by the installed instruments, while the simulation will consistently calculate temperatures over the whole plasma. Therefore it enhances the understanding of the theoretical mechanism.

Besides simulations can also have a predictive character: present machines can not match all parameters of future device machines, so that meaningful predictions get only possible by simulating future devices. Findings from experiments are thus extrapolated by the simulations.

Simulations of disruptions First simulations of disruptions were carried out in the eighties which already confirmed the relevance of $(2/1)$ tearing modes[81] and locking mechanisms[65].Yet due to the lack of computational capacities but also huge uncertainties of the underlying physical processes only very simplified models could be implemented. Typical strategies were to ignore mode coupling, to linearise and reduce the MHD equations, to neglect any non-MHD activity or to reduce the number of dimensions and only consider simple geometries[41]. Nevertheless the understanding of many details of MHD acitivity during disruption onset and thermal quench could be qualitatively improved.

Realistic simulations of disruptions in existing machines and predictions for ITER need more sophisticated models and codes. Currently in use for that purpose are mainly the 3D non-linear extended MHD codes NIMROD,[58] M3D,[62] M3D-C1[45] and JOREK (see 3.1).

Several effects of disruptions in existing machines have been simulated successfully. This includes a wide range of VDE-simulations, showing good agreement of the codes.[46] With JOREK and M3D-C1 simulations of VDEs in ITER have been carried out.[1] Also a model for runaway electrons to study their interaction with the background plasma has been implemented recently into JOREK.[3]

The triggering of a disruption by MGI, which is of great interest for the development of

DMSs for ITER, has been simulated for a JET plasma.[16] Also, simulations of shattered pellet injections in JET exist[43].

Great gaps in simulation of a full disruption onset still exist. Yet it is of particular relevance since only simulations can give a quantitative basis for the identification of operational limits of ITER for operational scenarios that are prone to disruptions. A better understanding of the onset will therefore enhance disruption avoidance and mitigation schemes significantly. These detailed simulations also need to investigate the role of more complex disruption precursors like edge localized modes or sawtooth instabilities in ITER.

Many simulations of specific aspects exist which does not give a full picture of a disruption onset yet: for example simulations of NTM onset in current machines[9] are available, which however do not end in a disruption. By contrast simulations of thermal quenches were made, which roughly confirm experimental observations but already assume the existence of locked islands.[78]

The long term goal is therefore to enable the possibility of simulating the full sequence of "natural" and mitigated disruptions of relevant categories in ITER. Hence the relevant mechanisms of disruption onset and consequences need to be implemented and validated. Based on these simulations the opportunities of disruption avoidance and mitigation systems will be reviewed to predict realistic instructions for disruption mitigation or avoidance in ITER.

1.6. Objectives of this work

This thesis demonstrates some of the most important elements for disruptions simulations and their validation with the JOREK code. For this purpose, in ASDEX Upgrade geometry, (1) virtual diagnostic coils are set up and the signals caused by a $(2/1)$ mode are analysed, (2) the development of a $(2/1)$ locked mode into a partial thermal quench is simulated, and (3) the interaction of a rotating magnetic island with conducting structures is studied. These objectives needs to be seen in light of the long term goal of disruption simulations.

(1) Full simulations of a disruption sequence including the reactions of mitigation or avoidance systems also needs to consider appropriate diagnostic signals. Theories derived for very simple cases are commonly used for its analysis. However, a systematic validation of this theory in realistic, toroidal geometries has never been carried out. Therefore a set of diagnostic coils will be implemented for a simulation of locked tearing modes as part of this thesis. The signal will be investigated and compared to the theory to estimate its actual validity.

(2) A $(2/1)$ non-rotating tearing mode will be excited through a tearing mode unstable equilibrium current. The onset of stochastisation with respect to the mode width and its influence on temperature profiles are relevant objectives hereby. Hence it will be checked if this excitation already leads to a thermal quench. The simulations are carried out with and without an ideal wall to analysis the mode suppression effect by the conducting wall.

(3) The interaction of poloidal rotation with walls of different resistivities is investigated. It will be checked for which resistivity the momentum transfer is the strongest, i.e. the locking occurs the fastest.

1.7. Thesis outline

The first part of this thesis is structured as follows: Chapter 2 will give a detailed background about the physics involved in a thermal quench. This includes an overview about magnetohydrodynamics, (neoclassical) tearing modes, field stochastisation and mode locking. Chapter 3.1 introduces the non-linear magnetohydrodynamics code JOREK, its coupling with the free boundary extension STARWALL, as well as diagnostic tools.

The second part presents and discusses the simulations which have been carried out in the course of this thesis: Chapter 4 describes, how virtual diagnostic signals of a $(2/1)$ mode have been produced. They are compared to some theoretical predictions. Chapter 5 contains the results of the simulation of a partial thermal quench. A series of different physical aspects, including the analysis of mode coupling, stochastisation and the effects on the temperature profile are investigated. Chapter 6 describes the the simulation of plasma rotation and the interaction of the rotating plasma with the wall for different resistivites.

Chapter 7 summarizes the work and gives an outlook. This includes in particular possible simulations that are based on the partial thermal quench to enhance the knowledge about disruptions and their mitigation.

Part I.
Background

2. Theoretical Background

The next section will give a detailed theoretical background for this work. The magnetohydrodynamics formulation is introduced first. From that basis, the relevant physical mechanisms involved in disruptions are introduced. Finally an overview of diagnostic tools is given to analyse MHD instabilities in experiments, which are also crucial for the prediction of disruptions.

2.1. Magnetohydrodynamic description of a plasma

A brief overview of magnetohydrodynamics (MHD) is given in this chapter. A more comprehensive discussion is for example given by Schnack [71].

2.1.1 From kinetic equations to multi-fluid equations

Kinetic equation The description of a magnetized plasma is a many body problem consisting of typically $N = 10^{20}$ particles per m^3. We assume here for simplicity, that the plasma is fully ionized (i.e. no non-elastic collisions) and does not exhibit impurities. The particles of each species α - electrons and ions - can be described by distributions in phase space for a given time point t_0: $f_{\alpha,N}(\vec{x},\vec{v},t_0) = \sum_i^N \delta(\vec{x}-\vec{x}_i(t_0))\delta(\vec{v}-\vec{v}_i(t_0))$. As we are dealing with fusion plasmas, the Lorentz force $\vec{F}_N = q_\alpha(\vec{E}_N + \vec{v}\times\vec{B}_N)$ is the only relevant force acting on the particles. The electric and magnetic fields $\vec{E}_N$ and $\vec{B}_N$ are determined by the $f_{\alpha,N}$ themselves and Maxwell's equations. The temporal evolution of the distributions is then exactly given by the continuity equation $\mathrm{d}f_{\alpha,N}/\mathrm{d}t = 0$.

Apparently this system of N differential equations can not be solved directly and instead an appropriate approximate description is needed, i.e. a description which can be fully determined by macroscopic quantities and still predicts the plasma behaviour sufficiently well. Therefore, we replace $f_{\alpha,N}$ by a continuous density function f_α by ensemble averaging, which means that individual particles become indistinguishable. Also, the electric $\vec{E}$ and magnetic $\vec{B}$ fields are now determined by f_α. Of course, these three macroscopic quantities can not describe the exact behaviour of particles on a microscopic scale any more. However, depending on the initial distribution and the time scales we are looking at, these microscopic interactions, which are summarized as collisions, can still have significant influence onto the macroscopic scale. Therefore, the collision operator $(\partial f_\alpha/\partial t)_{\mathrm{coll.}}$ needs to be introduced. The continuity equation is then modified to:

$$\begin{aligned} \frac{\mathrm{d}f_\alpha(\vec{x},\vec{v},t)}{\mathrm{d}t} &= \left(\frac{\partial f_\alpha}{\partial t}\right)_{\mathrm{coll}} \\ \Leftrightarrow \frac{\partial f_\alpha}{\partial t} + \vec{v}\cdot\nabla f_\alpha + \frac{q_\alpha}{m_\alpha}\left(\vec{E}+\vec{v}\times\vec{B}\right)\cdot\nabla_{\vec{v}} f_\alpha &= \left(\frac{\partial f_\alpha}{\partial t}\right)_{\mathrm{coll}}, \end{aligned} \tag{2.1}$$

which is known as the kinetic equation.

Moments of distribution The next assumption is that f_α is close to Maxwellian, which means that the plasma is in thermal equilibrium and the collision operator for collisions between particles of only one species is close to zero. The plasma can then be treated as a fluid.

In this case, one can average the kinetic equation, where f_α is replaced by its moments, which are macroscopic quantities again. The k^{th} order moment is defined by

$$\int_{\mathbb{R}} \underbrace{\vec{v} \otimes ... \otimes \vec{v}}_{k\,\text{times}} f_\alpha \mathrm{d}^3 v \tag{2.2}$$

For $k = 0$, the particle density n_α is obtained:

$$n_\alpha = \int_{\mathbb{R}^3} f_\alpha \mathrm{d}^3 v \tag{2.3}$$

For $k = 1$, the fluid velocity $\vec{u}_\alpha$ is obtained:

$$\vec{u}_\alpha = \frac{1}{n_\alpha} \int_{\mathbb{R}^3} \vec{v} f_\alpha \mathrm{d}^3 v \tag{2.4}$$

We can define the random thermal motion $\vec{w} = \vec{v} - \vec{u}_\alpha$ and find that the pressure tensor $\bar{\bar{P}}_\alpha$ is given by the second moment regarding $\vec{w}$:

$$\bar{\bar{P}}_\alpha = m_\alpha \int_{\mathbb{R}^3} \vec{w} \otimes \vec{w} f_\alpha \mathrm{d}^3 v \tag{2.5}$$

It is convenient to distinguish between the antisymmetric part $\bar{\bar{\pi}}_\alpha$ and the isotropic pressure p_α, so that $\bar{\bar{P}}_\alpha = p_\alpha \bar{\bar{1}} + \pi_\alpha$, where $\bar{\bar{1}}$ is the unit tensor. When the plasma is assumed to be in thermal equilibrium, the ideal gas law can be applied: $p_\alpha = n_\alpha k_\mathrm{B} T_\alpha$, with the temperature of the species T_α and the Boltzmann constant k_B.

We only need the symmetric part of the third moment, which is the heat flux $\vec{q}_\alpha$:

$$\vec{q}_\alpha = m_\alpha \int_{\mathbb{R}^3} \vec{w} \frac{|\vec{w}|^2}{2} f_\alpha \mathrm{d}^3 v \tag{2.6}$$

Integrals of the kinetic equation To yield fluid equations, we integrate the kinetic equation over velocity space. Since we only consider elastic collisions and the number of particles is conserved, the integral of the collision operator will vanish, otherwise we could define it as a particle source term here. Note also, that $f_\alpha(|\vec{v}| \to \infty) \to 0$.

Hence we get the continuity equation for each species:

$$\frac{\partial n_\alpha}{\partial t} + \nabla \cdot (n_\alpha \vec{u}_\alpha) = 0 \tag{2.7}$$

We had to insert the moments of zero and first order here.

Next, we multiply (2.1) with $\vec{v}_\alpha$ and integrate to yield the force balance after some rearrangement:

$$m_\alpha n_\alpha \frac{\mathrm{d}\vec{u}_\alpha}{\mathrm{d}t} = -\nabla \cdot \bar{\bar{P}}_\alpha + n_\alpha q_\alpha (\vec{E} + \vec{u}_\alpha \times \vec{B}) + \vec{R}_{\alpha\beta} \tag{2.8}$$

$\vec{R}_{\alpha\beta}$ is the first momentum of that part of the collision operator for collisions with unlike species. Its physical meaning is a friction force and it can only be calculated if a formulation for $(\partial f_\alpha/\partial_t)_{\text{coll}}$ is given. We had to insert the moments of zero, first and second order here.

Finally, we multiply (2.1) with $m_s|\vec{v}|^2/2$ to obtain the energy equation:

$$\partial_t(n_\alpha\epsilon_\alpha) + \nabla(n_\alpha\epsilon_\alpha\vec{u}_\alpha + \bar{\bar{\pi}}_\alpha\cdot\vec{u}_\alpha + p_\alpha\vec{u}_\alpha + \vec{q}_\alpha) = n_\alpha q_\alpha\vec{E}\cdot\vec{u}_\alpha + Q_{\alpha\beta} + \vec{R}_{\alpha,\beta}\cdot\vec{u}_\alpha \tag{2.9}$$

$\epsilon_\alpha = 3/2\frac{p_\alpha}{n_\alpha} + 1/2 m_\alpha|\vec{u}_\alpha|^2$ is the specific total energy. $Q_{\alpha\beta}$ is the second momentum of that part of the collision operator for collisions with unlike species. Its physical meaning is heat transfer from particles of species β to the ones of α. We had to insert the moments of zeroth to third order here.

Closure Apparently each equation (2.7)-(2.9) contains at least one moment of a higher order than the order of the equation itself. Therefore we need to find a closure, which is to find an additional equation from independent physical principles that defines those moments of highest order. Here we need a definition of the conductive heat flux, which is given by the Braginskii closure[8]:

$$\vec{q}_\alpha = -n_\alpha\chi^\alpha_\parallel\nabla_\parallel T_\alpha - n_\alpha\chi^\alpha_c\nabla_c T_\alpha - n_\alpha\chi^\alpha_\perp\nabla_\perp T_\alpha \tag{2.10}$$

Where χ^α_x are the coefficients for the parallel to $\vec{B}$ and perpendicular heat transport. Transport along field lines is typically by eight to ten orders of magnitude higher than transport in the perpendicular direction.

2.1.2 From bi-fluid equations to extended Magnetohydrodynamics

Scaling parameters To yield Magnetohydrodynamic equations, the above equations (2.7)-(2.9) for each species are now reduced to one set of equations. After comparing the magnitudes of the phsycial effects of each fluid, it is convenient to neglect small terms. At first we can assume that the system length is much bigger than the Debye length, $\epsilon_1 = \lambda_D/L \ll 1$, what implies quasi neutrality, $\nabla\cdot E \to 0$, as explained in 1.2. Second, $\epsilon_2 = m_e/m_i \ll 1$, so that we can neglect electron inertia.

Considering a hydrogen plasma ($q_i = -q_e = e$), it follows for the fluid-variables, that:

$$n = n_e = n_i \tag{2.11}$$
$$\rho = n_i m_i + n_e m_e \approx n m_i \tag{2.12}$$
$$\vec{v} = \frac{1}{\rho}(m_i n_i\vec{u}_i + m_e n_e\vec{u}_e) \approx \vec{u}_i \tag{2.13}$$
$$\vec{j} = e n_i u_i - e n_e u = e n(u_i - u_e) \tag{2.14}$$
$$p = p_i + p_e \tag{2.15}$$

Derivations By summing up the continuity equations (2.7) we obtain

$$\partial_t\rho + \nabla\cdot(\rho\vec{v}) = 0 \tag{2.16}$$

By summing up the force balances (2.8) and using that $R_{ie} = -R_{ie}$ we get

$$\rho \mathrm{d}_t \vec{v} = -\nabla p + \vec{j} \times \vec{B} \tag{2.17}$$

To yield an equation for the pressure, we first have to multiply both force balances by the corresponding velocity and then subtract these from the energy equations. After introducing heat capacity ratio for a monatomic gas, $\gamma = 5/3$, and adding both equations, some rearrangements, approximating the heat source by $Q_{\alpha,\beta} = 3\frac{n_\alpha}{\tau_\alpha}(T_\alpha - T_\beta)$ and interpreting the friction force as an effect of the resistivity, $\vec{R}_{ei} = -\eta \frac{e}{m_i} \rho \vec{J}$, we have the pressure equations

$$\frac{1}{\gamma - 1}\partial_t p_i + \frac{1}{\gamma - 1}\vec{u} \cdot \nabla p_i + \frac{\gamma}{\gamma - 1} p_i \nabla \cdot \vec{u} + \nabla \cdot \vec{q}_i + \bar{\bar{\pi}}_i : \nabla \vec{u} = \quad 3\frac{n_e}{m_i}(T_i - T_e) \tag{2.18}$$

$$\frac{1}{\gamma - 1}\partial_t p_e + \frac{1}{\gamma - 1}\vec{u} \cdot \nabla p_e + \frac{\gamma}{\gamma - 1} p_e \nabla \cdot \vec{u} + \nabla \cdot \vec{q}_e + \bar{\bar{\pi}}_e : \nabla \vec{u} =$$

$$\pi_e : \nabla \left(\frac{m_i}{e\rho} \vec{J} \right) - 3\frac{n_e}{m_i}(T_i - T_e) + \eta |\vec{J}|^2 \tag{2.19}$$

Generalized Ohm's law As $\nabla \cdot E = 0$ due to quasi-neutrality, another non-trivial expression for the electric field is necessary. This can be derived from the electron's equation of motion (2.8) by re writing it in terms of the one-fluid velocity $\vec{v}$

$$\vec{E} + \vec{v} \times \vec{B} = \eta \vec{J} - \frac{m_i}{\rho e} \nabla \cdot \bar{\bar{\pi}}_e + \frac{m_i}{\rho e} \vec{J} \times \vec{B} - \frac{m_i}{\rho e} \nabla p_e \tag{2.20}$$

Ideal and Resistive MHD The equations (2.16)-(2.20) are the formulation of the extended MHD, which contains equations for pressure, and terms for resistivity and two-fluid effects. For different scaling parameters it would be possible to derive ideal MHD equations, which neglect resistive effects. For a hot fusion plasma, the description using ideal MHD is often sufficient. However the understanding of resistive instabilities requires the resistive MHD at least in some layers within the plasma. It would be also possible to close the system of equations already with the second moment. Since heat fluxes play a crucial role during the disruption onset, the extended MHD including also third moment terms, is required here.

2.2. Tearing modes and magnetic islands

2.2.1 Classical tearing mode theory

A global instability which can be described well within the resistive MHD framework is the Tearing Mode. While the resistive effects only play a role within layers with widths in order of Lamour radius, these modes can change the topology of B globally by reconnection.

Stability of a current sheet The phenomenon of magnetic reconnection can be understood on a current sheet: let the equilibrium current pointing in negative z-direction, as depicted in figure 4. This implies a magnetic field of $\vec{B}_0(x) = -B_0 x / L \vec{e}_y$, where L is the spatial extent of the current sheet in x-direction. The plasma is now initially perturbed periodically

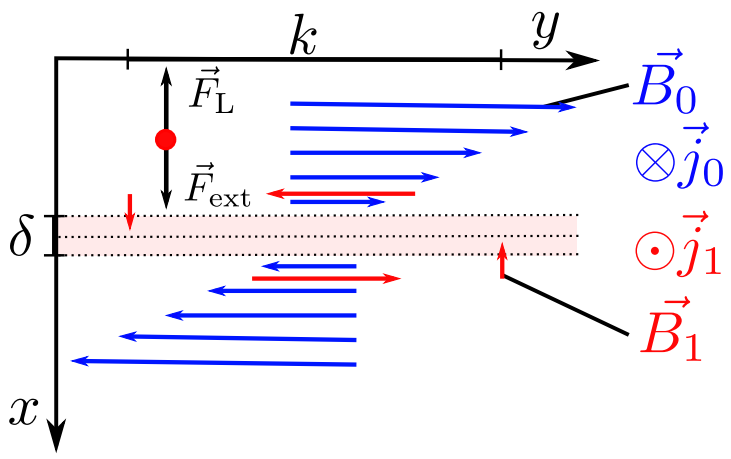

Figure 4: Equilibrium fields (blue) and perturbed fields (red) of a current sheet. Within the area of width δ resistive MHD applies. The forces that act on an exemplary volume of plasma (red dot) are also shown.

in y-direction by an external force $\vec{F}_{\mathrm{ext}}$. That flow of charged particles will induce a periodic current $\vec{j}_1$ in Z direction regarding Ohm's law. This means in turn a restoring Lorentz force of $\vec{F}_L(x) = -\sigma\vec{v}_{\mathrm{ext}}|\vec{B}_0(x)|^2$. Due to the strong dependency on $\vec{B}_0$, there will be a region of width δ around $x = 0$, where some arbitrary small external force can not be retained by the plasma any more. Within the layer, the induced current becomes dominating. Regarding linearised Maxwell's equations, this implies a growing perturbed magnetic field $\partial_t B_{1,x} = (\vec{k} \times \vec{j}_1)_x$. Superposition of $\vec{B}_0$ and $\vec{B}_1$ implies a twisting of the field lines towards the x-axis. Due to divergence freedom of magnetic fields, we will have a periodic reconnection of the lines. This is the basic concept of the linear tearing mode. During growth of that instability, the magnetic field for $x > \delta$ will be affected also, provoking further reconnection until a macroscopic magnetic island is produced.

A situation similar to a current sheet can be found in a tokamak around rational surfaces due to the shear. The equilibrium field of the current sheet $\vec{B}_0$ now corresponds to the so called magnetic helical field $\vec{B}_0^*$. Assuming constant shear around r_s it is then given by:

$$\vec{B}_0^* \approx \vec{B}_0(r) - \vec{B}_0(r_s)\frac{r}{r_s} \tag{2.21}$$

Stability parameter and timescales The orientation of the perturbed quantities determines if a perturbation can stabilize itself. Therefore, it is convenient to define the stability parameter by considering $\vec{B}_1$.

$$\Delta' \equiv \frac{k[B_{1,y}(\delta/2) - B_{1,y}(-\delta/2)]}{|B_{1,x}|}, \tag{2.22}$$

If $\Delta' < 0$, $\vec{j}_1 \parallel \vec{j}_0$ and therefore the equilibrium field gets strengthened. Otherwise the mode is unstable as it is the case for a current sheet. Δ' is also a quantity for its linear growth rate γ. The timescale for reconnection is much greater than Alfven time-scale but much smaller

than resistive-diffusion time, so that

$$\frac{L}{v_A} = \tau_A \ll \frac{1}{\gamma} \ll \tau_R \approx \frac{\mu_0 a^2}{\eta} \tag{2.23}$$

Tearing mode equation For further treatment of tearing modes, it is convenient to describe the magnetic fields by flux functions, i.e. $\vec{B} = \nabla\Psi \times \vec{e}_z$. The perturbed flux regarding a rational surface (m/n) is then given by $\Psi_1 = \Psi_1(r)\exp[i(m\theta - n\phi)]$.

The corresponding components of $\vec{B}$ are:

$$B_r = \Re\left(\frac{1}{r}\frac{\partial\Psi}{\partial\theta}\right) \tag{2.24}$$

$$B_\theta = \Re\left(-\frac{d\Psi}{dr}\right) \tag{2.25}$$

Outside the resistive layer, stability can be investigated by an energy principle for ideal MHD. From that the tearing mode equation is derived:

$$\Delta\Psi_1 - \frac{\mu_0 d_r j_{0,z}}{B_{0,\theta}(r)(1 - q(r)n/m)}\Psi_1 = 0 \tag{2.26}$$

Two independent solutions have to be found for Ψ_1 inside and outside of the rational surface. The resistive layer δ is assumed to be arbitrary thin. Due to linearity both solution can now be scaled in such a way that it matches the condition $\Psi_1(r_s^- = r_s - \delta/2) = \Psi_1(r_s^+ = r_s + \delta/2)$ to yield continuity of Ψ_1 if $\delta \to 0$. However this implies a sudden change of Ψ_1' around r_s. This jump

$$\Delta' = \left[\frac{1}{\Psi_1}\frac{d\Psi_1}{dr}\right]_{r_s^-}^{r_s^+} \tag{2.27}$$

is equivalent to the stability parameter in (2.22) . (2.26) exhibits the strong dependence on the current density gradient. Calculations for explicitly given current gradients have shown that for $d_r j_{0,z}(r > r_s) > d_r j_{0,z}(r < r_s)$ the mode tends to be unstable. This is in accordance to the experimental observations during disruption onset as introduced in 1.4.

The energy principle for the tearing mode shows, that the stabilizing energy grows with m, i.e. $\Delta' \approx -2m/r_s$ in cases where classical tearing modes are stable. Therefore tearing modes with low poloidal mode number are usually more likely observed.

Magnetic Islands In fact the linear treatment of tearing mode is only valid in the first moment of its occurrence. Since it changes the topology of the magnetic field, its evolution is mainly a non-linear process. This newly formed field line structure is given by the superposition of Ψ_1 and Ψ_0. It yields the occurrence of magnetic islands, which are areas of nested flux surfaces that are isolated from the bulk of the plasma (see figure 5). Islands behave periodic, with a periodicity determined by m and n of the corresponding tearing mode. An island reaches its maximum radial expansion at the O-Point which is the island width given by:

$$W = 4\sqrt{\frac{\overline{\Psi_1}}{\Psi_0''}} = 4\sqrt{\frac{B_{1,r}}{B_{0,\theta}}\frac{r_s q}{m q'}}. \tag{2.28}$$

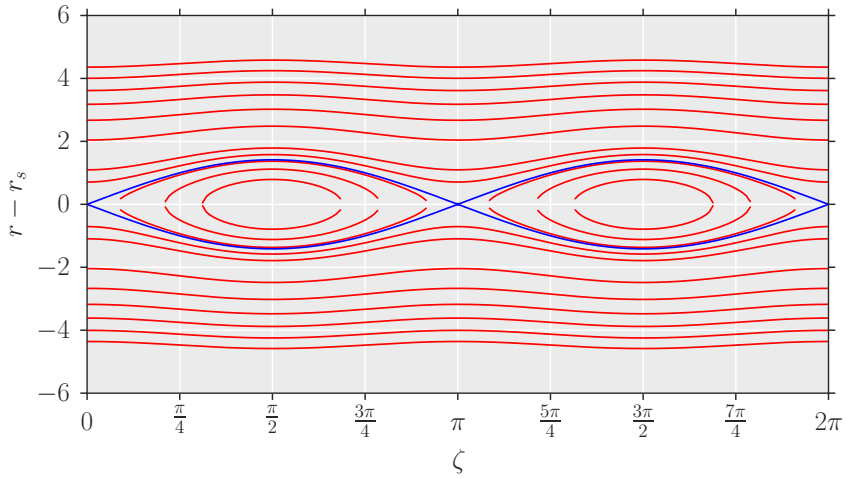

Figure 5: Flux surfaces after occurrence of a $(2/1)$ island. The surface in blue is also called the island separatrix, as it is the boundary inside the island and the boundary region. $\zeta \equiv \theta - \frac{n}{m}\phi$ is called the magnetic coordinate. O-Points at $\zeta = \pi/2$ and $\zeta = 3\pi/2$; X-Points at $\zeta = 0$ and $\zeta = \pi$.

Rutherford equation Understanding the growth rate of the island requires a focus on the mechanisms within the island itself. However only outside the island the plasma can still be treated within ideal MHD where (2.26) holds and its solution has to be matched at the island separatrix now. The stability parameter is now defined by a non-linear definition considering an integral of the current distribution within the island. Proceeding from that the evolution of island width is derived as being:

$$\frac{\tau_R}{r_s}\frac{dW}{dt} = r_s \Delta'. \tag{2.29}$$

with the resistive timescale $\tau_R = 0.82\mu_0\sigma r_s^2$. (2.29) is known as Rutherford equation, which does not take into account the impact of the island on kinetic profiles which will influence the tearing mode stability in turn. Therefore, this formulation is also just valid in the first phase of island growth.

2.2.2 Effects on temperature profile

Indeed the island will have a significant influence on the temperature profile after reaching a critical island width since the islands yields a connection of different radial regions. The radial gradient of the equilibrium temperature profile will lead to an initial temperature gradient on the island separatrix, which is of order $\nabla_\parallel T \approx B_{1,r}/B_\phi \nabla_\parallel T$. Since $\kappa_\parallel \gg \kappa_\perp$ holds, as shown in section 2.1.1, strong heat fluxes can be expected around the island. Expressing $B_{1,r}$ in terms of W and taking divergence freeness of $\vec{q}$ leads to an expression of the temperature gradient for non vanishing W:

$$\left(\kappa_\parallel \left[\left(\frac{W}{2}\right)^2 \frac{n s_s}{R_0 r_s}\right]^2 + \kappa_\perp\right) \nabla_\perp^2 T \approx 0 \tag{2.30}$$

This implies a critical island width w_c, for which the temperature gradient around the O-Point of the island will vanish. As a result, the temperature and pressure profile starts to get flattened around r_s. By reformulation and considering some other effects, Fitzpatrick formulated w_c as[19]

$$w_c = 5.1 \sqrt[4]{\frac{\kappa_\perp}{\kappa_\parallel}} \sqrt{\frac{R_0 r_s}{n s_s}} \tag{2.31}$$

In fact, an axisymmetric flattening of the temperature, that exceeds the whole island is only reached, if the island reaches an with of $3w_c$ to $4w_c$. [40, Section 5.1]

Non-linear saturation The flattening of the temperature profile also affects the current distribution by a modification of resistivity around the island. Therefore the driving current gradient will flatten and the stability parameter decreases monotonously with further island growth. This implies a saturated island width, which is being approached exponentially with time:

$$W(t) = W_{\mathrm{sat}} \left[1 - \exp\left(-t \frac{r^2 \Delta'(0)}{\tau_R W_{\mathrm{sat}}} \right) \right] \tag{2.32}$$

W_{sat} is determined by initial $d_r j_0$.

2.2.3 Neoclassical tearing modes

As described in the last section the current density is the driving quantity of tearing modes. Classical theory only considers the externally driven inductive current. In addition the neoclassical currents present in finite β plasma influence the stability of tearing mode, which leads to the class of so called neoclassical tearing modes (NTMs). Since NTMs become more relevant in high pressure plasmas, they limit the maximum achievable pressure. To quantify the mode growth of NTMs, the Rutherford-equation needs to be extended.

Bootstrap current The main contribution to the non-inductive currents comes from the bootstrap current. It is a result of the inhomogeneity of B_ϕ, which leads to a gradient drift, (1.5). Because of this, the toroidal mobility of particles is limited and they get trapped on so called "banana-orbits". These trapped particles collide with free ones and accelerate them. Taking the pressure gradient into account the effect leads to an effective current in terms of MHD. This so called bootstrap current is mainly carried by the free, accelerated electrons and is quantified by:

$$j_{\mathrm{bs}} \propto \sqrt{\frac{r}{R_0}} \frac{\nabla p}{B_\theta} \approx -\sqrt{\frac{r}{R_0}} \frac{1}{L_p} \tag{2.33}$$

with the pressure scale length $L_p = -p/(\mathrm{d}p/\mathrm{d}r)$. A more precise formulation has been derived by Sauter.[70]

Modified Rutherford equation The Pfirsch-Schlüter current, which guarantees $\nabla \cdot j = 0$, modifies the stability of TMs also. Its influence is quantified by the Glasser-Greene-Johnson-term[26].

Taking both effects into account the Rutherford equation now reads as:

$$\frac{\tau_R}{r_s}\frac{\mathrm{d}w}{\mathrm{d}t} = r_s\Delta'(w) + c_{\mathrm{sat}} f_{\mathrm{GGJ}} \sqrt{\frac{r_s^3}{R_0}} \frac{L_q}{L_p}\frac{\beta_p}{w} \tag{2.34}$$

c_{sat} is a constant that is dependent on the saturated island width, f_{GGJ} is a constant given by the Glasser-Greene-Johnson-term, L_q is the q scale length, similar defined to L_p and $\beta_p = \langle p \rangle / {B_\theta^2}/{2\mu_0}$ is the poloidal plasma beta.

The neoclassical drive can now be understood as follows: by the flattening of the pressure profile within the island the bootstrap current is decreased helically on the resonant surface. This is equivalent to an "effective" current pointing in the same direction like the perturbed current j_1 and hence drives the island growth. That neoclassical drive decreases with increasing island width, therefore the neoclassical fraction in (2.34) is proportional to w^{-1}. However, (2.34) exhibits an singularity for arbitrary small islands and can not predict its growth rate correctly. In fact the assumption of complete flattening breaks down for small island sizes below W_0 given in (2.31), which is referred as the "transport threshold". The neoclassical drive gets also impaired for rotating islands, that are smaller than the "polarization threshold": the rotation causes a time varying field that in turn leads to a stabilizing modification of banana orbits.

A corrected Rutherford equation that respects both thresholds reads as:

$$\frac{\tau_R}{r_s}\frac{\mathrm{d}w}{\mathrm{d}t} = r_s\Delta'(W) + \sqrt{\frac{r_s^3}{R_0}} \frac{L_q}{L_p}\frac{\beta_p}{W} \left(c_{\mathrm{sat}} f_{\mathrm{GGJ}} \frac{W^2}{W_0^2 + W_2} - c_{\mathrm{pol}} \frac{\rho_{\theta,i}^2}{W^2} \right) \tag{2.35}$$

Further mechanisms can play a role and modify the growth rate significantly, e.g. runaway electrons during the non-linear phase significantly[34].

Stability regimes NTMs can grow even when $\Delta'(w) < 0$ according to (2.35) A positive growth rate in that case, however requires the occurrence of a seeding island, which is greater than the small island thresholds. Seed islands are often caused by other MHD activities like sawteeth. Therefore that mode is called being "metastable". The mode saturates with an island width, at which the neoclassical instability term equals the classical stabilization term. It is also possible that neoclassical destabilization is too weak for every island width and island growth is fully suppressed. The mode is then called being "unconditionally stable". Since increasing the plasma beta moves unconditionally stable modes into the metastable regime, maximum reachable plasma pressure is limited.

Consequences for disruptions can be summarized as follows: if a small island is forced by some arbitrary external effects in an equilibrium stable to classical tearing modes, it may grows as a NTM. If it saturates at a width, where confinement degradation becomes significant and stochastisation sets is, it can cause a disruption.

2.3. Influence of conducting structures

The perturbed flux excited at an rational surface extends beyond the plasma and also affects the outer region: if the temporally changing perturbed magnetic field penetrates a wall, a current of the same periodicity will be induced. The current in turn produces an opposite

directed magnetic field, that penetrates the plasma. The sum of both helical fields is therefore reduced. Hence, the wall has a stabilizing effect and Δ' is decreased.

To calculate the field strength at the wall, some approximations need to be applied[17]. We assume, that the current density is negligible outside the rational surface. The z-component of Ampere's law expressed in terms of magnetic fluxes, $\Delta\Psi_1 = -\mu_0 j_z$, then reduces to to $\Delta\Psi_1 = 0$ for $r > r_s$. In addition considering the circular cross-section, high aspect ratio approximation, and appropriate boundary conditions we get the solution:

$$\Psi_1(r) = \hat{\Psi}_1 \left(\frac{r_s}{r}\right)^{-m} \exp[i(m\theta - n(\phi - \phi_0))] \quad \text{for} \quad r > r_s \tag{2.36}$$

With the amplitude at the resonant surface $\hat{\Psi}_1$, which is not constant in time for mode growth, and assuming the toroidal periodicity and allowing a phase shift ϕ_0, which is in case of island rotation not constant in time. In this assumption, a field reduces by $\propto r^{-m-1}$ outside the resonant surface.

The reduced magnetic field the can than be approximated as, if a wall is ideally conducting, i.e. its resistivity is given as $\rho_w = 0$:

$$B_r^w(r) \approx B_r(r)^{w.o.} \left(a - \left(\frac{r}{r_w}\right)^{2m}\right) \tag{2.37}$$

with the distance of the wall to the magnetic axis r_w and the minor radius a. $B_r(r)^{w.o.}$ is the perturbed field without conducting structures. Hence, if a wall would be indefinitely close to the plasma, all perturbations vanish at the edge.

With increasing the resistivity, the stabilizing effect decreases and vanishes for $\rho_w \to \infty$.

2.4. Plasma rotation and mode locking

A plasma usually exhibits a toroidal and poloidal rotation. It is mainly the result of the sum of diamagnetic drifts like given by (1.6) and a fluid velocity. The fluid velocity can be provoked by an external torque, like coming from neutral beam injections, that mainly forces the toroidal rotation. An additional contribution to poloidal rotation comes from E-cross-B drifts as given by (1.4). The electric field points in radial direction and is a result of further neoclassical effects. Therefore it is also called a "neoclassical E-cross-B drift". It is to note, that both the diamagnetic drift and the neoclassical E-cross-B drift are proportional to ∇p. Due to the incompressibility of the plasma, $\nabla \cdot v = 0$, an angular rotating frequency ω can be defined.

As discussed in the last section, a growing mode will induce currents in a conducting wall. The same applies for a rotating mode. For a finite resistivity these eddy currents will yield $j \times B$ acting on the vessel by the interaction with magnetic field components that are not in phase with the current. Due to Newton's third law, a counterforce will hence act on the vessel. Momentum transfer between plasma and machine occurs and the plasma reduces its rotation, which is called mode locking. The acting forces are highly dependent on rotational frequency and wall resistivity. A broad discussion is given in [57]. For the forces hold, that:

$$F_w \propto \frac{\omega\tau_w}{m^2 + (\omega\tau_w)^2} \tag{2.38}$$

where τ_w is the so resistive time of the wall. It can be approximated by $\tau_w = \mu_0/\rho_w bd/2$ with the wall resistivity ρ_w, minor radius of the vessel b and vessel thickness d. m is the poloidal number of the considered mode.

(2.38) shows, that the forces reach a maximum for $m/\tau_w \approx \omega$ and locking appears the fastest. In turn, for frequencies much higher or lower than this, no effect of the wall onto rotation is expected. Interaction with the wall usually brings the plasma to frequencies of a few Hz. The fully locking in turn is often the result of additional interaction with error fields.

2.5. Mode coupling and field stochastisation

The assume, that a $(2/1)$ mode is the dominant instability in a tokamak, however so called side band harmonics will be excited in two different ways by coupling.

Firstly, the background equilibrium field in a toroidal device exhibits a strong $m = 1$ component and also higher m components with lower amplitudes. As a consequence, the perturbed field of a $(2/1)$ mode has also a strong $m = 3$ component, for instance. Te amplitude of that component is only dependent on the $m = 2$ harmonic of the perturbation and the $m = 1$ harmonic of the equilibrium field. Since it is not localized in radial direction, it will also destabilize a secondary $(3/1)$ mode at the $q = 3$ surface. This is referred to as the (linear) coupling due to toroidicity.[21] The amplitude of the background field only hardly changes with time, so that the $(3/1)$ island is expected to grow with the same rate as the $(2/1)$ island. Also a $(4/1)$ mode can expected, which also the same growth rate as the $(2/1)$ mode, but will be significantly smaller due to the smaller amplitude of the $m = 2$ component of the background field.

Secondly, the MHD equations contain non-linear term, such that mode coupling can occur like it was described already for JOREK in a ballooning mode case[47]. The quadradic mode coupling takes places between the modes among each other and yields modes of higher n. Therefore, $(2/1)$ and $(3/1)$ may couple to yield modes of $n = 2$. This type of secondary islands is not expected to grow with the same rate as the primary $(2/1)$ mode, since their amplitude is expected to grow in a way proportional to the product of the amplitudes of the driving modes.

In a rotating plasma, the difference in the angular velocities between the respective flux surfaces would lead to a shielding effect of the magnetic perturbations leading to a suppression of the sidebands until the point where the perturbation is strong enough to reduce the rotational shear to a value close to zero, at which the secondary islands would "penetrate". This is the same mechanism as mode penetration caused by an external magnetic field like it has been investigated in detail with JOREK.[54]

Stochastisation If two adjoining magnetic islands get large enough, so that they overlap, magnetic flux surfaces get destroyed and a region between these islands is produced which is referred to as the stochastic layer: the trajectories of field lines in this layer become chaotic and it is not possible any more to define flux surfaces. The stochastisation sets in, if the Chirikov-Criterion is fulfilled:[11],[86]

$$1 < \sigma_{\mathrm{Ch}} = \frac{(w_{m/n} + w_{m\pm1/n})/2}{|r_{m/n} - r_{m\pm1/n}|} = \frac{w_{m/n}}{(ms)^{-1}}$$

With the magnetic shear $s = \frac{1}{q}\frac{\mathrm{d}q}{\mathrm{d}r}$. For $1 < \sigma_{\mathrm{Ch}}$, the average island width is greater than their distance, what implies overlapping.

The stochastisation can be quantified by a field line diffusion coefficient: as the field line diffuse in radial direction, an appropriate averaging leads to an effect radial component δB. From that it follows a definition by:

$$D_{\mathrm{st}} = \pi R_0 \left(\frac{\delta B_r}{B_0}\right)^2 \tag{2.39}$$

With major radius R_0.

The heat transport across the stochastic layer may get enhanced by field line diffusion only if the heat diffusion anisotropy $\chi_\parallel/\chi_\perp$ is great enough. Otherwise the effects of single islands on radial heat transport as discussed before are dominating. Additionally heat transport caused by stochastisation is given, if $\chi_\parallel/\chi_\perp > 10^7$. [40, Section 8.1]

2.6. Diagnostic coils

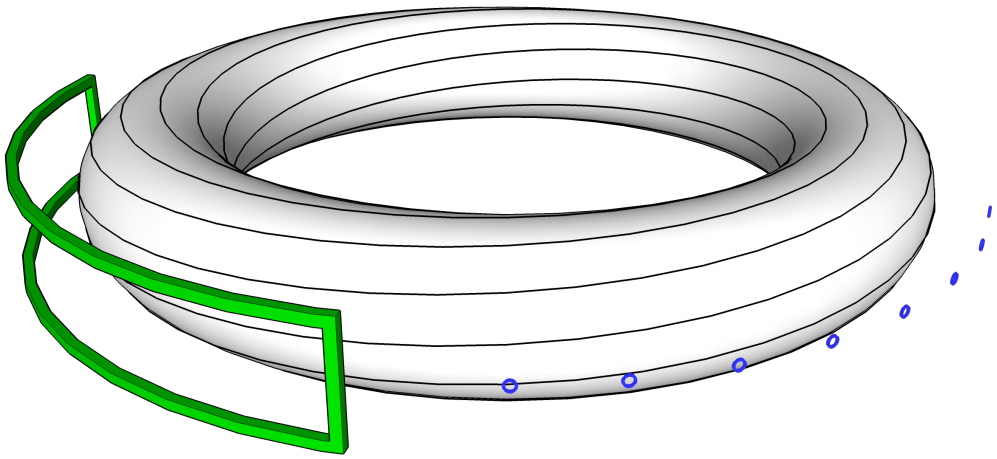

Figure 6: Schematic sketch of diagnostic coils suitable for mode detection. A saddle coil in green and an array of radial Mirnov coils to measure B_r in blue. Poloidal Mirnov coils for the measurement of B_θ are not shown and would lie in the horizontal plane.

The analysis of mode growth and structure is usually conducted using diagnostic coils placed between plasma and vacuum vessel. In doing so, one makes use of the fact, that the effect of the perturbed flux excited at an rational surface extends beyond the plasma and also affects the outer regions: If a changing magnetic field penetrates diagnostic coils, measurable voltages will be induced. These allow to measure mode dynamics and with a well positioned set of diagnostic coils it is possible to reconstruct $\Psi_1(r_s)$.

For the detection of MHD modes, Mirnov coils, a type of magnetic probes, and saddle coils are available (see figure 6).[75] Due to their small spatial extent, Mirnov coils are used to determine the toroidal and poloidal mode structure. They are aligned, such that they measure

the individual components of the local perturbed magnetic field, B_θ, B_ϕ or B_r. They can be used for fast rotating modes with frequencies of up to a few MHz.

On the other hand, saddle coils respond better to slowly rotating modes or locked modes. They give only the radial magnetic field averaged over a larger area. By knowing the mode structure the mode amplitude can be extracted from that signal.

Physics of magnetic diagnostic The principle is based on Faradays law, which is given for a static coil with only one turn by

$$U_{\text{ind}} = \dot{\Psi}_{\text{coil}} = \frac{d}{dt}\int_\Sigma \vec{B}(t,\vec{n})\cdot d\vec{S} \tag{2.40}$$

where Σ is the area enclosed by the coil.

To link the perturbed flux at the rational surface $\Psi_1(r_s)$ and the pertubed flux at the i-th diagnostic coil of a set $\Psi_1(r_{c_i})$[3] which determines $\vec{B}(t,\vec{n})$ in (2.40), the same assumption as in 2.3 are applied. We recap the solution:

$$\Psi_1(r) = \hat{\Psi}_1\left(\frac{r_s}{r}\right)^{-m}\exp[i(m\theta - n(\phi-\phi_0))] \quad \text{for} \quad r > r_s \tag{2.41}$$

With the amplitude at the resonant surface $\hat{\Psi}_1$, which is not constant in time for mode growth, and assuming the toroidal periodicity and allowing a phase shift ϕ_0, which is in case of island rotation not constant in time.

Evaluating the magnetic fields (recall equations (2.24)) at r_{c_i} gives:

$$B_{\theta/r}(r_{c_i},\theta,\phi,t) = \frac{\hat{B}_{\theta/r}(t)}{(r_{c_i}/r_s)^{m+1}}\cos(m\theta - n(\phi-\phi_0(t))) \tag{2.42}$$

For Mirnov coils, $\vec{B}$ varies only insignificantly in radial and poloidal direction within Σ. Further, they are aligned in such a way, that they only measure the radial or poloidal components of the field, $B\cdot dS = B_\theta$ or $B\cdot dS = B_r$.

This leads to the expressions for the i-th Mirnov coil on the midplane, i.e. $\theta_{c_i} = 0$:

$$I_i \equiv I_{ind,coil}(r_{c_i},\phi_{c_i},t) = \frac{\Sigma_{\text{coil}}}{R_{\text{coil}}}\frac{1}{(r_{c_i}/r_s)^{m+1}}\frac{\mathrm{d}}{\mathrm{d}t}\hat{B}_{\theta/r}(t)\cos(n(\phi_{c_i}-\phi_0(t))) \tag{2.43}$$

$$= C_i\cos(n(\phi_{c_i}-\phi_0))\frac{1}{r_{c_i}^{m+1}} \tag{2.44}$$

Where C_i is given both by $\dot{\Psi}_1(r_s)$ and the coil geometry and coil resistivity R_{coil}.

Equation (2.44) gives a relation between I_i and n. For a set of measured currents $\{I_i\}$, that equation can be fitted with n and C_i as fitting parameters to identify the toroidal mode number. By setting Mirnov coils on different poloidal positions, the poloidal mode number can be identified in a similar way. The magnetic fields can be calculated by time integration of (2.43):

[3] where the centre coordinates of each coil are defined as $(r_{c_i},\theta_{c_i},\phi_{c_i})$

$$B_{\theta/r}(r_{c_i}, 0, \phi_{c_i}, t_\mathrm{f}) = \frac{R_\mathrm{coil}}{\Sigma_\mathrm{coil}} \int_0^{t_\mathrm{f}} I_{ind,coil} \mathrm{d}t \tag{2.45}$$

$$\Leftrightarrow \hat{B}_{\theta/r}(t_\mathrm{f}) = \frac{R_\mathrm{coil}}{\Sigma_\mathrm{coil}} \frac{\cos(n(\phi_{c_i} - \phi_0(t_\mathrm{f})))}{(r_s/r_{c_i})^{m+1}} \int_0^{t_\mathrm{f}} I_{ind,coil} \mathrm{d}t \tag{2.46}$$

3. Simulation of MHD stabilities

3.1. Non-linear MHD code JOREK

JOREK is a non-linear code for solving extended MHD in realistic X-point plasma geometry including the separatrix and scrape-off layer. It has been primarily developed for simulations of Edge Localized Modes[44] but is nowadays also applied for a wide range of disruption-related simulations (see 1.5).

Reduced MHD In JOREK the so called reduced MHD equations[77],[76] derived from the extended MHD as given in 1.4 are implemented. The reduced MHD is usually applicable for the tokamak geometry and relies on two basic assumptions. The toroidal magnetic field is much stronger than the poloidal field and the toroidal field is constant over time:

$$B_\phi \gg B_\theta \tag{3.1}$$

$$\frac{\mathrm{d}B_\phi}{\mathrm{d}t} = 0 \tag{3.2}$$

This enables the description of the toroidal magnetic field through a scalar potential:

$$\begin{aligned}\vec{B} &= B_\phi + B_\theta \\ &= F_0 \nabla\phi + \nabla\Psi \times \nabla\phi\end{aligned} \tag{3.3}$$

with the constant $F_0 \equiv R_0 B_{\phi 0}$ and $\nabla\phi \equiv e_\phi / R$.

The simulation variables toroidal vorticity ω, toroidal current density j and electric potential u are then defined as:

$$\vec{v} = \vec{v}_\parallel B + R^2 \nabla\phi \times \nabla u \tag{3.4}$$

$$\omega = \nabla\phi \cdot (\nabla \times v_\perp) = \nabla_\perp^2 u \tag{3.5}$$

$$j = \nabla^* \Psi \tag{3.6}$$

The set of reduced MHD equations which are implemented in JOREK is given by:

$$\frac{\partial \rho}{\partial t} + \nabla(\rho \vec{v}) = \nabla \cdot (D \nabla \rho) + S_\rho \tag{3.7}$$

$$R\nabla \cdot \left(R^2 \rho \nabla_\perp \left(\frac{\partial u}{\partial t} \right) \right) = [R^4 \rho\omega, u] - \frac{1}{2}\left[R^2\rho, R^4 |\nabla_\perp u|^2\right] - [R^2, p^2] + [\Psi, j] - \frac{F_0}{R}\frac{\partial j}{\partial \phi} + \mu_\perp R \nabla^2 \omega \tag{3.8}$$

$$\rho F_0^2 \frac{dv_\parallel}{dt} = F_0 \frac{\partial p}{\partial \phi} - R[\Psi, p] + \mu_\parallel \nabla^2 v_\parallel \tag{3.9}$$

$$\frac{\partial \Psi}{\partial t} = R[\Psi, u] + \eta j - F_0 \frac{\partial u}{\partial \phi} \tag{3.10}$$

$$\rho \frac{\partial T}{\partial t} = -\rho(\vec{v} \cdot \nabla T)T - (\gamma - 1)\rho T \nabla \cdot \vec{v} + \nabla \cdot (\kappa_\perp \nabla_\perp T + \kappa_\parallel \nabla_\parallel T) + S_T \tag{3.11}$$

Ion and electron temperatures are assumed to be equal, so that $T_i = T_e = T/2$. S_ρ and S_T are additional, optional source terms.

For solving with JOREK, the set of equations is converted into the weak form. Detailed discussions and derivations can be found in [44], [15] and [61].

3.1.1 Numerics used in JOREK

This section touches some important aspects of the features implemented in JOREK.

Poloidal discretization The poloidal plane is discretised using bi-cubic Bezier finite elements. The grid is flux surface aligned (see 3.1.1). Introducing local coordinates for each grid element, $0 \leq s \leq 1$ and $0 \leq t \leq 1$, a simulation variable is parametrized in the form of:

$$P(s,t) = \sum_{i \leq 3, j \leq 3} P_{ij} B_i(s) B_j(t) \tag{3.12}$$

Here B are the third order Bernstein Polynomials. The 16 coefficients P_{ij} of each physical unknown are reduced so that continuity of the unknowns and their first derivatives within across element boundaries is guaranteed. They are calculated for each time step. Also the geometric variables R and Z are expressed by (3.12) which is called isoparametric mapping, which maintains the scheme's accuracy and allows for the flux alignment. Further details about the Finite Elements implemented JOREK are given in [14].

Toroidal expansion For the toroidal expansion, a real Fourier series is applied. The basis function of the zeroth harmonic equals 1. The n^{th} harmonic ($n > 0$) is given by the pair of basis functions $\cos(n\phi)$ and $\sin(n\phi)$. The harmonics to be included in a simulation have to be predefined by input parameters.

Using a Fourier expansion is intuitive since it adopts the periodicity in toroidal direction which is a fundamental property of the considered modes. To simulate a $(2/1)$ mode it is already sufficient to consider only the $n = 0$ and $n = 1$ mode. However in experiments mode coupling is often observed so that a $(2/1)$ mode may excite modes of higher order. To reproduce this behaviour the non-linear interaction between the harmonics is a crucial property of JOREK.

Time stepping Time evolution is performed using the fully implicit Crank-Nicolson scheme.[37] The advantage of implicit time schemes is that the time steps can be chosen independently of the grid size. Instead, time steps in order of the physical time scales of interest are allowed, which are usually anywhere between one and 10.000 Alfven times.

At each step the matrix representation of the weak form of the reduced MHD equations introduced above is constructed and inverted with the iterative scheme GMRES and using a physics based preconditioning involving the PaStiX[36] sparse matrix library.

Equilibrium calculation An initial poloidal grid is given by input parameters. For the flux alignment in the first simulation step the equilbirium flux surfaces are calculated based on the

Grad-Shafranov-equation:[72]

$$\nabla \cdot \frac{1}{R_0^2} \nabla \Psi = -p' - \frac{FF'}{R_0^2}, \tag{3.13}$$

where p is the pressure, $F = RB_\theta$ and the derivatives $(')$ are with respect to the poloidal flux Ψ used as a radial coordinate. The flux alignment yields computational advantages due to strongly differing magnitudes of parallel and perpendicular gradients.

The profiles of p' and FF' have to be provided as input files. Also, Ψ at the boundary of the computational domain needs to be given. All three inputs can be obtained from equilibrium reconstructions, performed by codes like CLISTE[60] based on measurements of a specific experiment.

3.1.2 Implemented Models and Extensions

Due to a broad range of applications with varying complexities, different physics models and extensions are available in JOREK. Choosing the right model makes a run more time efficient. Only the models relevant for this thesis are shortly introduced below:

Simple Physics model The simplest model describes the reduced MHD (3.7)- (3.11) only. In addition, $v_\parallel = 0$ so that only six physical unknowns are simulated: ψ, u, j, ω, ρ and T.

Model with parallel flows An extensions of the previous model is available by parallel plasma flows. The parallel velocity $v_\parallel$ becomes the seventh simulation variable and is given initially by a velocity profile. In addition, the diamagnetic drift has been implemented. The diamagnetic frequency can be scaled for theoretical studies, so that it does not necessarily need to match with the theoretical assumption of diamagnetic drift (1.6). Also, the evolution of the bootstrap current is considered. To this end the initial bootstrap current $j_{\mathrm{BS}}(0)$ is calculated from the equilibrium pressure profile by the Sauter-formula.[69] It is subtracted from the equilibrium current profile: $j_{\mathrm{ind}} \equiv j(0) - j_{\mathrm{BS}}(0)$. For each time step $j_{\mathrm{BS}}(t)$ is calculated from the evolving pressure profiles and the entire current profile is therefore given by $j(t) = j_{\mathrm{ind}} + j_{\mathrm{BS}}(t)$.

Free boundary extension STARWALL By default, JOREK uses Dirichlet conditions at the boundary of the computational domain for the magnetic flux and current. This corresponds to an ideally conducting wall placed on the boundary of the computational domain, which suppresses all perturbations there.

To describe the interaction of the plasma with a more realistic shaped respective resistive wall, but also for the implementation of active and passive coils an extension of JOREK is needed. This is enabled by the coupling of JOREK with the resistive wall code STARWALL[38],[59] . The wall is considered as a "thin wall", i.e. the current distribution that flows in conducting structures is described by an indefinitely thin current sheet. The thin wall is represented by triangles and its wall resistivity is set by an input parameter. The triangles can be calculated from a Fourier decomposition of the wall, which is given as input also. For each time step, the wall current is calculated and its back reaction onto the plasma, which is the modification of ψ at the boundary of JOREK's computational domain.

3.2. Diagnostic tools

The analysis of the plasma dynamics requires an evaluation of the simulation variables: for each time step, a series of macroscopic variables is calculated simultaneously. This includes the calculation of the total toroidal plasma current I_p or the magnetic energies $E_{\mathrm{mag,i}}$ for each harmonic. The latter is yielded by an integration of the local magnetic energy density, which is proportional to the square of the local magnetic field, given by the simulation variables. Hence it gives general information about the amplitudes and growth rates of modes with the regarding toroidal number.

Post-processing enables a more detailed analysis: physical variables like magnetic field components or electron velocities can be calculated on particular flux surfaces, averaged in poloidal and toroidal direction, or on the midplane, averaged in toroidal direction. It is also possible to perform a two dimensional Fourier analysis in straight field line coordinates[30]. For a plasma that has developed a $(2/1)$ mode, the $(m = 2, n = 1)$ component of ψ read out at $\Psi_N(q = 2)$ corresponds to the helical perturbed flux Ψ_1 at the rational surface then.

Poincare plots[18] enable to visualize the field line structure: Starting from a poloidal plane, several field lines are traced for many toroidal turns an their position is marked every time they cut the plane at which they were started. This way, field lines starting from a flux surface map out the respective flux surfaces - both from the unperturbed plasma or from an island. In contrary, the mapping will proceed rather chaotic if the lines lie in a stochastic layer. The Poincare plot can be written out in $R - Z$ as well as in $\Psi_N - \theta$-coordinates.

Part II.
Results

4. Virtual diagnostic signals of a (2/1) locked mode

In order to compare simulation data directly to experiments, virtual diagnostic coils are needed. JOREK has the capability to simulate virtual diagnostic coils using the free boundary extension STARWALL. For this work, a set of diagnostic coils was set up such that virtual signals can be written out in response to the MHD activity. The different set-ups implemented for this series of simulations are given in 4.2. In the following sections we will validate if the behaviour of the coil signals that is predicted by the formulas derived in 2.6 for the vacuum field in simple geometry also holds for a realistic case.

In this first application of virtual diagnostic coils, we consider a classical born locked mode that gets excited by an artificial heat sink mimicking the situation caused by massive material injection for disruption mitigation (see 4.1). The locking mechanism itself is not of interest in this section, but is studied in section 6.

4.1. Plasma setup

The simulations are based on a typical ASDEX Upgrade L-mode equilibrium with $q_0 = 1.12$ and $q_{95} = 4.67$. The $q = 2$ rational surface lies at $\Psi_N \approx 0.54$ and the magnetic axis is located at $(R_{\text{axis}}, Z_{\text{axis}}) = (1.66\,\text{m}, 0.075\,\text{m})$. The $(2/1)$ mode is linearly stable in this equilibrium and gets excited by an artificial heat perturbation as explained in the next section. The simple physics model implemented in JOREK (see 3.1.2, Simple Physics model) is sufficient here, since the main purpose of this section is to investigate signal diagnostic coils applied to a locked mode. In order to investigate the influence of non-linear coupling with higher harmonics on the MHD modes and coil signals, simulations including toroidal harmonics from $n = 0, 1$ up to $n = 0, ..., 5$ are carried out.

Source terms and diffusivities were set up such that density and temperature profiles are stationary in the absence of modes on the considered timescales. Further scans have been performed to check the convergence of the results with the grid resolution. For this simple case of only one tearing mode in a plasma that is stable against any other modes, a low spatial resolution, compared to similar simulations, of the poloidal grid is sufficient to describe the dynamics: the grid is constructed from 40 nodes in the radial directions times 50 points in the poloidal direction.

4.1.1 Triggering a born-locked mode

Due to the strong dependency of resistivity on temperature, $\eta \propto T^{3/2}$[12], a temperature perturbation will be followed by a current perturbation. On one hand, this can lead to axisymmetric modification of current distribution. If this implies a steepening of current gradient around a rational surface, a tearing mode may get destabilized. On the other hand a non-axisymmetric, periodic perturbation can also enforce island growth. Thus, by introducing a

non-rotating temperature perturbation, a non-rotating mode structure is induced, where the O-Point is aligned with the perturbation. This triggering is comparable to massive material injection used for disruption mitigation[56].

Therefore an additional term S_{HS} describing a "thermal energy sink" was added to the temperature source term S_T in JOREK. The radially, poloidally and toroidally localized heat sink is placed at the $q = 2$ surface on the low field side. Intensity is time varying with a maximum after $t = 2000\,\tau_A$[4] according to the temporal dependency $\exp\left[-(t-2000)^2/1500^2\right]$.

4.2. Coil setup

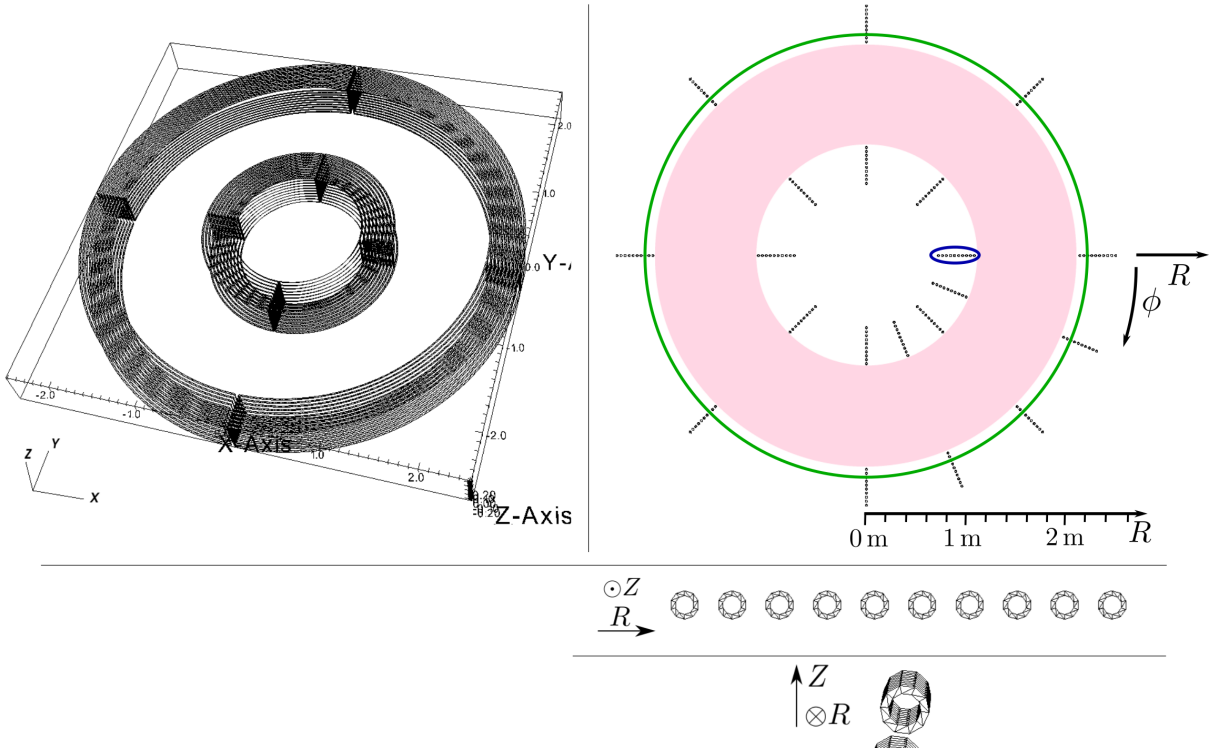

Figure 7: Left: Model of the saddle coils. Right: Positions of the Mirnov coils. Toroidal subset (see 4.4.1) at $R = 2.222\,\mathrm{m}$ is marked in green; Radial subset (see 4.4.2) at $\phi = 0$ is marked in blue. Below: Horizontal Mirnov coils for the measurement of B_θ. Far below: Vertical Mirnov coils for the measurement of B_r.

Four saddle loop coils measuring the radial magnetic field are installed on the high field side of ASDEX Upgrade centred around the midplane at $R = 1.0845\,\mathrm{m}$ next to each other, each spanning a toroidal angle of $\Delta\phi = \pi/2$ and having a height of $\Delta Z = 452\,\mathrm{mm}$. The same coils are implemented with STARWALL as virtual diagnostic coils. Two further saddle coils at the same radial position R have been added, such that all toroidal angles are covered. In addition virtual coils with different distance to the plasma, i.e. from $R = 1.0445\,\mathrm{m}$ to $R = 0.7245\,\mathrm{m}$ on high field side, and further coils on the low field side, i.e. from $R = 2.142\,\mathrm{m}$

[4] All times within this thesis are normalized with respect to Alfven time scale. Multiplying t by $\tau_A = \sqrt{\mu_0 \rho_0}$ yields the time in seconds, where ρ_0 is the central mass density. For these simulations $\tau_A \approx 3 \cdot 10^{-7}\,\mathrm{s}$.

to $R = 2.502\,\mathrm{m}$, are considered (see figure 7). They are centred around the $Z = 0$-plane and therefore the center is below the magnetic axis ($Z_{\mathrm{axis}} = 0.075\,\mathrm{m}$).

To analyse the toroidal dependency of the signal in more detail, a set of horizontally and a set of vertically aligned Mirnov coils each with a diameter of $2\,\mathrm{cm}$ are implemented in addition at ten toroidal positions and at the same radial position as the saddle coils. They are adjusted in such a way that one set can measure B_r and the other set measures B_θ.

This broad set of 480 virtual diagnostic coils enables to investigate radial and toroidal dependency of measured signals. Therefore they can be compared with the theoretical derivations for a cylindrical, large aspect ratio geometry given in 2.6. The resistivity of all coils has been set to very high values, so that magnetic fields driven by I_{coil} are negligible relative to equilibrium or tearing mode fields and back reaction to the plasma is excluded.

4.3. Evolution of the plasma

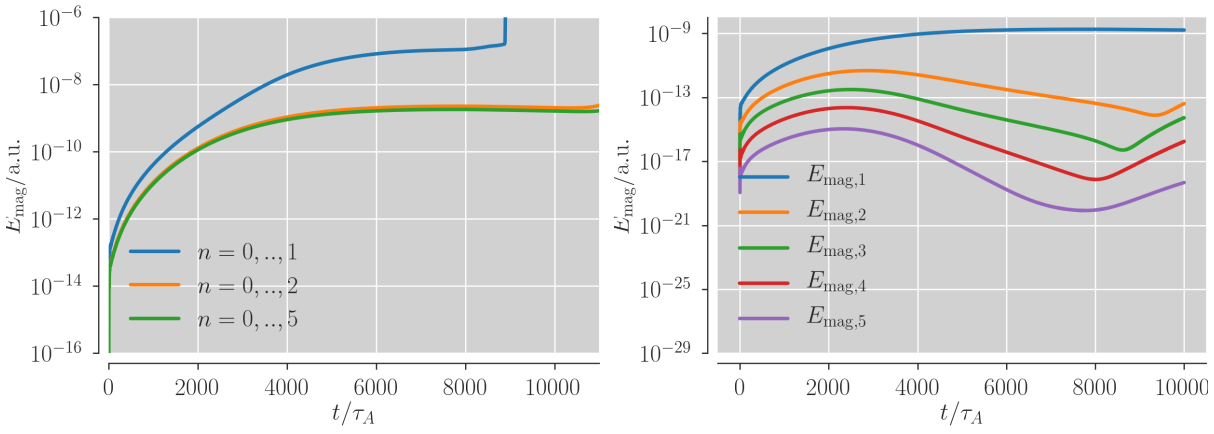

(a) (b)

Figure 8: (a) Magnetic energy of the first harmonic for some runs with different number of harmonics. Including at least $n = 0, ..., 2$ is required for convergent results. The $n = 0, 1$ simulations ends with a numerical instability at $t = 8400\,\tau_A$. (b) Magnetic energies of all harmonics of the $n = 0, ..., 5$ simulation. Apparently the first harmonic is dominating.

Excitation of the tearing mode promptly sets in within the first time steps, since $S_{HS}(t = 0)$ already has a significant amplitude. This results in a monotonously increasing magnetic energy of the first harmonic, $E_{\mathrm{mag},1}$, in all simulations. In the $n = 0, 1, 2$ simulation and at $t = 4000\,\tau_A$ that energy reaches $1 \cdot 10^{-9}$, while the amplitude of cooling sources drops below 1% of its maximum amplitude at $t = 2000\,\tau_A$. The energy growth rate decreases later on, so that the energy reaches a plateau of $\approx 1.6 \cdot 10^{-9}$ only at $t \approx 6000\,\tau_A$. At that time point an island structure is visible with a width of $25\,\mathrm{mm}$ (5% of minor radius) on the low field side. As expected, the O-Point on low field side is exactly centred around the position of the cooling source (see figure 9). During the mode growth q_0 drops to a value slightly below 1 whereby the $q = 2$ surface moves outwards by $\Delta\Psi_n \approx 0.03$, which is around half island width on the

low field side. In the last sequence, for $t > 8000\,\tau_A$ it can be observed that the islands width decreases slowly.

Taking more than the first two harmonics into account shows a strong convergence, thus the time trace of $E_{\mathrm{mag},1}$ does not change largely. In contrary the simulation with only $n = 0, 1$ is under resolved, so that it exhibits energies two order of magnitude higher and develops significant numerical instabilities in the centre after $t = 8000\,\tau_A$, causing it to diverge.

Additional modes of higher mode numbers develops slightly, what could be explained both by weakly mode coupling but also by helical currents on other rational surfaces that were also induced by the heat sink. Comparing island widths and mode amplitudes, which are extracted using a Fourier Transformation (see also 4.4.3) show, that the $(2/1)$ still remains to be the dominant mode.

In the following we will study the virtual coil signals caused by this MHD activity.

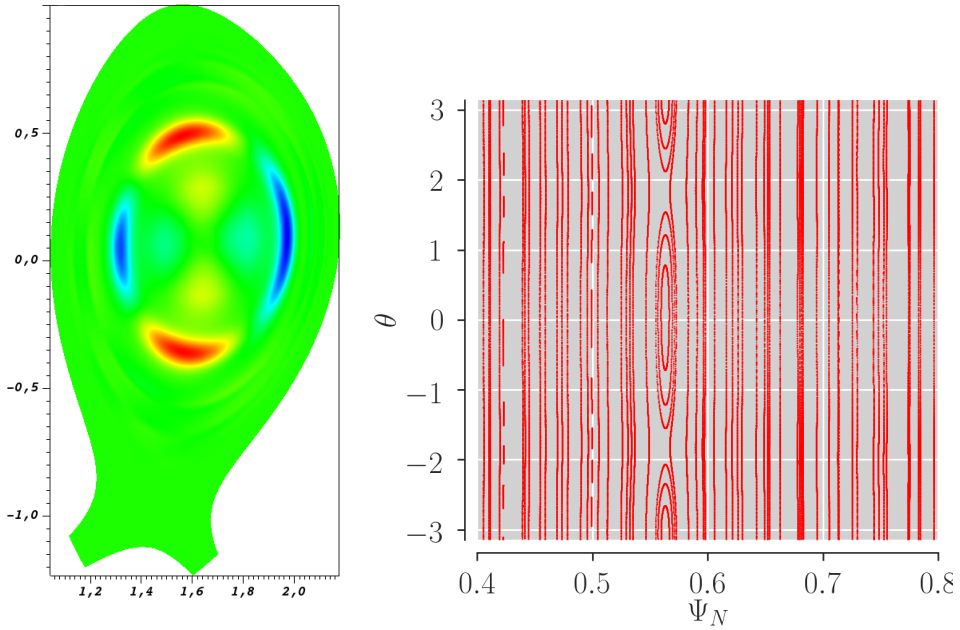

(a) (b)

Figure 9: (a) Current density distribution j of the first harmonic for $t = 6000\,\tau_A$. (b) Poincare plot showing the $(2/1)$ island at $\Psi_N \approx 0.56$ at the same time. Other modes are only weakly developed, since mode coupling is limited at this $(2/1)$ mode amplitude.

4.4. Analysis of the coil signals

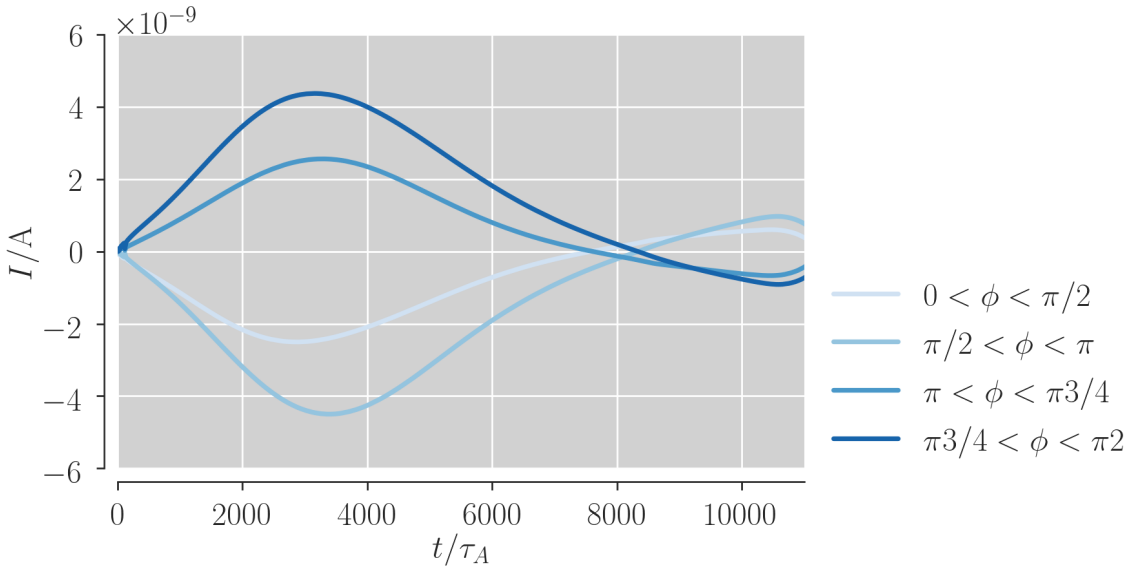

Figure 10: Time trace of the saddle coils on the high field side at $R = 1.0845\,\mathrm{m}$ from the $n = 0, ...5$-simulation. The labels indicate the toroidal angle each coil covers.

For each coil, the time trace of the measured current $I_{\mathrm{coil,i}}$ are documented. The signal amplitude, which are a proxy for the islands growth rate, vary strongly by the toroidal position, as can be seen in figure 10. All time traces for the coils of the simulations with at least $n = 0, 1, 2$ exhibit a local maximum of the absolute value after around $t = (3700 \pm 200)\,\tau_A$, the exact time point varies for each coil angle or coil setup. After reaching the maximum, the signal amplitude decreases, what is in agreement with a slowing down of energy and island growth shown before. After $t \approx 8000$ signal signs change, indicating the observed damping of the mode.

4.4.1 Toroidal dependency

The question arises how well the wave number n of the mode and its phase shift in toroidal direction can be identified from the diagnostic coils. Therefore we choose from one set of coils those coils which are at a specific radial position and analyse the signal at a specific timepoint t. We call this selection a "toroidal subset" as it is marked in figure 7. Therefore we have 30 of these kind of subsets in total.

For the investigation we simplify $C_i/r_{c_i}^{m+1}$ in (2.43) by $C_j^\dagger$ with $0 < j \leq 30$ for each toroidal subset. Then using modified (2.43) as a fitting function

$$I_i = C_j^\dagger \sin(n_j(\phi_i - \phi_{0,j})), \tag{4.1}$$

all n_j and $\phi_{0,j}$ are determined using a non-linear least-square fit[66]. The time point is set to $t = 6000\,\tau_A$ at which the signals have already grown to a significant amplitude but do not exhibit anomalies due to numerical instabilities.

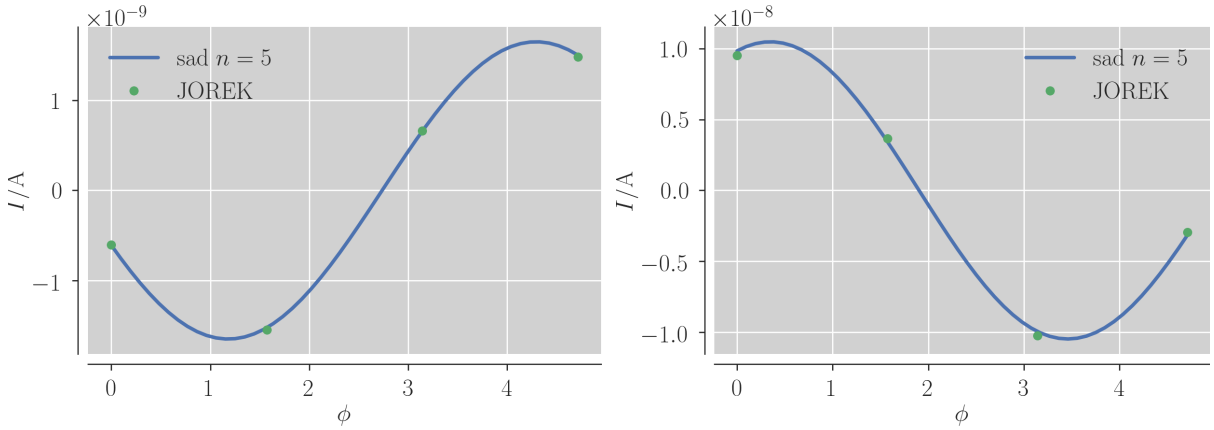

(a) High field side (b) Low field side

Figure 11: Saddle coils at the position of $R = 1.0045\,\mathrm{m}$

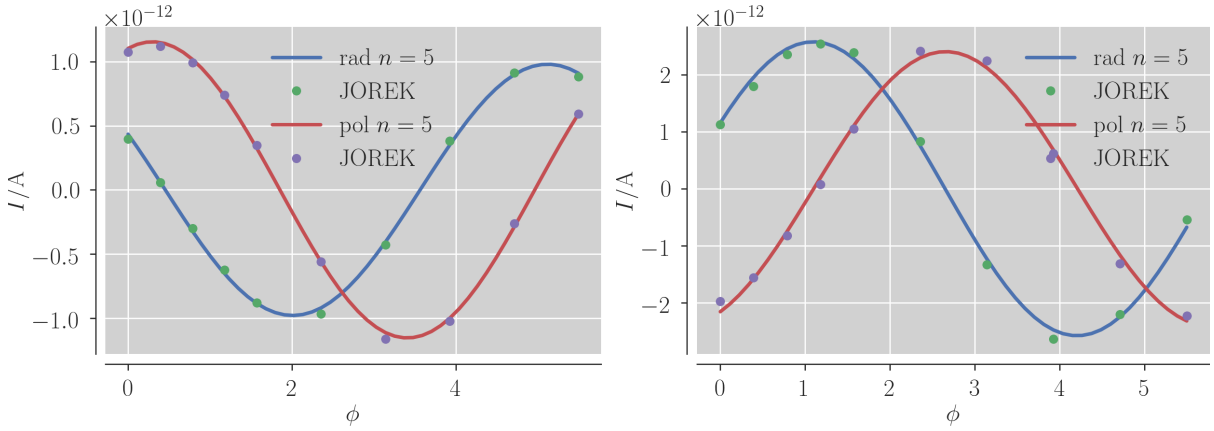

(a) High field side (b) Low field side

Figure 12: Mirnov coils at the position of $R = 1.0045\,\mathrm{m}$

If (4.1) is fitted to mode signal from the $n = 0, 1$-simulation, it shows clearly a periodicity of $n_j = 1$, which is expected, since that simulation only considers the first harmonics, $\cos(\phi)$ and $\sin(\phi)$ in the toroidal expansion. The periodicity becomes non-trivial by including higher harmonics. Applying the fit to any of the other simulation shows a good agreement still. The relative error between measured points and the optimized function is only about up to 1%[5] which is tolerable. This implies that side modes with higher mode numbers do not perturb the signal too strongly and the periodic structure of a $n = 1$ mode clearly dominates.

Since the thermal sink is placed at the position $\phi = 0$ one would expect the maximum of B_θ respective $B_r = 0$ at this position, what would imply no phase shift for the signal of vertical Mirnov coils and a phase shift of $\pi/2$ for the horizontal ones. However all subsets at high field side exhibit a positive phase shift of about $(0.08 \pm 0.01)\pi$, while the signals on low field side lag behind with $-(0.14 \pm 0.02)\pi$. This is a result of the displacement of the

[5]Error defined by $\Delta \equiv (n^{-1} \sum_i^n |y_i/f(x_i)|) - 1$

coils of $0.075\,\mathrm{m}$ relative to the magnetic axis. Therefore the smallest distance between coils and an O-point is not reached at $\phi = 0$ exactly. With increasing ϕ the O-point on high field side moves "downwards" on the poloidal plane and reaches the minimal distance to the coils at around $\phi = 0.08\pi$. The reverse phenomenon applies for the low field side. It should be a result of the toroidicty that the additional phase shift is greater on the high field side than on the low field side.

This misalignment however also implies that the horizontal respective vertical Mirnov coils will also measure small amount of B_θ respective B_r, which decreases with increasing distance to the plasma. This might influence the radial behaviour of the signal which is analysed in the next section.

4.4.2 Radial Decay

It is of interest how well the radial dependency derived for a simple geometry in chapter 2.6 fits for a realistic case. In case of sufficient agreement, the mode amplitude can easily be reconstructed from the measured coil signal. To this end it is analysed in the following if the measured signals decay like r^{-m-1}.

We investigate the radial dependency for each toroidal position and field side, i.e. for each "radial subset" (see figure 7) separately. We define $C_i \sin(n(\phi_i - \phi_0))$ in (2.43) as $C_j^\dagger$, $0 < j \leq 48$ for each subset of Mirnov coils. For saddle coils the term is replaced by $C_j^\dagger R$. The multiplication with R takes into account that $\Sigma_{\mathrm{saddlecoil}} = \pi/2R\Delta Z \propto R$. Therefore $C_i^\dagger$ remains independent R. The minor radius can be expressed as $r_{c,i} = R_i - R_{\mathrm{axis}}$ since the coils are centred around midplane. For a fixed time point $t = 4000\,\tau_A$, we take the signal of each coil from a subset. Then using modified (2.43) as fitting functions,

$$I_i = C_j^\dagger \frac{1}{(R_i - R_{\mathrm{axis}})^{m_j+1}} \quad \text{for Mirnov coils}$$

$$I_i = C_j^\dagger \frac{R}{(R_i - R_{\mathrm{axis}})^{m_j+1}} \quad \text{for saddle coils}$$

we optimize to find expressions for C_j setting $m_j = m = 2$ in the first step using a non-linear least-square fit. In the second step we optimize for m_j and C_j simultaneously to check if the signals decrease with a power of r that is systematically differing from $-(m+1)$. This is carried out for the coil signals of all simulations separately.

For some subsets the mode amplitudes of coils close to the plasma deviates strongly from the r^{-m-1}-behaviour (see figure 13,14,15). This is the case, when the coils are unrealistically close to the plasma. A higher resolution of the coils discretized by planar triangles would be needed to resolve this numerical artefact. Therefore the corresponding coils are excluded from the fitting.

The quality of the fits varies only weakly with the number of harmonics in the simulation. That means that the deviations discussed here, are observed in all simulations in a very similar manner. Instead the toroidal position, but also the type of coils has a much bigger impact. In summary the signal agree with the first by $\Delta \approx 2\%$ if it is taken by Mirnov coils at a position where the amplitude is the strongest. This is the case for horizontal Mirnov coils at $\phi \approx \pi/8$ and high field side or vertical Mirnov coils at $\phi \approx 3\pi/8$ (see figure 12). The good agreement

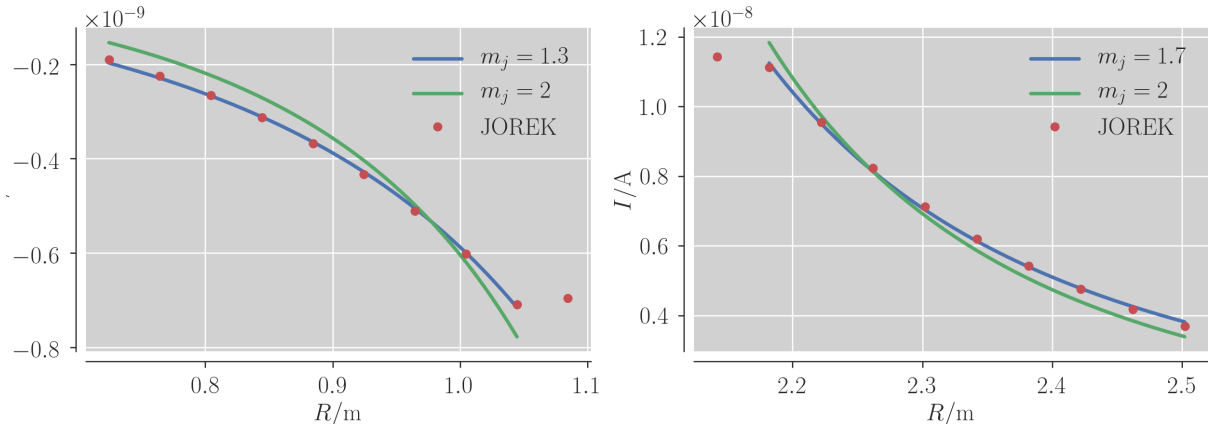

(a) High field side (b) Low field side

Figure 13: Saddle coils at the position of $0 < \phi < \pi/2$

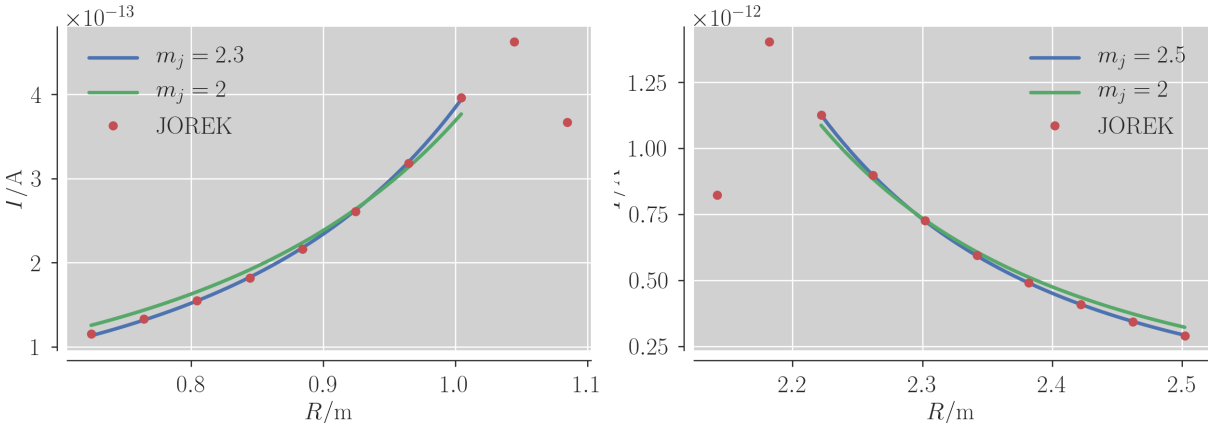

(a) High field side (b) Low field side

Figure 14: Mirnov coils measuring B_r at the position of $\phi = 0$

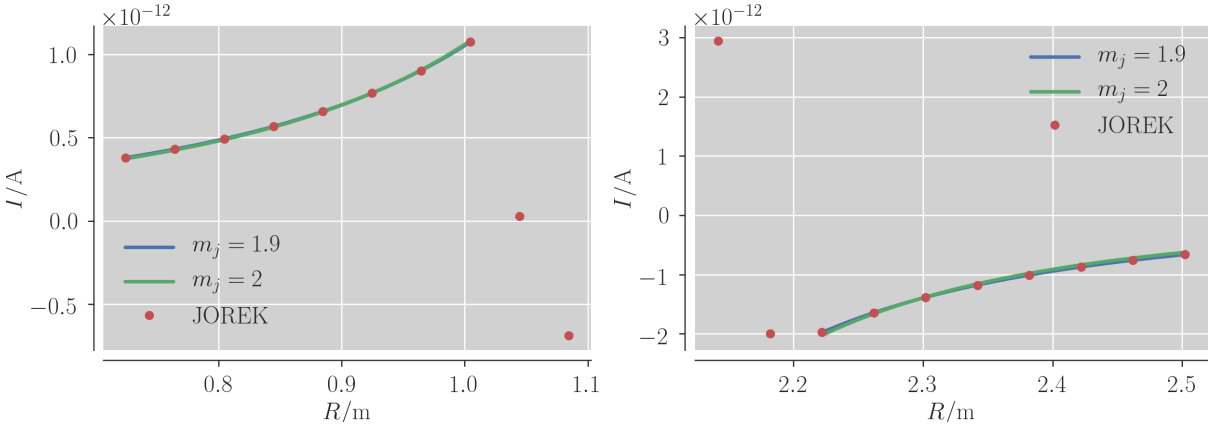

(a) High field side (b) Low field side

Figure 15: Mirnov coils measuring B_θ at the position of $\phi = 0$

holds for horizontal coils also at $\phi = 0$, where the amplitude is still sufficient high (see figure 15).

For the saddle coils with high amplitude a deviation of around 5% is identified.

By fitting m_j also, the quality of the fits improves in nearly all cases and the deviation is below $< 0.2\%$. Yielded m_j are in a range between 1.0 and 3.0, a clear trend between coil position and m_j is not identifiable however. As an effect of toroidicity and shaping the magnetic island on low field side is significantly bigger in direction of θ (see figure 9). This could imply $m_j < 2$ for low field side and m_j for high field side. Given the fact that there is also no correlation between field side and m_j (e.g $m_j < 1$ for all saddle coils) the observed deviations are likely not to be explicable as geometric effects only.

As explained before the magnetic field perpendicular to a coil is not exactly defined by only one component, B_r or B_θ. Instead, a small amount of the other component is added and that amount is dependent of the radial coil position. This perturbation may lead to the deviation of signals from the theoretical decay with $r^{-(m+1)}$. At those toroidal positions where one component reaches a maximum, the other component vanishes and hence the perturbation also. This is in agreement with the observation that the fit yields smallest deviations at these positions.

4.4.3 Comparison with the magnetic flux at the rational surface

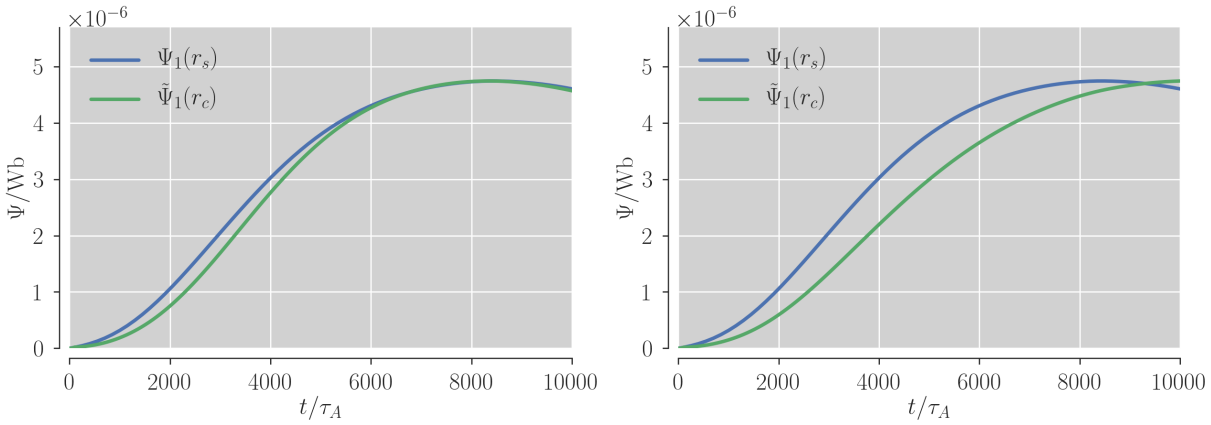

(a) High field side

(b) Low field side

Figure 16: Saddle coils. For a better comparison $\tilde{\Psi}_1(r_c)$ has been scaled so that $\max \Psi_1(r_s) = \max \tilde{\Psi}_1(r_c)$

By a two dimensional Fourier analysis (see 3.2) the helical perturbed flux $\Psi_1(r_s)$ is determined. Moreover $\Psi_1(r_c)$ can be estimated except for a constant by the integration of the measured current: $\Psi_1(r_c) \propto \int_0^t I_i(t')dt' \equiv \tilde{\Psi}_1(r_c)$.

Regarding the Fourier analysis $\Psi_1(r_s)$ grows rapidly between $t \approx 1000$ and $t \approx 5000$ and reaches a maximum value at about $t \approx 8000$. This is in good agreement with the growth of island width described before. The integrated signals of the coils on high field side match well (see figure 16 for saddle coils). During the rapid growth the signals exhibit a slightly delay of $\delta t < 300$, while it is about $\delta t < 1000$ on the low field side. The delay can be explained qualitatively by the shielding effect the remaining plasma outside r_s has.

A similar behaviour is detected by the Mirnov coils, albeit the lagging is only $\delta t < 100$ during the rapid growth. There is a tendency, independent from the type of coils, that the

signal on low field side is less delayed than on low field side.

4.5. Conclusions

In this sequence of simulations the generation of diagnostic coil signals for the detection of tearing modes using a simple reduced MHD model and realistic geometry has been realized. Both saddle and Mirnov coils were implemented and their appropriateness for analysing a $(2/1)$ mode were compared. The signals were examined for their consistency and compared with theoretical expectations.

Toroidal periodicity of the coil signals corresponds well to the periodicity of the $(2/1)$. This means by using a sufficient number of Mirnov coils the mode and its phase shift can be identified easily. It was also checked how well the radial decay of the amplitude can be predicted. At positions where B_r respective B_θ reaches its maximum, the decay matches well with expected prediction for simple geometries. It is important to keep in mind the delay between mode growth and coil signal due to a skin effect of the outer plasma. This needs to be quantified in further simulations correctly especially if coils are used for investigation of a rotating mode: The inverse of the delay gives an upper limit for observable rotation frequencies.

Another effect which is of possible relevance is the variation of the position of the rational surface. In this simulation, it changed only slightly, as it moved outwards, i.e. about 2 cm on the low field side. That would imply an increase in the coil signal due to the $r^{-(m+1)}$ dependence, and could be wrongly interpreted as a a mode growth. This effect seemed not to be significant here. Future studies should also investigate this in more detail.

5. Simulation of a partial thermal quench

The dynamics of a $(2/1)$ locked mode that leads to a thermal quench are investigated in the following using a more realistic physics model and plasma setup. An equilibrium, which is unstable against the mode is considered. The current density profile of an ASDEX Upgrade equilibrium was modified for this purpose to destabilize the mode, i.e. $\Delta' > 0$ is fulfilled. The focus lies on the linear development and evolution of the stochastic layer and its influence onto the temperature profile. Wall setups with different resistivities and geometries are considered.

It shall be analysed how the mode coupling introduced in 2.5 behaves in a realistic toroidal system: it is expected to observe the coupling of poloidal mode numbers due to toroidicity effects soon after the onset of the $(2/1)$ mode and the quadratic mode coupling with modes of higher toroidal harmonics in the later course. It is analysed if the time points of island overlapping corresponds to the onset of stochasticity, as predicted by the Chirikov criterion.

The conducting structure has a stabilizing effect onto mode growth and saturation amplitudes (see 2.3). On the one hand a decrease of the growth rate of the $(2/1)$ mode and hence its side bands is expected. In addition the wall could also have a direct influence on the side bands amplitudes, especially if they lie much closer to the wall than the $(2/1)$ mode. As an another effect, the conducting wall may have a suppressing effect on the stochastisation in particular at the plasma edge. Even at the same amplitude of the $(2/1)$ mode, stochastisation at the plasma edge is expected to reduce for decreasing resistivity of a wall close to the plasma.

Next, it will be analysed how the occurrence of modes and stochastisation will degrade energy confinement. For large islands of a widths some multiples of the critical island width regarding Fitzpatrick, a flattening of the temperature profile is expected, like discussed in Section 2.2.2. Based on the simulation it will be investigated, which modes have a significant influence hereby. Besides these direct island effects, also stochastisation is expected to contribute to the radial transport for high heat diffusion anisotropies.

In light of disruption prediction, many attempts have been made over the years to find an empirical estimate for the $(2/1)$ amplitude observed at the onset of a thermal quench. One common threshold is referred as the deVries-scaling law[85]. To discuss its validity, it will be applied to these simulations in the end of the chapter and further dependencies on geometry neglected in this scaling are discussed.

5.1. Plasma and wall setup

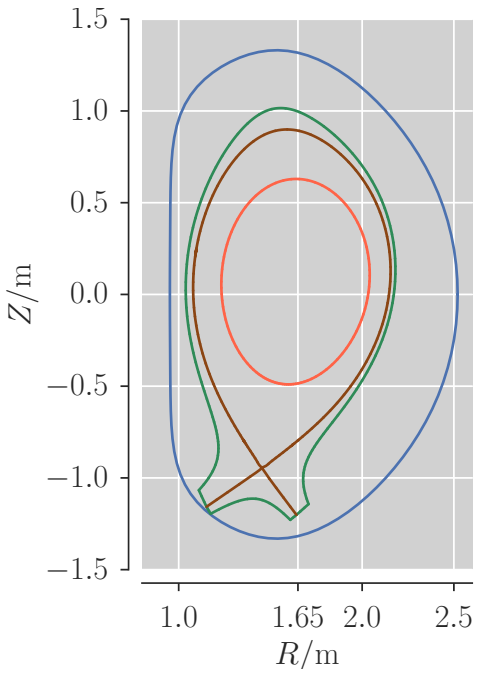

Figure 17

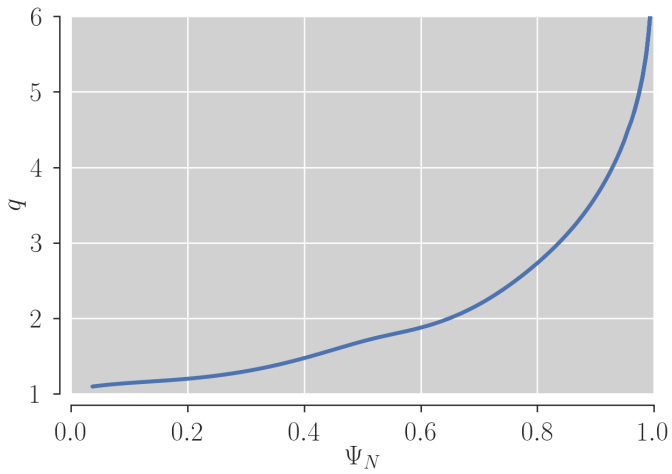

Figure 18

Figure 17: Blue line: Poloidal cross section of the vacuum vessel of ASDEX Upgrade as used for this simulations. Green line: Boundary of the computational domain and ideal wall of the simulation with fixed boundary conditions. Brown line: Separatrix. Orange line: Cross section of the $q = 2$-surface. Figure 18: Q-profile with $q_0 = 1.05$ and $q_{95} = 4.35$.

A similiar equilibrium like set up in section 4 is considered. The $q = 2$-surface is given at $\Psi_N = 0.65$ here. The slight shift is a result of an adjustment of B_ϕ to avoid having a $q = 1$ rational surface in the plasma. The current gradient between $\Psi_N \approx 0.55$ and $\Psi_N \approx 0.75$ is increased to destabilize the $(2/1)$ mode. This also flattens the q-profile around the resonant surface, which remains to increase monotonously still (see figure 18). The plasma is rather cold with an electron temperature of $4\,\mathrm{keV}$ in the core and $0.6\,\mathrm{keV}$ at the $q = 2$-surface.

Simulations are carried out with four different boundary configurations. For the first simulation, fixed boundary conditions are applied, i.e. an ideal wall is placed on the border of the computational domain (green curve in figure 17).

The further simulations make use of STARWALL to represent the vacuum vessel of ASDEX Upgrade (blue curve in figure 17): the vacuum vessel consists of eight electrically insulated octants, and is made of 4311 Cr-Ni Austenitic Stainless Steel.[84] The insulated gaps are bypassed with metallic bellows. Further features like ports make its structure more complex. Hence the resistance of the vacuum vessel is inhomogeneous and increased compared to a one-piece vessel.[33] The representation used here by a thin closed wall with constant resistivity is a strong simplification. Since only the general interaction of MHD modes with a conducting wall are of interest here, without the aim of quantitatively comparing to experiments, this problem is not further discussed for now.

The vessel has an maximum wall thickness of $d = 15\,\mathrm{mm}$ and a toroidal resistivity of $R = 0.28\,\mathrm{m\Omega}$. It has an approximate major radius, averaged over the outer and inner radius of the vessel, of $R_M = 1.75\,\mathrm{m}$ and the poloidal cross section has an area of about $A = 0.1\,\mathrm{m}^2$. This yields a resistivity of $\rho_w = RA/(R_M 2\pi) = 2.6 \cdot 10^{-6}\Omega\mathrm{m}$. The 4311 Steel has a resistivity of around $1 \cdot 10^{-6}\Omega\mathrm{m}$ for usual operating temperatures. The assumption of a higher resistivity as for the pure material is reasonable due to the structure of the vessel.

For the second simulation, this realistic resistivity is set and the ASDEX Upgrade like vessel as depicted in figure is implemented. The resistivity is increased or decreased by a factor of 10^6 in the third or fourth simulations, respectively to study the ideal vacuum vessel and the no-wall limit.

The simulations are carried out with the physics model including parallel velocity, see 3.1.2. This model also consistently describes the evolution of the bootstrap current following the kinetic profiles, such that the neoclassical drive of the island is accounted for. To yield virtually locked modes from the beginning, the toroidal rotation, E-cross-B background drifts and diamagnetic drifts are set to zero. The parallel heat conductivity scales with $\propto T_e^{5/2}$ and is set, such that it matches the theoretical Spitzer-Härm conductivity at the rational surface, $\chi_\parallel(\Psi_N = 0.65) = 1.22 \cdot 10^{-9}\,\mathrm{m}^2/\mathrm{s}$. (with $T_e = 650\,\mathrm{eV}$ and $n_e = 1.33 \cdot 10^{19}\,\mathrm{m}^{-3}$ at the rational surface). To allow for coupling with high order modes, the simulations are carried out with the first five toroidal harmonics, regarding the observations in the last chapter.

5.2. Analysis of the plasma

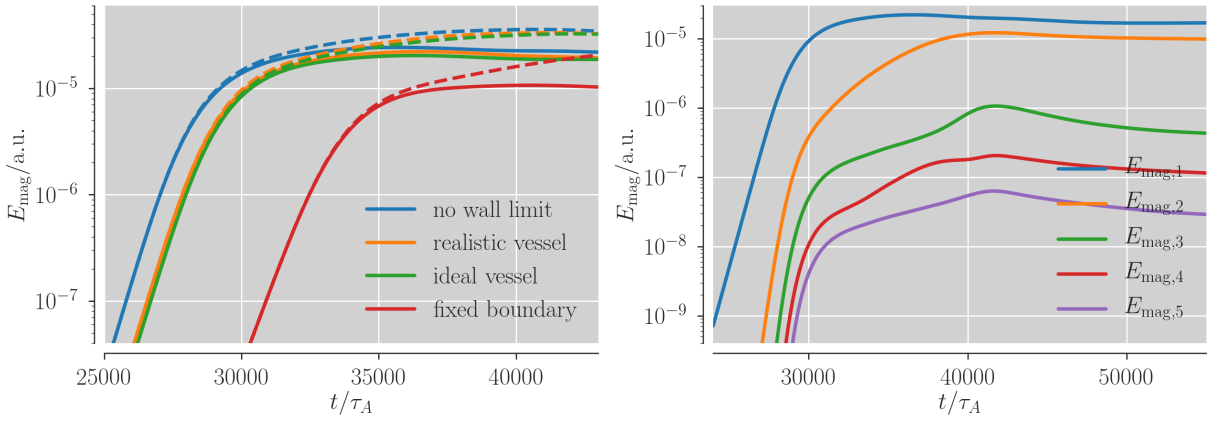

(a) (b)

Figure 19: (a) Time traces of the magnetic energy of the first harmonic (solid line) and the sum of the magnetic energies of all the first five harmonics (dashed line) for different wall configurations. (b) The magnetic energies for the first five harmonics separately for simulation with realistic vacuum vessel.

As expected, the $(2/1)$ mode starts growing soon after initialising each simulation and clearly dominates modes of higher order during its linear phase. The different boundary conditions influence the mode growth significantly so that the growth rate of the first harmonic in the run with fixed boundary is about 20% smaller compared the no-wall limit and saturates later(see figure 19 (a)). The differences between the runs with ASDEX Upgrade like vessel are substantially smaller: the growth rate for realistic vacuum vessel is just 4% smaller. The difference growth rates also impact the saturated energy amplitudes, so that $\max E_{\mathrm{mag},1}$ is one order of magnitude lower for the run with fixed boundary compared to the other runs. With entering the non-linear phase between $t = 27000\,\tau_A$ to $t = 35000\,\tau_A$, modes of higher order become significant for all runs. The sum of the $n = 2, ..., 5$ magnetic energies gets comparable to $E_{\mathrm{mag},1}$. In the further course $E_{\mathrm{mag},1}$ stops growing in all runs. However modes of higher order continue to grow, so that $E_{\mathrm{mag,sum}}$ reaches a maximum, when $E_{\mathrm{mag},1}$ has already decreased by around $20\,\%$ in each run. Modes with $n = 2$ reach a magnetic energy in the same order of magnitude as the $n = 1$-modes (see figure 19 (b)).

The current density profile rearranges in the stochastic region, but is kept constant at the magnetic axis and the toroidal plasma current I_p, which is initially $I_p = 0.988\,\mathrm{MA}$ varies less than 2% until $t = 70000\,\tau_A$ during each simulation. Only weak variations of the q-profile are observable.

5.2.1 Development of the Stochastisation

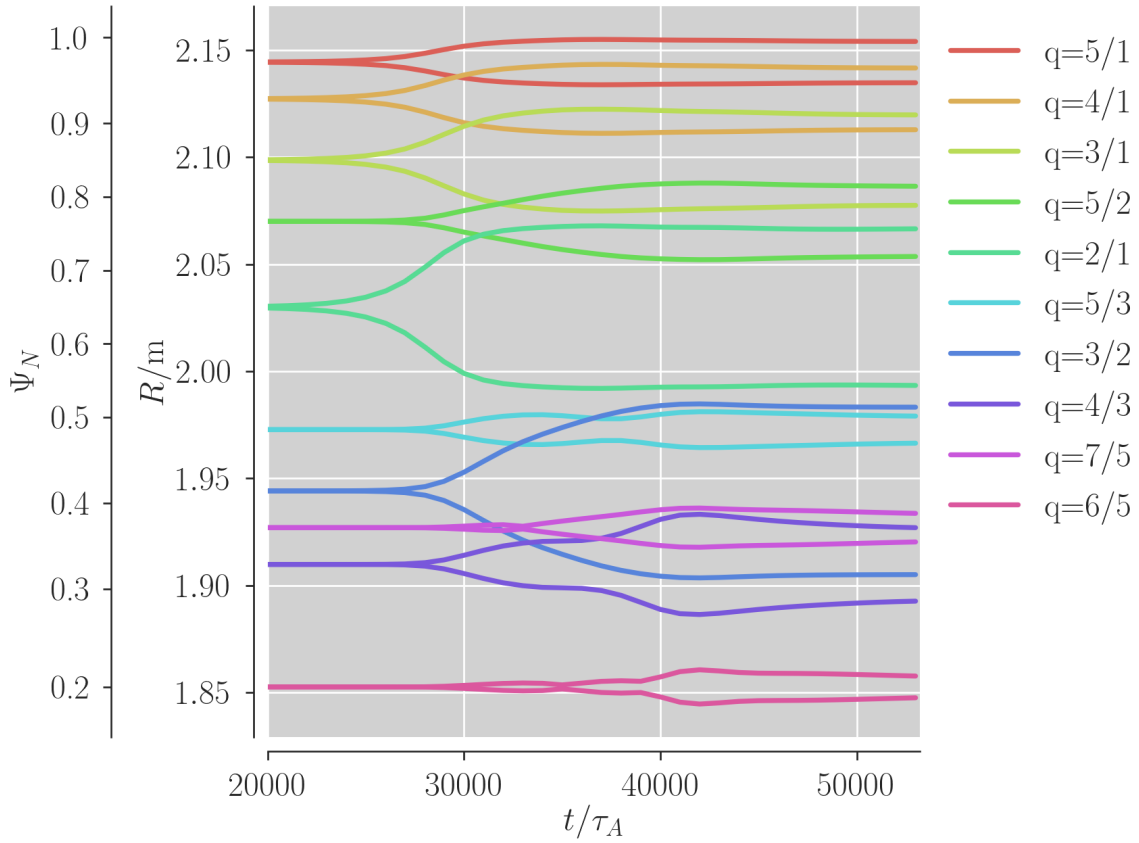

Figure 20: Time trace of the island widths for the run width realistic vacuum vessel. The widths of all islands, which grow at least to 3% of the minor radius, respective get clearly visible in the Poincare plots, are drawn.

Equation (2.28) gives an expression for the island width of a circular plasma and high aspect ratio in terms of the perturbed magnetic flux. Based on this equation, the island widths for this realistic plasma are calculated from:

$$W = 0.7 \cdot 4 \frac{\Psi_{n,m} q}{B_\theta q'} \tag{5.1}$$

All variables are extracted from the simulation and $\Psi_{n,m}$ is given by a Fourier-Transformation like introduced in 4.4.3. The prefactor 0.7 takes account of island compression due to toroidal and shaping effects and is determined empirically by comparing the width predicted by (2.28) for the $(2/1)$ island and the actual width read out manually from Poincare plots at some time points. A comparison of (5.1) with the island widths of further modes shows a good agreement with deviations $< 7\%$ independent of time step or simulation. A similar approach has been applied in [78].

By this, the time traces of island widths are calculated for each simulation. Island widths for the run with realistic vacuum vessel are shown in figure 20. That simulation is discussed in detail in the next paragraphs.

At $t = 25000\,\tau_A$, the $(2/1)$ island becomes visible agreeing with the fact that the linear phase ends. Simultaneously, the $(3/1)$ and $(4/1)$ modes become visible (see figure 22, first). Due to the steep gradient of q for $\Psi_N > 0.8$ (see figure 18), the rational surfaces $q = 3, 4, 5$ lie close to each other rendering this region prone to stochastisation soon after the appearance of sideband harmonics. Actually stochastisation gets visible at $t = 30000$, which is in agreement with island overlapping as depicted in figure 20. At the same time, the non-linear coupling of modes of the first harmonic, leads to the occurence of $n = 2$ modes. Due to the low mode number, the $(3/2)$ mode dominates here, agreeing with the predictions from the energy principle introduced in 2.2. Due to slight overlapping with $(5/3)$ and $(4/3)$ island, stochastisation also sets in around $\Psi_N = 0.4$ after $t = 32000\,\tau_A$. The further growth of $(5/2)$, $(5/3)$, $(3/2)$ and $(4/3)$ modes leads to a full stochastisation for $\Psi_N > 0.3$ after $t = 40000$. At that time the amplitudes of $n = 1$ harmonics do not change significantly, in agreement with the evolution of $E_{\mathrm{mag},1}$ respective $E_{\mathrm{mag,sum}}$. The $(2/1)$ island saturates with a width of about $W \approx 10\mathrm{cm}$, that is 20% of the minor radius. Also, the $(6/5)$ island gets visible, which is however not large enough for any island overlapping. Therefore the plasma core remains not being stochastic, which is characteristic for a "partial" thermal quench[78]. Stochastisation of the core would need the presence of islands of the $q = 1$ surface in the plasma. In the further course, all modes start shrinking and the stochastisation reduces. This may be caused by a flattening of the current profile due to the cooling of the plasma, as discussed in more detail in section 5.2.3.

The observed mode growth rates match well with the findings of mode coupling as discussed in section 2.5, as apparent from figure 21. For a quantiative comparison, the width growths rates γ_w are calculated numerically for the linear phase by:

$$\gamma_w(t_i) = \frac{\ln\left[w(t_{i+1}) - w(t_i)\right]}{t_{i+1} - t_i} \tag{5.2}$$

where t_i is the time at the i-th simulation step and $w(t_i)$ the island width in meters.

This yields growth rates of $\gamma_{w,n=1} = 4.6 \cdot 10^{-4}\,\tau_A^{-1}$ for all $n = 1$ islands, consistent of a coupling of the various $n = 1$ islands via the toroidicity related structure of the background field (see 2.5). $\gamma_{w,n=2} = 9.5{\cdot}10^{-4}\,\tau_A^{-1}$ for all $n = 2$ islands and $\gamma_{w,n=3} = 14.6{\cdot}10^{-4}\,\tau_A^{-1}$ for all $n = 3$ islands. They suggest a coupling of two $n = 1$ modes to destabilize the second harmonic, and coupling of a $n = 1$ and $n = 2$ mode to destabilize the third harmonics. For the fifth harmonic, likely to be a result of coupling of a $n = 2$ and $n = 3$ mode, has $\gamma_{w,n=5} = 22 \cdot 10^{-4}\,\tau_A^{-1}$ at $t = 25000\,\tau_A$, which shrinks to $\gamma_{w,n=5} = 10.2 \cdot 10^{-4}\,\tau_A^{-1}$ at $t = 29000\,\tau_A$. The reason be that the coupled modes are already in the non-linear phase at the time, therefore their growth rates change. Indeed, the sum of $\gamma_{w,n=2} + \gamma_{w,n=3}$ at $t = 2900\,\tau_A$ is still equivalent to $\gamma_{w,n=5}$.

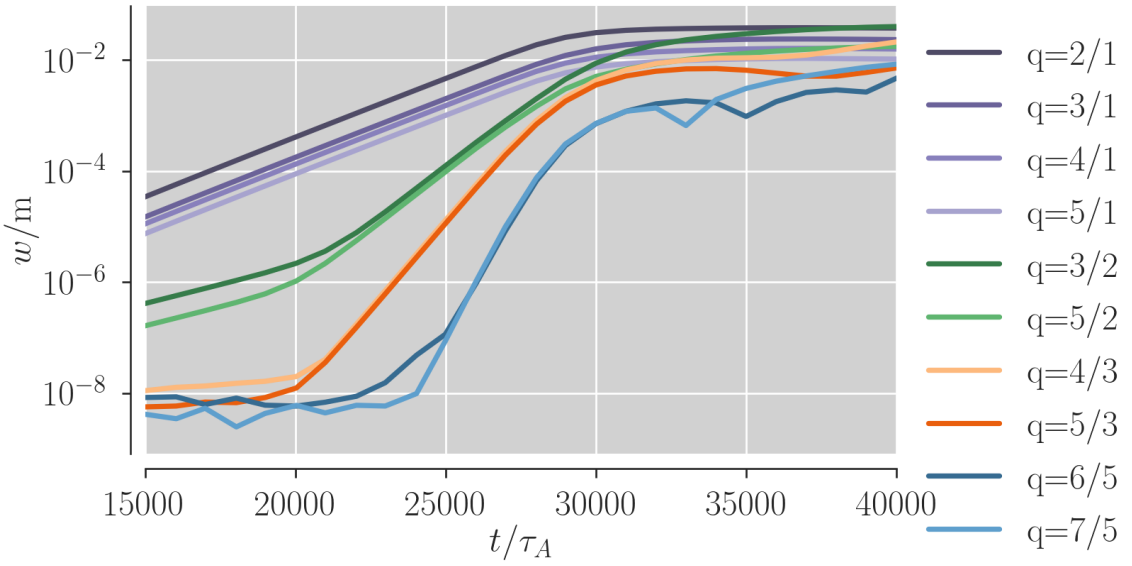

Figure 21: Widths of the islands shown in figure 20 versus time. The various m for a given n are coupled due to toroidicity effects. The higher n modes are driven by quadratic mode coupling of the lower mode numbers leading to higher growths rates than for the base mode.

5.2.2 Influence of the wall configuration on mode growth and stochastisation

An approximation for the influence of wall currents on the mode growth is given by the comparison of the distance between the wall and resonant surface and the poloidal wave length of the mode. The averaged minor radius of the $q = 2$-surface is about $r = 0.46\,\mathrm{m}$. This implies for a mode of $m = 2$ a wave length of $\lambda_{\mathrm{m=2}} \approx r\pi \approx 1.4\,\mathrm{m}$. The poloidally averaged distance between wall and resonant surface is $20\,\mathrm{cm}$ for the simulation with fixed boundary conditions, while it is around $80\,\mathrm{cm}$ for the simulations with ASDEX Upgrade like vacuum vessel. Since the distances are smaller than the wave length for each run, an influence of the wall on the mode growth can be expected by this approximation, which is confirmed by the observations described before. We assume, that the magnetic field generated by the wall currents decays like a vacuum field, so that $B_{\mathrm{wall}}(r) \propto (r_w - r)^{-3}$. Therefore the amplitude at the resonant surface $B_{\mathrm{wall}}(r_s)$ is already only about 2% in the run with ideal vessel compared to the run with fixed bound-

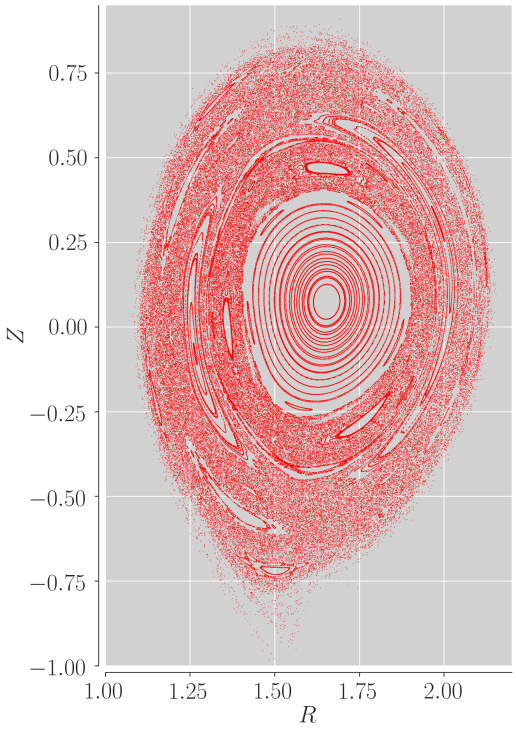

Figure 23: Poincareplot of the run with realistic vacuum vessel at timepoint $t = 54000\,\tau_A$.

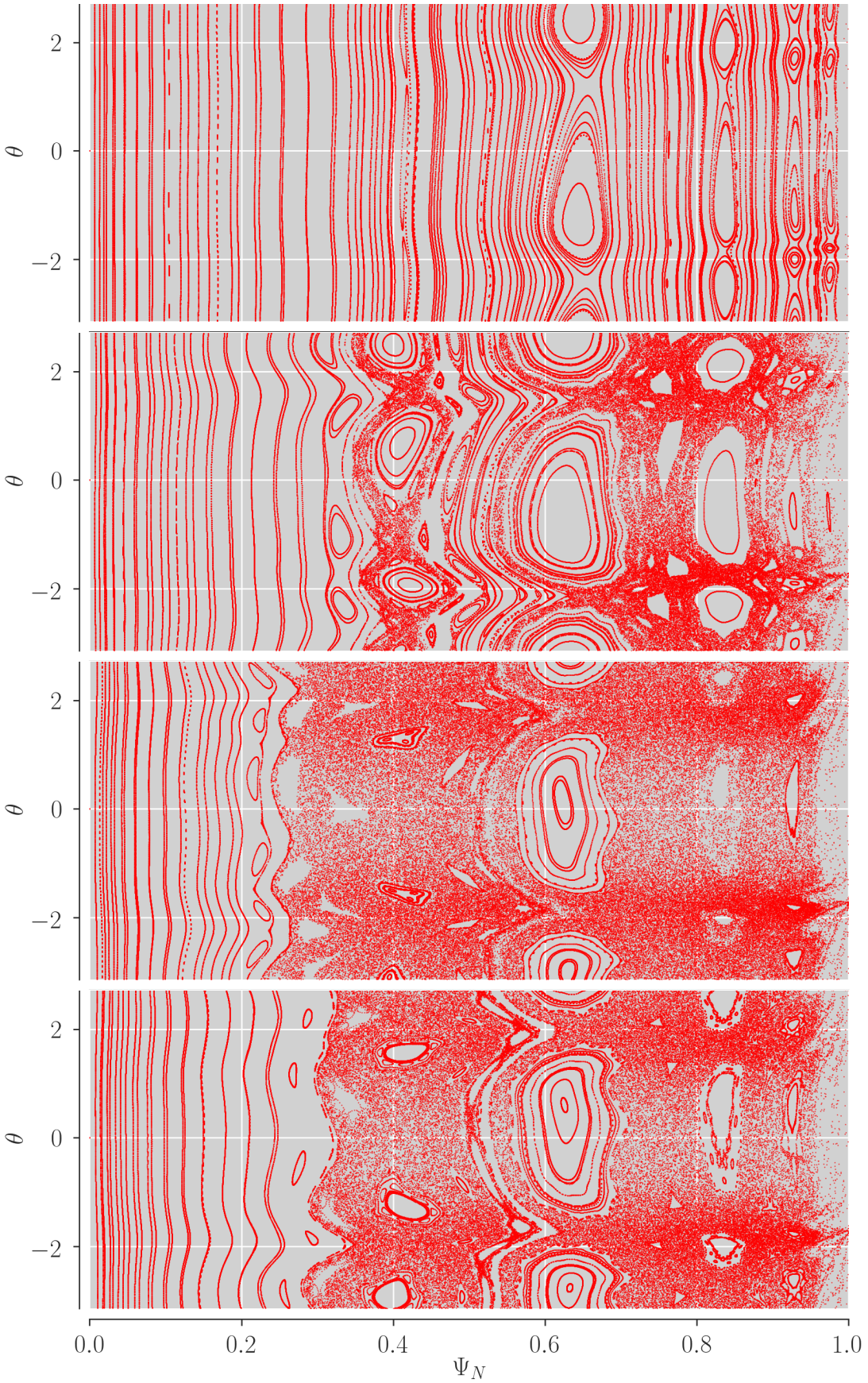

Figure 22: Poincareplots of the run with realistic vacuum vessel at timepoints $t = 28000\,\tau_A$, $t = 34000\,\tau_A$, $t = 42000\,\tau_A$ and $t = 54000\,\tau_A$.

ary. Hence varying the resistivity in addition only affects the plasma dynamics moderately. This is in full agreement with the observations described before.

A comparison of the island width evolution confirms that the influence is strongest at the plasma edge: the $(5/1)$, $(4/1)$ and $(3/1)$ islands saturate at widths of only 60% to 80% in the simulation with fixed boundary compared to the one with realistic vessel. In contrast, the wall configuration does not affect directly the maximum width of $(3/2)$ island. Since the non-linear phase of the $(2/1)$ mode sets in with a delay of about $5000\,\tau_A$ for the fixed boundary compared to the other runs, all other modes are affected and maximum islands widths are reached with a delay between $5000\,\tau_A$ to $10000\,\tau_A$.

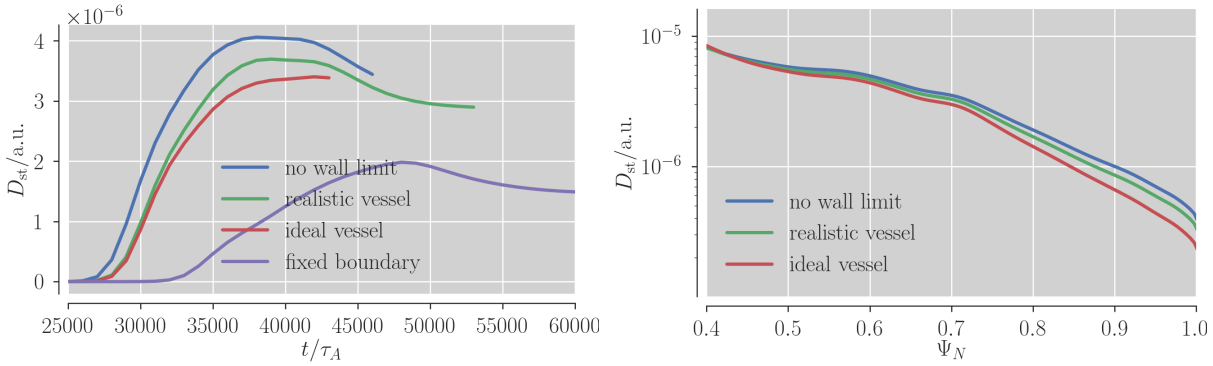

(a) (b)

Figure 24: (a) Time traces of the field line diffusion coefficient D_{st} at $q = 2$-surface. (b) Profile of D_{st} in the stochastic layer of the three runs with resistive wall. Each profile has been taken at the time point, where $E_{\mathrm{mag,sum}} = 3.2 \cdot 10^{-5}$. The run with fixed boundary is not shown as it does not reach that energy at any time.

The wall's direct and indirect influence both on growth rates and island widths has a significant impact on the stochastisation: to quantify the field stochastisation, The field line stochastisation coefficient, introduced in (2.39) is calculated with respect to Ψ_N for each simulation. The temporal evolution of $D_{\mathrm{st}}(\Psi_N = 0.65)$ confirms the strong dependency of the degree of stochastisation on wall geometry and resistivity (see figure 24): As mode growth is clearly reduced in the first simulation, maximal D_{st} is reduced by 50% compared to the cases with an ASDEX Upgrade like wall. In addition a dependency on the wall resistivity is now clearly visible, as $D_{\mathrm{st}}(0.65)$ is 20% smaller for the ideal wall as for the no-wall limit. The modification of D_{st} increases with reducing distance to the wall. Since the ideally conducting wall on the border of the computational domain suppresses all perturbation, $D_{\mathrm{st}}(\Psi_N \approx 1)$ is actually forced to zero in the first simulation.

5.2.3 Evolution of the temperature profile

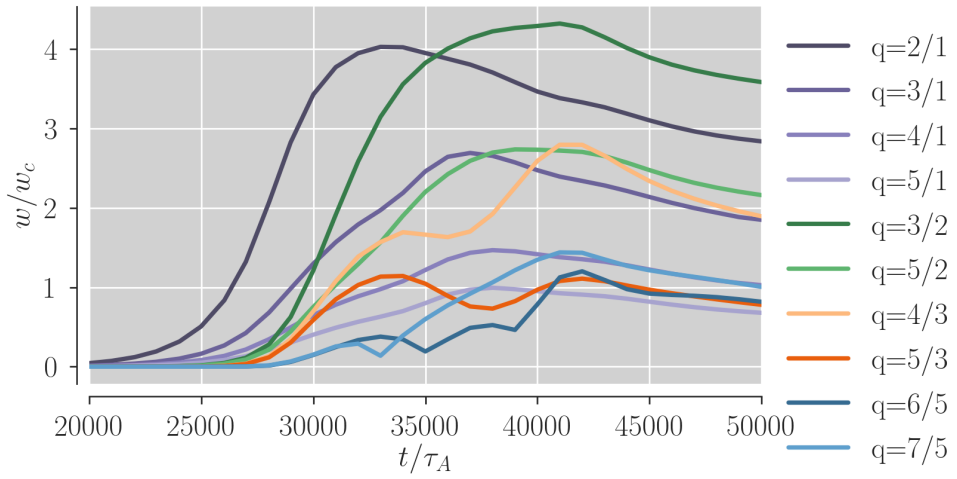

Figure 25: Widths of the islands shown 20 relative to their critical island width w_c for island flattening.

When islands reach the critical island width w_c, a flattening of the temperature profile occurs at first around the O-Point and extends up to the X-Point for $w \gtrsim 4w_c$ which leads to an axial-symmetric flattening, as discussed in Section 2.2.2. Further, if the heat diffusion anisotropy $\chi_\parallel/\chi_\perp$ is of order 10^8 or greater, also stochastisation has a significant effect onto the temperature distribution. In the following the simulation with realistic vacuum vessel is discussed.

The $(2/1)$ island reaches w_c at $t = 27000\,\tau_A$ (see figure 25). For $t = 30000\,\tau_A$, during the onset of the non-linear phase, it has already grown to a size of $3w_c$ and a significant effect on the temperature profile is already observable. This is in agreement with the intrinsic property of a mode in its non-linear phase to modify the equilibrium parameters. The stochasticity is not yet strongly developed (compare with figure 24). A maximum width of $4w_c$ is reached at $t = 34000\,\tau_A$. Secondly, the $(3/2)$ island starts rapidly growing after $t = 27000\,\tau_A$ and reaches $\approx 3.5w_c$ at $t = 34000\,\tau_A$. At that time point, also $(4/1)$ and $(5/2)$ are greater than $2w_c$.

The evolution of the temperature profile, averaged in poloidal and toroidal direction, is shown in figure 26. The flattening effect of the $(2/1)$ island becomes clearly visible in the beginning of the non-linear phase, around $\Psi_N = 0.65$. As no stochastisation occurs at that time point, the development of the temperature profile is only a result of the large island. At $t = 34000\,\tau_A$, the influence of the $(3/2)$ island, which now has reached a width of $3w_c$ becomes visible. Both flattened regions are still isolated from each other, as there exist non-destructed islands flux surfaces between both islands and a temperature difference of $\Delta T_e = 200\,\mathrm{eV}$ around $\Psi_N = 0.57$ remains. The increased radial heat transport at the plasma edge, in particular due to the $(4/1)$ and $(5/2)$ also leads to an increase of the temperature there. Since these islands stay only at sizes of $2w_c$, a temperature gradient in the averaged temperature profile remains.

In the further course, the enhancement of the radial heat transport due to stochasticity becomes relevant for $\Psi_N < 0.85$. Outside, the heat diffusion anisotropy is always smaller than 10^8. This implies that even for the distinct stochasticity of the plasma edge, a temperature

gradient remains. Inside, the flattening enhances and the temperature difference around $\Psi_N = 0.57$ decreases. In the following, the island sizes reduce due to the dropping neoclassical drive an the flattening of the current profile. The $(2/1)$ is only expanded to $\approx 3w_c$ at $t = 50000\,\tau_A$. Yet, the temperature between in $0.25 < \Psi_N < 0.8$ continues to drop. This is now in particular the result of the additional heat transport due to the stochasticity. As the temperature confinement is remarkably degraded, temperatures in the core $\Psi_N < 0.2$ also starts dropping.

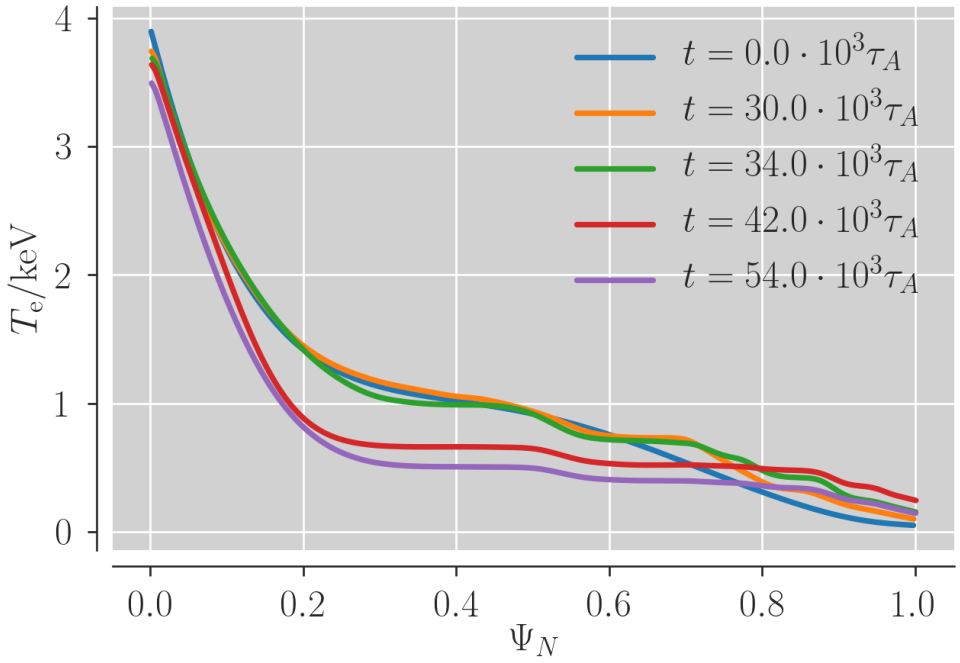

Figure 26: Temperature profile for the simulation with realistic vacuum vessel at different timesteps. Compare with figure 22.

However, a strong reduction of the temperature only occurs outside $\Psi_N = 0.3$, which is the approximate position of the inner margin of the $(3/2)$ island (see figure 20). Outside $\Psi_N = 0.3$, temperature is all below $T_e = 0.5\,\mathrm{keV}$. It is likely, that the temperature will further drop, if the simulation is continued. Due to that behaviour with relatively constant core temperature, this can be called a "partial" thermal quench.

A similar course has recently been investigated in DIII-D studies of locked mode disruptions[78]. The temperature, quenching just after the development of great $(2/1)$ and $(2/3)$ locked modes and reaching stochastisation in the outer plasma region, has been observed there experimentally and has been qualitatively reproduced by NIMROD. In contrary to this work, the island evolution has, however, not been investigated fully consistently in these simulation, which starts from ad-hoc initialized islands. In DIII-D and other machines, partial thermal quenches have often been observed as precursor events of "full" disruptions: Just after mode locking and within a time frame of about $200\,\mathrm{ms}$ usually three to five partial thermal quenches were observed, from which the plasma recovered. After that series of events, also the core temperature dropped in a full disruption. These findings motivate to investigate deeper into the

physics of partial thermal quenches to possibly improve disruption predictors.

5.2.4 Required mode amplitude to trigger a disruption

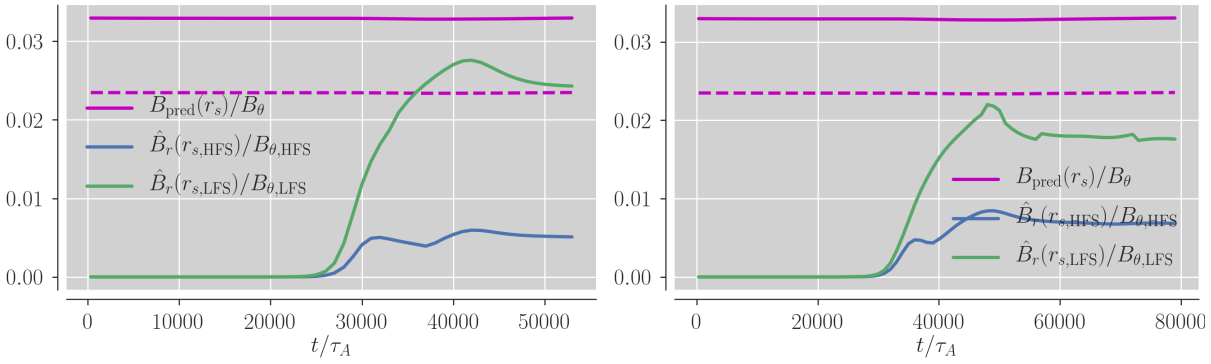

(a) (b)

Figure 27: Normalized perturbed field B_r at the rational surface $q = 2$ measured on midplane on high field side (HFS, blue) respective low field side (LFS, green). The amplitude for triggering thermal quench regarding de Vries is drawn in purple. The dashed line represents the lower limit of the confidence interval. (a) Simulation with realistic wall. The amplitude on LFS reaches up to 2.7% and matches the scaling law within the range of uncertainties, whereas it stays only at $< 1\%$ on HFS. (b) Simulation with fixed boundary conditions.

In a recent paper by de Vries et al.[85], a threshold for the measured locked mode signal reached at the disruption onset was formulated empirically. It was proposed, that this threshold only scales with a limited number of macroscopic parameters. The data of magnetic diagnostics on the low field side of JET from 250 shots, of ASDEX Upgrade (HFS) from 35 shots and of COMPASS (both LFS and HFS) from 19 shots were consulted to derive the following scaling law:

$$B_{\mathrm{pred}}(r_c) = (8.5 \pm 2.5) I_p^{1.07\pm0.11} a^{-1.1\pm0.11} q_{95}^{-1.2\pm0.12} l_{i3}^{1.2\pm0.12} \rho_c^{-2.8\pm0.3} \tag{5.3}$$

With the predicted amplitude at the coil in mT $B_{\mathrm{pred}}(r_c)$, plasma current I_p in MA, minor radius at the midplane a in m, internal inductance l_{i3}, and the normalized coil position $\rho_c = r_c/a$.

The internal inductance is defined by:

$$l_{i3} = \frac{2V\langle B_\theta^2\rangle}{\mu_0^2 I_p^2 R_0}, \quad V = \pi a^2 2\pi R_0 \tag{5.4}$$

where B_θ^2 was averaged using the definition $\langle ... \rangle = \int_0^a ... r dr 2/a^2$.

By the assumption, that the mode signal is mainly caused by the growth of the $(2/1)$ mode the scaling law was transformed to find also an expression for the perturbed field at the $q = 2$ surface, $B_{\mathrm{pred}}(r_s)$. To do so, the previously introduced scaling by r^{-m-1} was applied.

$B_{\mathrm{pred}}(r_q)$, normalized to the poloidal magnetic plasma edge, averaged over both sides of the midplane, $B_\theta(a)$, is then given by:

$$\frac{B_{\mathrm{pred}}(r_s)}{B_\theta(a)} = (9 \pm 1) \cdot 10^{-3} q_{95}^{0.85\pm0.18} l_{i3}^{0.35\pm0.15} \tag{5.5}$$

It was shown that this fraction is usually around 3%. It is to notice that both scaling laws do not distinguish between the side of the coils respective the resonant surface.

Equation (5.5) can be adapted to our runs, even though only a partial thermal quench has been observed. This is reasonable: as discussed above the reason for not observing a full stochastisation (hence a "full" thermal quench) is primarily caused by the absence of a $(1/1)$ mode. Since that mode would be close to the magnetic axis, it is far away from diagnostic coils in comparison to the $(2/1)$ mode. Therefore, the impact of a $(1/1)$ mode onto the coil signal would be limited. These assumptions match on measurements on DIII-D of partial and full thermal quenches, where no strong differences between partial and full TQs were observed in locked mode amplitudes[78],[80]. For a different simulation setup, which would allow for a drop of q_0 below unity, it would be very likely to trigger the $(1/1)$.

Since the plasma current only varies in the order of 1% through all simulations and also the q-profile does not evolve much, both $l_{i3} = 1.15$ and $q_{95} = 4.35$ keep constant within uncertainties. Both quantities lie within the ranges of the shots from ASDEX Upgrade considered in [85] and a threshold of $B_{\mathrm{pred}}(r_s)/B_\theta = (3.3 \pm 0.9)$ is predicted by (5.5).

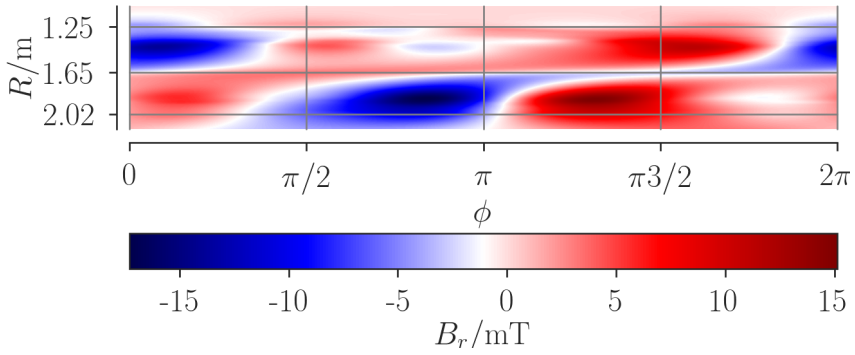

Figure 28: The perturbed field B_r measured at the midplane at $t = 42000\,\tau_A$ in the simulation with realistic vacuum vessel versus toroidal angle an major radius. The radial positions of the $q = 2$-surface and the magnetic axis are marked by grey lines.

The evolution of B_r strongly depends on the field side during all of our the simulations. During the linear phase, the structure of B_r is clearly dominated by an $n = 1$ periodicity. A maximum is reached at $\Psi_N = 0.27$ on the high field side respective $\Psi_N = 0.35$ on the low field side, which is smaller by one third on high field side. Also, B_r decays more towards the edge on high field side: hence it is usually three to four times smaller at $\Psi_N(r_s) = 0.65$ on high field side. At the end of the non-linear phase ($t = 25000\,\tau_A$ for the second simulation), $B(r_s, \mathrm{HFS}) = 1.8\,\mathrm{mT}$ toroidally averaged and $B(r_s, \mathrm{LFS}) = 5.0\,\mathrm{mT}$. During the non-linear phase, only $B(r_s, \mathrm{LFS}) = 5.0\,\mathrm{mT}$ continues do grow significantly. Outside the $q = 2$-resonant surface on the high field side, the B_r rapidly vanishes to values of $< 0.1\,\mathrm{mT}$. In contrary $B_r(\Psi_N = 0.95)$ has only reduced by half compared to the magnitude at the rational surface.

B_r on the midplane is shown in figure 28 at that time point during the non-linear phase, where the stochastisation reaches its maximal expansion.

The distinct behaviour of B_r on both sides motivates to treat them individually. For that purpose, the poloidal background field $B_\theta(a)$ is determined as $460\,\mathrm{mT}$ on high field side and $350\,\mathrm{mT}$ on low field side and remains constant over time. B_r is read out at the resonant surface on each side and at those toroidal position, where it becomes maximal to determine the amplitudes $\hat{B}_r(r_s)$. Since the plasma in the second to fourth simulation exhibits a slight toroidal rotation with a frequency of $\approx 40\,\mathrm{Hz}$ during the non-linear phase, these toroidal positions shift.

Within all simulation with ASDEX Upgrade like wall, the normalized B_r at the low field side reaches between 2.5% to 2.7% at around $t = 42000\,\tau_A$, i.e., when stochastisation becomes the most expanded. Afterwards, it shrinks to a value of 2.4% (see figure 27). This means that it clearly overcomes the lower limit of the confidence interval for the empirically predicted threshold. However, normalized B_r at the high field side remains at a value below 1%.

It is likely that the different amplitudes B_r are mainly an effect of toroidicity. These simulations suggest, that these toroidal effects already play a significant role for an aspect ratio of $R_0/a = 3.3$ and will therefore be also relevant for ITER, which will have a similiar aspect ratio. De Vries explicitly mentions, that the derived scaling law lacks of a distinction between HFS and LFS, which should be included in future work. Figure 3(a) in [85] shows a comparison between the measured locked mode amplitudes and the predictions as given by (5.3). The measured signals at COMPASS show derivations from the predicted amplitudes of up to 230%. Moreover, also the measurements of COMPASS systematically show, that $\hat{B}(r_s, \mathrm{HFS}) < \hat{B}(r_s, \mathrm{LFS})$[53],[85, table 1]. This motivates the need for further calculations.

5.2.5 Coil signals during the partial thermal quench

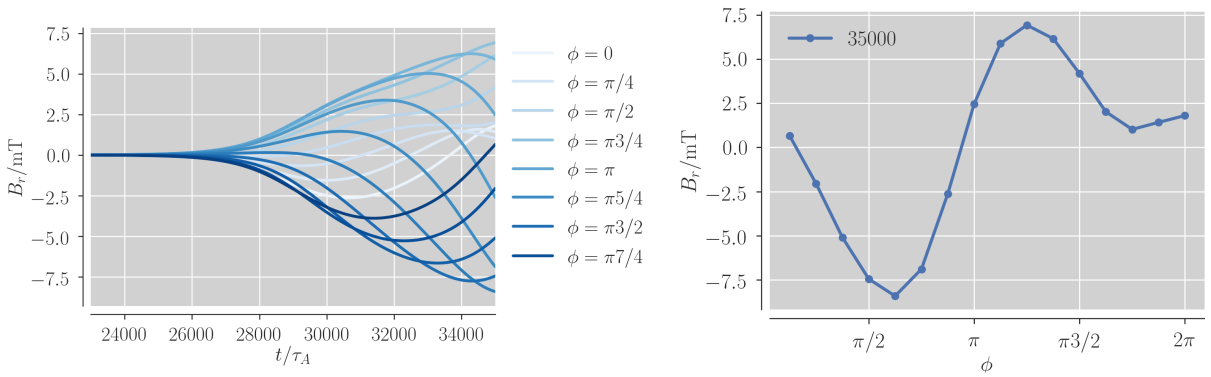

(a) (b)

Figure 29: (a) Time traces of the locked mode signals from Mirnov coils at low field side ($r_c = 57.2\,\mathrm{cm}$) in the run with realistic vacuum vessel. (b) The locked mode signal from the same coils at $t = 35000\,\tau_A$.

Virtual Mirnov coils similar to chapter 4 are placed on high and low field side at sixteen different toroidal positions. The signals were integrated to yield the radial magnetic field at the positions of the coils according to (2.45). The time traces (figure **??**(a)) show both the

growth of the mode and a slow rotation, which is mainly caused by an E-cross-B, velocity as further analysis have shown. The signals at $t = 35000\,\tau$ are given in figure **??**(b). At this time point, the $(2/1)$ mode is in the non-linear phase an modes of higher toroidal numbers are affecting the signal: although the $n = 1$ harmonic still dominates, significant deviations are observable for $\pi 3/2 < \phi < 2\pi$. These are in accordance to the radial field on the midplane given by figure 28. In contrast to chapter 4, this shows that coil signals can not always be directly mapped to a resonant surface and some post-processing, like a Fourier transformation, would be required to yield the amplitude of a mode.

The signal could be compared to (5.3). We leave this for further work, since our simulations already show very different values of the perturbed radial magnetic field between high and low field side rendering a more detailed comparison not useful at this time.

6. Simulation of mode locking

This section treats the effects of rotation and its interaction with the resistive vacuum vessel, namely the locking mechanism, acting onto a $(2/1)$ mode. The equilibrium and physics model used in Chapter 5 is used in this chapter as well, but E-cross-B background rotation and diamagnetic drift effects are taken into account. An additional toroidal rotation is not taken into account yet, which does not change the overall physics too strongly, such that this is sufficient for a qualitative analysis of mode locking.

Like discussed in 2.4 it is known, that the momentum transfer varies with the rotation frequency and it is supposed that it reaches a maximum if $\tau_w \omega \approx m$, where τ_w is the characteristic resistive time of the vessel, ω the frequency at the resonant surface of the considered mode, and m its mode number. In contrast, the transfer will vanish for both limits of the ideal and non conducting wall. Hence, for an initial constant frequency and by varying the wall resistivity, a value with maximum torque is expected, for which the decrease of plasma rotation should be strongest. In the last section of this chapter, that specific resistivity will be identified.

Besides, the occurrence of an island itself will reduce the rotation in a second way: the flattening of the temperature profile around an island, that has been discussed in the last section, leads to a modification of the pressure profile. The reduction of the pressure gradient entails a decrease of the neoclassical E-cross-B and diamagnetic velocities at the resonant surface. This effect is supposed to proceed on a much shorter timescale than the electromagnetic interaction with the wall, i.e. between entering the non-linear phase and island saturation. It will be only indirectly affected by the conducting wall, due to its influence on the mode growth rate.

6.1. Plasma and wall setup

Simulations mainly rely on the setup already described in Section 5.1. In addition, E-cross-B background rotation and diamagnetic terms of JOREK are now included. The ASDEX Upgrade like vacuum vessel is considered only. To analyse the influence of the wall resistivity on mode locking and to identify the value of maximal torque, a parameters scan over ten values of ρ_w respective twelve orders of magnitude is carried out. The characteristic time is approximated based on $\tau_w = \mu_0 / \rho_w b d/2$, with an average vessel radius of $b \approx 90\,\mathrm{cm}$ and the vessel thickness of $d = 15\,\mathrm{mm}$. This approximation allows to restrict the expected order of magnitude of the optimal resistivity. However, a more sophisticated prediction would require numerical calculations that take the exact vessel geometry into account, like implemented into the VALEN code[5].

$f = \rho_w / \rho_{w,0}$	τ_w / s
10^{-6}	$3.3 \cdot 10^{3}$
10^{-2}	$3.2 \cdot 10^{-1}$
$3 \cdot 10^{-2}$	$1.1 \cdot 10^{-1}$
10^{-1}	$3.3 \cdot 10^{-2}$
$3 \cdot 10^{-1}$	$1 \cdot 10^{-2}$
1	$3.3 \cdot 10^{-3}$
3	$1.1 \cdot 10^{-3}$
10	$3.3 \cdot 10^{-4}$
30	$1.1 \cdot 10^{-4}$
10^{6}	$3.3 \cdot 10^{-9}$

Table 1: ρ_w is given in units of realistic $\rho_{w,0} = 2.6 \cdot 10^{-6} \Omega\mathrm{m}$.

The considered resistivities and regarding resistive times are summarized in table 1. The runs with $f = 10^{-6}$ or $f = 10^{6}$ again represent the ideal wall or no-wall limits, where f denotes the scaling factor used for the resistivity in the scan.

Since the simulations focus on the investigation of the lock-

ing of the $(2/1)$ mode and its toroidicity induced sideband harmonics, only the first harmonic, $n = 1$, is considered.

6.2. Analysis of the plasma

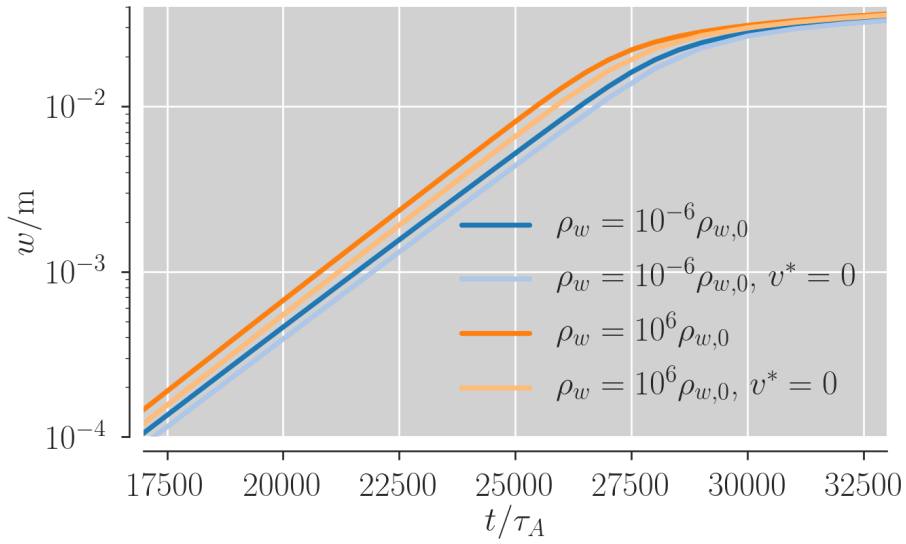

Figure 30: Evolution of the $(2/1)$ island widths in the run with ideal wall and no-wall limit. For a comparison, the respective runs without flows are also shown.

The destabilisation of the $(2/1)$ mode behaves similarly like for the cases without flows: The linear phase ends around $t = 25000\,\tau_A$, and different wall resistivities modify the growth rate such that the island width at $t = 25000\,\tau_A$ in the no-wall limit is only reached with a delay of $\Delta t = 1000\,\tau_A$ in the ideal wall limit.

The diamagnetic frequency at the $q = 2$ surface is $v_e^* = -200\,\mathrm{m/s}$ (see figure 32) initially. Assuming a poloidal circumference of the $q = 2$ surface of $C \approx 2\pi r = 2.9\,\mathrm{m}$ with minor radius $r = 0.46\,\mathrm{m}$, this yields a diamagnetic frequency of $69\,\mathrm{Hz}$. This relatively low frequency reflects the fact that the considered plasma has a low temperature and low pressure gradient around the $q = 2$ surface. The unchanged mode growth rates further confirm, that this low frequency has no significant stabilizing effect on the mode for this equilibrium.

In this regime, it is well justified to study the locking mechanism between plasma and vacuum vessel only: as discussed for DIII-D[52, fig. 10], the interaction with conducting structures inside the vessel is dominant for high frequencies of $10^4\,\mathrm{Hz}$. However, for frequencies of $10^2\,\mathrm{Hz}$ or lower - which is the case here - the vacuum vessel dominates the locking.

6.2.1 Mode locking

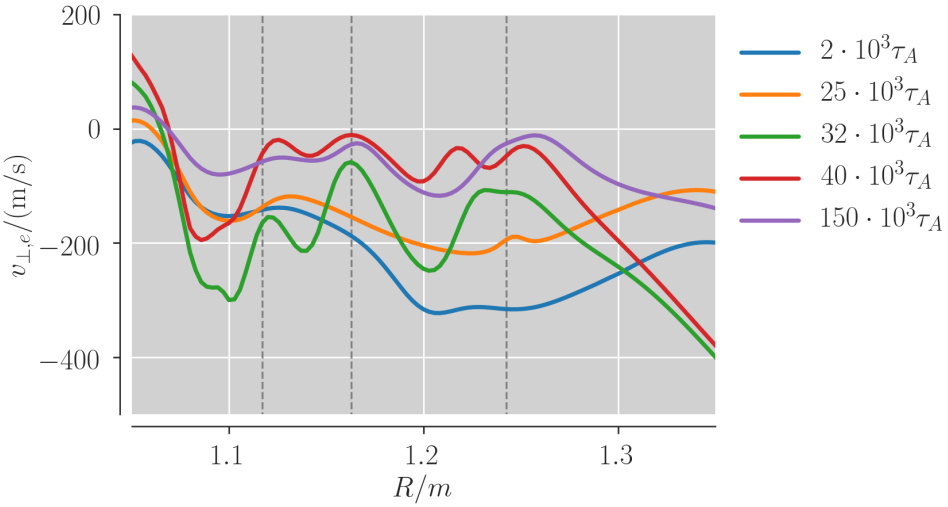

Figure 31: Poloidal velocity profile for $\rho_w = \rho_0$ at the midplane on high field site at some time points. The radial positions of the $(4/1)$, $(3/1)$ and $(2/1)$ islands are marked with vertical lines from left to right.

The following section describes the simulation with $f = 1$ in more detail, wherby the locking behaves qualitatively the same for the other resistivities: the temporal evolution of the velocity profile (see figure 31.) shows first influences through the occurrence of the $(2/1)$ mode for $t = 25000\,\tau_A$: The small perturbation of the velocity of 5% only around the resonant surface ($R = 1.25\,\mathrm{m}$ at HFS) can easily be identified as an effect of mode locking. After mode saturation at $t = 32000\,\tau_A$, locking sets in at the side band harmonics $(3/1)$ and $(4/1)$, too. The poloidal velocity reaches values close to zero at the resonant surfaces and due to frictional forces acting between plasma at the resonant surface and the surroundings, the overall velocity between $\Psi_N = 0.6$ and $\Psi_N = 0.95$ shrinks.

The first phase of velocity reduction is clearly dominated by the reduction of the diamagnetic drift as introduced before (see figure 32). After mode saturation E-cross-B goes to zero and even points in the opposite direction for a time of $< 1000\,\tau_A$. Then, it turns back in the original direction and increases. These effects could be a results of Maxwell stress, like explained in [44]. After that, locking mechanism sets in and the velocities decrease over a timescale of $\Delta t = 100000\,\tau_A$.

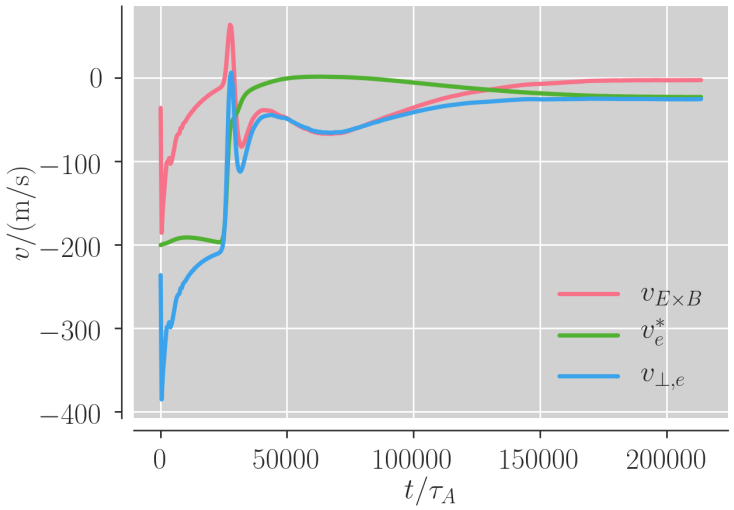

Figure 32: Time traces of the contributions to the poloidal velocity at the q=2-surface on the high field side for $\rho_w = \rho_0$. $v_{\perp,e} = v_e^* + v_{E\times B}$ holds.

6.2.2 Influence of different wall resistivities

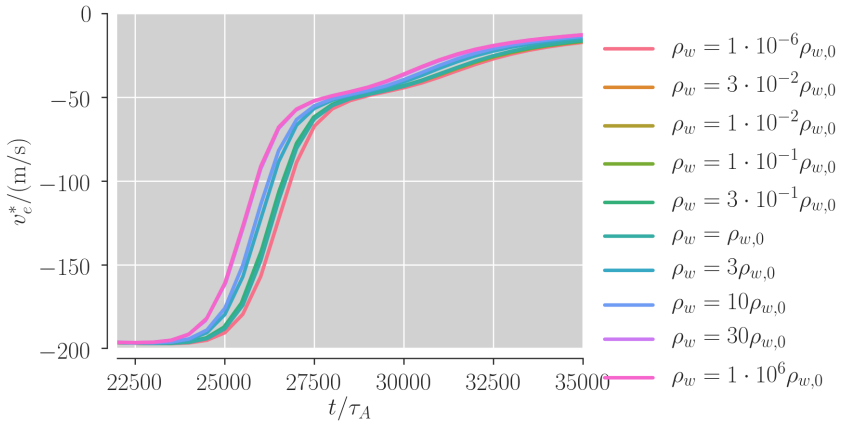

Figure 33: Poloidal velocity after entering the non-linear phase of the growth of the $(2/1)$ mode. The effect of different wall resistivities is indirect by modifying the growth rate and thus time point of saturation.

Starting from the initial diamagnetic velocity $v_e^* = -200\,\mathrm{m/s}$ at the resonant surface, the deceleration sets in at $t \approx 23000\,\tau_A$ in the run with the no-wall limit and the velocity reduces to $-150\,\mathrm{m/s}$ at $t \approx 25000\,\tau_A$ (see fig 33). Both time points are delayed by around $\Delta t = 1000\,\tau_A$ for the ideal wall limit. For increasing resistivity this delay reduces monotonously. This behaviour matches quantitatively with the observations about mode growth: The delay of $\Delta t = 1000\,\tau_A$ is reflected also in the different onset of the non-linear phase. Independently of the growth rates, the $(2/1)$ island saturates in each run at a width of $> 4w_c$, implying a distinct flattening of the kinetic profile. Hence, the pressure gradient decreases to $< 5\%$ of

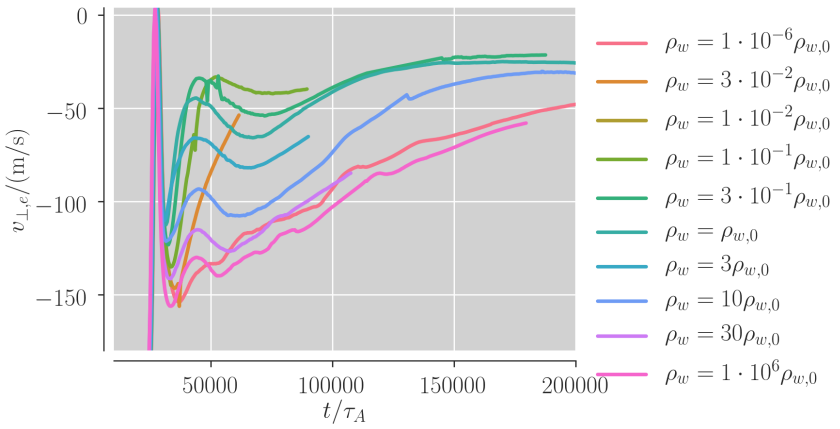

Figure 34: Development of the overall poloidal velocity in the later course. The locking sets in and is strongest at a realistic resistivity of $\sim 10^{-1}\rho_{w,0}$.

the initial value for each run after $t > 50000\,\tau_A$, which makes the diamagnetic drift vanishing.

The no-wall and ideal-wall limits both show a similar behaviour in the latter course, where the E-cross-B drift dominates: starting from $v_{\perp,e} \approx -150\,\mathrm{m/s}$, the velocity reduces to $\approx -50\,\mathrm{m/s}$ after $t = 20000\,\tau_A$ (see figure 34). Since momentum transfer onto the wall is vanishing for these limits, it is assumed that only changes in the pressure gradient and friction forces within the plasma lead to the reduction. All runs with resistivites between these two limits show a clear braking due to the interaction with the conducting vessel.

The strongest locking can be identified at $\rho_w \approx 1 \cdot 10^{-1}\rho_0$: In that case, $v_{\perp,e} = -40\,\mathrm{m/s}$ already at $t = 50000\,\tau_A$. At $t = 35000\,\tau_A$, when the E-cross-B drift reaches a maximum, the entire velocity is about $140\,\mathrm{m/s}$ in this run, which corresponds to a poloidal rotation with a frequency of $\omega = 50\mathrm{Hz}$ at the resonant surface. This leads to $\tau_W\omega = 1.6$. This value is approximately equal to m as predicted, and torque acts with an amplitude close to the maximum regarding (2.38). In comparison, the velocity decreases only to $v_{\perp,e} = -50\,\mathrm{m/s}$ for a run with $\rho_w = \rho_0$. In this case, where $\tau_W\omega$ is one order of magnitude smaller, the deceleration has an amplitude of only 15% of the maximum value.

7. Summary and Outlook

In this thesis, simulations of several aspects crucial for the understanding of the disruption onset were carried out for the first time with the non-linear magnetohydrodynamics code JOREK-STARWALL in realistic tokamak X-Point geometry.

The subject of the first part of this thesis was to generate virtual diagnostic coil signals for the detection of tearing modes. For that purpose an ASDEX Upgrade like L-mode equilibrium with a core electron temperature of $4\,\mathrm{keV}$ was considered and by the addition of an artificial cooling source on the $q = 2$ surface, a $(2/1)$ mode with a small amplitude was triggered. Virtual Mirnov and Saddle coils for the measurement of the radial and poloidal components of the perturbed field were implemented.

Toroidal periodicity of the coil signals corresponds well to the periodicity of the $(2/1)$. This means by using a sufficient number of Mirnov coils the mode and its phase shift can be identified easily. It was also checked how well the radial decay of the amplitude can be predicted. At positions where B_r respective B_θ reaches their maxima, the decay matches well with predictions for simple geometries.

Secondly, the evolution of a $(2/1)$ neoclassical tearing mode into a partial thermal quench was investigated in detail. A similar ASDEX Upgrade like equilibrium was considered again and modified such that it is consistently unstable against the $(2/1)$ mode. The evolution of the plasma leads to a "partial" thermal quench, i.e. a stochastisation and cooling of the outer plasma, which left the plasma core nearly unaffected. The detailed analysis of important physicals mechanisms involved confirmed that the simulation met with theoretical and experimental predictions or observations: After the initial occurrence of the $(2/1)$ mode, modes of higher poloidal respective toroidal number were coupled due to toroidicity effects respectively quadratic coupling. It was shown, that the onset of stochastisation matches the Chirikov criterion, i.e. were observed after island overlapping. The temperature profile became significantly flattened in the island region with a critical island size regarding Fitzpatrick. That flattening finally lead to the partial thermal quench. As experiments have shown, partial thermal quenches are often occur during the precursor phase prior to a full thermal quench. This enhances the relevance of this simulation for disruption modelling.

As third part of this thesis, the equilibrium was modified, so that it exhibits a slow poloidal rotation below $100\,\mathrm{Hz}$. The reason for such a weak rotation is given by a relatively flat pressure gradient around the $q = 2$ surface. These slow rotation frequencies usually occur in the last sequence of locking, where the interaction with the vacuum vessel becomes most relevant. The vessel was considered in these simulations and a parameter scan of its resistivity respective its characteristic wall time was performed. The dependency of locking on the resistivity was clearly shown and the maximum decrease of rotation were observed at a value in agreement with predictions. However, plasma rotation and locking need to be investigated in more detail in further simulations. Rotation frequencies of up to $10\,\mathrm{kHz}$ are often observed in experiments. They can be caused by momentum transfer from injected neutral beams but also from steep pressure gradients, which are a main property of H-Mode plasmas. For such high frequencies, mode growth is expected to be significantly decreased and the locking phase can proceed over some hundreds of milliseconds.

The fact, that these simulations reproduce disruption processes well in a qualitative manner, qualify them for further studies: using a more complex model implemented in JOREK, disrup-

tion mitigation has already been shown.[56] These simulations started from "healthy" plasmas exhibiting no instabilities. It is straightforward to apply this model to the equilibrium used here. The effectiveness of mitigation depending on the time point from when it was started during development of the (partial) TQ can than be investigated.

An extension of JOREK is currently under development, allowing to simulate the interaction of run away electrons with the plasma.[3] Starting from an initial distribution of REs, its evolution and back reaction onto the plasma can be studied. The effect of RE beams during the (partial) thermal quench can be investigated within this setup. It is of interest for instance how they further destabilize the tearing modes.

A full TQ simulation can be approached with a fully consistend current profile evolution. This will allow for the destabilization of a $(1/1)$ mode that leads to a full stochastisation. In the long term, a simulation of the full sequence of a thermal quench towards a VDE would be possible. Simulations of VDEs within JOREK were recently carried out[1].

Appendices

References

[1] F.J. Artola et al. "Non-linear magnetohydrodynamic simulations of edge localised mode triggering via vertical position oscillations in ITER". In: *Nuclear Fusion* 58.9 (July 2018), p. 096018. DOI: 10.1088/1741-4326/aace0e. URL: https://doi.org/10.1088%2F1741-4326%2Faace0e.

[2] R Aymar, P Barabaschi, and Y Shimomura. "The ITER design". In: *Plasma Physics and Controlled Fusion* 44.5 (2002), p. 519. URL: http://stacks.iop.org/0741-3335/44/i=5/a=304.

[3] Hoelzl M. et al. Bandaru V. "Runaway electron fluid model with non-linear coupling to MHD modes in the JOREK code". In: *Physical Review E* (2019).

[4] I. Bernstein. "An energy principle for hydromagnetic stability problems". In: *Proceedings of the Royal Society of London A: Mathematical, Physical and Engineering Sciences* 244.1236 (1958), pp. 17–40. ISSN: 0080-4630. DOI: 10.1098/rspa.1958.0023. eprint: http://rspa.royalsocietypublishing.org/content/244/1236/17.full.pdf. URL: http://rspa.royalsocietypublishing.org/content/244/1236/17.

[5] James Bialek et al. "Modeling of active control of external magnetohydrodynamic instabilities". In: *Physics of Plasmas* 8.5 (2001), pp. 2170–2180. DOI: 10.1063/1.1362532. eprint: https://doi.org/10.1063/1.1362532. URL: https://doi.org/10.1063/1.1362532.

[6] A. Bondeson. "Simulations of tokamak disruptions including self-consistent temperature evolution". In: *Nuclear Fusion* 26.7 (1986), p. 929. URL: http://stacks.iop.org/0029-5515/26/i=7/a=009.

[7] Allen H. Boozer. "Physics of magnetically confined plasmas". In: *Rev. Mod. Phys.* 76 (4 Jan. 2005), pp. 1071–1141. DOI: 10.1103/RevModPhys.76.1071. URL: https://link.aps.org/doi/10.1103/RevModPhys.76.1071.

[8] S.I. Braginski. "Transport Processes in a Plasma". In: *Review of Plasma Physics* 1 (1965), p. 205.

[9] D.P Brennan et al. "A categorization of tearing mode onset in tokamaks via nonlinear simulation". In: *Nuclear Fusion* 45.9 (Sept. 2005), pp. 1178–1190. DOI: 10.1088/0029-5515/45/9/018. URL: https://doi.org/10.1088%2F0029-5515%2F45%2F9%2F018.

[10] C Z Cheng, H P Furth, and A H Boozer. "MHD stable regime of the Tokamak". In: *Plasma Physics and Controlled Fusion* 29.3 (1987), p. 351. URL: http://stacks.iop.org/0741-3335/29/i=3/a=006.

[11] Boris V Chirikov. "A universal instability of many-dimensional oscillator systems". In: *Physics Reports* 52.5 (1979), pp. 263–379. ISSN: 0370-1573. DOI: https://doi.org/10.1016/0370-1573(79)90023-1. URL: http://www.sciencedirect.com/science/article/pii/0370157379900231.

[12] Robert S. Cohen, Lyman Spitzer, and Paul McR. Routly. "The Electrical Conductivity of an Ionized Gas". In: *Phys. Rev.* 80 (2 Oct. 1950), pp. 230–238. DOI: 10.1103/PhysRev.80.230. URL: https://link.aps.org/doi/10.1103/PhysRev.80.230.

[13] N. Commaux et al. "Demonstration of rapid shutdown using large shattered deuterium pellet injection in DIII-D". In: *Nuclear Fusion* 50.11 (2010), p. 112001. URL: http://stacks.iop.org/0029-5515/50/i=11/a=112001.

[14] Olivier Czarny and Guido Huysmans. "Bézier surfaces and finite elements for MHD simulations". In: *Journal of Computational Physics* 227.16 (2008), pp. 7423–7445. ISSN: 0021-9991. DOI: https://doi.org/10.1016/j.jcp.2008.04.001. URL: http://www.sciencedirect.com/science/article/pii/S0021999108002118.

[15] A. Lessig E Franck M Hoelzl. "Energy conservation and numerical stabilty for the reduced MHD models for the non-linear JOREK code". In: *ESAIM: Mathematica Modeling an Numerical Analysis* 49.5 (2015), p. 1331 1365. URL: https://www.esaim-m2an.org/articles/m2an/abs/2015/05/m2an141088/m2an141088.html.

[16] A. Fil et al. "Three-dimensional non-linear magnetohydrodynamic modeling of massive gas injection triggered disruptions in JET". In: *Physics of Plasmas* 22.6 (2015), p. 062509. DOI: 10.1063/1.4922846. eprint: https://doi.org/10.1063/1.4922846. URL: https://doi.org/10.1063/1.4922846.

[17] R. Fitzpatrick. "Interaction of tearing modes with external structures in cylindrical geometry (plasma)". In: *Nuclear Fusion* 33.7 (1993), p. 1049. URL: http://stacks.iop.org/0029-5515/33/i=7/a=I08.

[18] Richard Fitzpatrick. *Computatinal Physics*. CreateSpace Independent Publishing Platform, 2015, pp. 151–153. ISBN: 978-1506189802.

[19] Richard Fitzpatrick. "Helical temperature perturbations associated with tearing modes in tokamak plasmas". In: *Physics of Plasmas* 2.3 (1995), pp. 825–838. DOI: 10.1063/1.871434. eprint: https://doi.org/10.1063/1.871434. URL: https://doi.org/10.1063/1.871434.

[20] Richard Fitzpatrick. *Plasma Physics. An Introduction*. CRC Press, 2014. ISBN: 978-1-466-59426-5.

[21] R Fitzpatrick et al. "Stability of coupled tearing modes in tokamaks". In: *Nuclear Fusion* 33.10 (Oct. 1993), pp. 1533–1576. DOI: 10.1088/0029-5515/33/10/i11. URL: https://doi.org/10.1088%2F0029-5515%2F33%2F10%2Fi11.

[22] Jeffrey P. Freidberg. "MHD stability – general considerations". In: *Ideal MHD*. Cambridge University Press, 2014, pp. 327–380. DOI: 10.1017/CBO9780511795046.009.

[23] H. P. Furth, P. H. Rutherford, and H. Selberg. "Tearing mode in the cylindrical tokamak". In: *The Physics of Fluids* 16.7 (1973), pp. 1054–1063. DOI: 10.1063/1.1694467. eprint: https://aip.scitation.org/doi/pdf/10.1063/1.1694467. URL: https://aip.scitation.org/doi/abs/10.1063/1.1694467.

[24] Harold P. Furth, John Killeen, and Marshall N. Rosenbluth. "Finite Resistivity Instabilities of a Sheet Pinch". In: *The Physics of Fluids* 6.4 (1963), pp. 459–484. DOI: 10.1063/1.1706761. eprint: https://aip.scitation.org/doi/pdf/10.1063/1.1706761. URL: https://aip.scitation.org/doi/abs/10.1063/1.1706761.

[25] R.D. Gill et al. "Direct observations of runaway electrons during disruptions in the JET tokamak". In: *Nuclear Fusion* 40.2 (2000), p. 163. URL: http://stacks.iop.org/0029-5515/40/i=2/a=302.

[26] A. H. Glasser, J. M. Greene, and J. L. Johnson. "Resistive instabilities in general toroidal plasma configurations". In: *The Physics of Fluids* 18.7 (1975), pp. 875–888. DOI: 10.1063/1.861224. eprint: https://aip.scitation.org/doi/pdf/10.1063/1.861224. URL: https://aip.scitation.org/doi/abs/10.1063/1.861224.

[27] E. P. Gorbunov and K. A. Razumova. "The effect of a strong magnetic field on the magnetohydrodynamic stability of plasma and the containment of charged particles in the Tokamak". In: *Soviet Atomic Energy* 15.5 (Nov. 1963), pp. 105–1112. DOI: 10.1007/BF01115931. URL: https://doi.org/10.1007/BF01115931.

[28] M. Greenwald et al. "A new look at density limits in tokamaks". In: *Nuclear Fusion* 28.12 (1988), p. 2199. URL: http://stacks.iop.org/0029-5515/28/i=12/a=009.

[29] Martin Greenwald. "Density limits in toroidal plasmas". In: *Plasma Physics and Controlled Fusion* 44.8 (2002), R27. URL: http://stacks.iop.org/0741-3335/44/i=8/a=201.

[30] RAY C. GRIMM, JOHN M. GREENE, and JOHN L. JOHNSON. "Computation of the Magnetohydrodynamic Spectrum in Axisymmetric Toroidal Confinement Systems". In: *Controlled Fusion*. Ed. by JOHN KILLEEN. Vol. 16. Methods in Computational Physics: Advances in Research and Applications. Elsevier, 1976, pp. 253–280. DOI: https://doi.org/10.1016/B978-0-12-460816-0.50012-9. URL: http://www.sciencedirect.com/science/article/pii/B9780124608160500129.

[31] TFR Group. "Low-Q MHD activity studies on TFR". In: *Nuclear Fusion* 24.6 (1984), p. 784. URL: http://stacks.iop.org/0029-5515/24/i=6/a=011.

[32] O Gruber et al. "Vertical displacement events and halo currents". In: *Plasma Physics and Controlled Fusion* 35.SB (1993), B191. URL: http://stacks.iop.org/0741-3335/35/i=SB/a=015.

[33] B. Sombach. et. al. H. Kotzlowski. "Concept, Calculation and Design of the Insulation Gap in the Vacuum Vessel of ASDEX Upgrade". In: (1986). URL: http://www.aug.ipp.mpg.de/documentation/pub/VacuumVessel/VacuumVessel/1986-4.pdf.

[34] P. Helander et al. "Resistive stability of a plasma with runaway electrons". In: *Physics of Plasmas* 14.12 (2007), p. 122102. DOI: 10.1063/1.2817016. eprint: https://doi.org/10.1063/1.2817016. URL: https://doi.org/10.1063/1.2817016.

[35] T.C. Hender et al. "Chapter 3: MHD stability, operational limits and disruptions". In: *Nuclear Fusion* 47.6 (2007), S128. URL: http://stacks.iop.org/0029-5515/47/i=6/a=S03.

[36] P. Hénon, P. Ramet, and J. Roman. "PaStiX: a high-performance parallel direct solver for sparse symmetric positive definite systems". In: *Parallel Computing* 28.2 (2002), pp. 301–321. ISSN: 0167-8191. DOI: https://doi.org/10.1016/S0167-8191(01)00141-7. URL: http://www.sciencedirect.com/science/article/pii/S0167819101001417.

[37] Charles Hirsch. "Chapter 9 - Time Integration Methods for Space-discretized Equations". In: *Numerical Computation of Internal and External Flows (Second Edition)*. Ed. by Charles Hirsch. Second Edition. Oxford: Butterworth-Heinemann, 2007, pp. 413–489. ISBN: 978-0-7506-6594-0. DOI: https://doi.org/10.1016/B978-075066594-0/50052-7. URL: http://www.sciencedirect.com/science/article/pii/B9780750665940500527.

[38] M Hoelzl et al. "Coupling JOREK and STARWALL Codes for Non-linear Resistive-wall Simulations". In: *Journal of Physics: Conference Series* 401 (Dec. 2012), p. 012010. DOI: 10.1088/1742-6596/401/1/012010. URL: https://doi.org/10.1088%2F1742-6596%2F401%2F1%2F012010.

[39] E.M. Hollmann et al. "Measurements of injected impurity assimilation during massive gas injection experiments in DIII-D". In: *Nuclear Fusion* 48.11 (2008), p. 115007. URL: http://stacks.iop.org/0029-5515/48/i=11/a=115007.

[40] Matthias Hölzl. "Diffuse Heat Transport across Magnetic Islands and Stochastik Layers in Tokamaks". PhD thesis. Technische Universität München, 2007.

[41] K.I. Hopcraft, A. Sykes, and M.F. Turner. "Comparison of tokamak disruption simulations". In: *Nuclear Fusion* 28.7 (1988), p. 1265. URL: http://stacks.iop.org/0029-5515/28/i=7/a=009.

[42] K. Hoshino et al. "Avoidance of q=3 disruption by electron cyclotron heating in the JFT-2M tokamak". In: *Phys. Rev. Lett.* 69 (15 Oct. 1992), pp. 2208–2211. DOI: 10.1103/PhysRevLett.69.2208. URL: https://link.aps.org/doi/10.1103/PhysRevLett.69.2208.

[43] Q. Hu. "Fast and pervasive heat transport induced by multiple locked modes in DIII-D". 2018. URL: https://pinboard.ipp.mpg.de/bin/pinboard/viewdocument/qiy_00024/1?t=1541802771.

[44] G.T.A. Huysmans and O. Czarny. "MHD stability in X-point geometry: simulation of ELMs". In: *Nuclear Fusion* 47.7 (2007), p. 659. URL: http://stacks.iop.org/0029-5515/47/i=7/a=016.

[45] S.C. Jardin. "A triangular finite element with first-derivative continuity applied to fusion MHD applications". In: *Journal of Computational Physics* 200.1 (2004), pp. 133–152. ISSN: 0021-9991. DOI: https://doi.org/10.1016/j.jcp.2004.04.004. URL: http://www.sciencedirect.com/science/article/pii/S0021999104001366.

[46] et.al. Krebs I. Artola F.J. "Axisymmetric simulations of vertical displacement events: A benchmark of nonlinear MHD codes". In: *Nuclear Fusion* (2018).

[47] I. Krebs et al. "Nonlinear excitation of low-n harmonics in reduced magnetohydrodynamic simulations of edge-localized modes". In: *Physics of Plasmas* 20.8 (2013), p. 082506. DOI: 10.1063/1.4817953. eprint: https://doi.org/10.1063/1.4817953. URL: https://doi.org/10.1063/1.4817953.

[48] Martin David Kruskal, Martin Schwarzschild, and Subrahmanyan Chandrasekhar. "Some instabilities of a completely ionized plasma". In: *Proceedings of the Royal Society of London. Series A. Mathematical and Physical Sciences* 223.1154 (1954), pp. 348–360. DOI: 10.1098/rspa.1954.0120. URL: https://royalsocietypublishing.org/doi/abs/10.1098/rspa.1954.0120.

[49] T. Kudyakov et al. "Spatially and temporally resolved measurements of runaway electrons in the TEXTOR tokamak". In: *Nuclear Fusion* 48.12 (2008), p. 122002. URL: http://stacks.iop.org/0029-5515/48/i=12/a=122002.

[50] M. Lehnen et al. "Disruption mitigation by massive gas injection in JET". In: *Nuclear Fusion* 51.12 (2011), p. 123010. URL: http://stacks.iop.org/0029-5515/51/i=12/a=123010.

[51] B. Lipschultz et al. "Marfe: an edge plasma phenomenon". In: *Nuclear Fusion* 24.8 (1984), p. 977. URL: http://stacks.iop.org/0029-5515/24/i=8/a=002.

[52] N C Logan, E J Strait, and H Reimerdes. "Measurement of the electromagnetic torque in rotating DIII-D plasmas". In: *Plasma Physics and Controlled Fusion* 52.4 (2010), p. 045013. URL: http://stacks.iop.org/0741-3335/52/i=4/a=045013.

[53] *Critical RMP Field and Magnetic Island Amplitude Prior to Disruption on the COMPASS Tokamak*. Nov. 2016. URL: https://www.researchgate.net/publication/312607831_Critical_RMP_field_and_magnetic_island_amplitude_prior_to_disruption_on_the_COMPASS_tokamak.

[54] et al. Meshcheriakov D. Hoelzl M. "Numerical study of tearing mode seeding in tokamak X-point plasma". In: *Physics of Plasmas (submitted)* (2019).

[55] M. Nagami et al. "High-density, low-q discharges with D-shaped and circular cross-sections in Doublet III". In: *Nuclear Fusion* 22.3 (1982), p. 409. URL: http://stacks.iop.org/0029-5515/22/i=3/a=009.

[56] E Nardon et al. "Progress in understanding disruptions triggered by massive gas injection via 3D non-linear MHD modelling with JOREK". In: *Plasma Physics and Controlled Fusion* 59.1 (2017), p. 014006. URL: http://stacks.iop.org/0741-3335/59/i=1/a=014006.

[57] M.F.F. Nave and J.A. Wesson. "Mode locking in tokamaks". In: *Nuclear Fusion* 30.12 (1990), p. 2575. URL: http://stacks.iop.org/0029-5515/30/i=12/a=011.

[58] "Nonlinear magnetohydrodynamics simulation using high-order finite elements". In: *Journal of Computational Physics* 195.1 (2004), pp. 355–386. ISSN: 0021-9991. DOI: https://doi.org/10.1016/j.jcp.2003.10.004. URL: http://www.sciencedirect.com/science/article/pii/S0021999103005369.

[59] E Strumberger P Merkel. "Linear MHD stability studies with the STARWALL code". In: (2015). URL: https://arxiv.org/abs/1508.04911.

[60] W. Schneider P.J McCarthy P. Martin. "The CLISTE interpretive equilibrium code". In: (1999). URL: http://inis.iaea.org/search/search.aspx?orig_q=RN:31057068;.

[61] S. Pamela. "Simulation Magneto-Hydro-Dynamiques des Edge-Localised-Modes dans un tokamak". PhD thesis. Universite de Provence, 2010. URL: https://inis.iaea.org/collection/NCLCollectionStore/_Public/43/127/43127242.pdf.

[62] W. Park et al. "Plasma simulation studies using multilevel physics models". In: *Physics of Plasmas* 6.5 (1999), pp. 1796–1803. DOI: 10.1063/1.873437. eprint: https://doi.org/10.1063/1.873437. URL: https://doi.org/10.1063/1.873437.

[63] G. Pautasso et al. "On-line prediction and mitigation of disruptions in ASDEX Upgrade". In: *Nuclear Fusion* 42.1 (2002), p. 100. URL: http://stacks.iop.org/0029-5515/42/i=1/a=314.

[64] G Pautasso et al. "Disruption studies in ASDEX Upgrade in view of ITER". In: *Plasma Physics and Controlled Fusion* 51.12 (2009), p. 124056. URL: http://stacks.iop.org/0741-3335/51/i=12/a=124056.

[65] M. Persson and A. Bondeson. "Wall locking and density limit disruptions". In: *Nuclear Fusion* 29.6 (1989), p. 989. URL: http://stacks.iop.org/0029-5515/29/i=6/a=009.

[66] "Python least square fit". In: (). URL: https://github.com/scipy/scipy/blob/v.1.2.0/scipy/optimize/minpack.py#L504-L792.

[67] A. B. Rechester and M. N. Rosenbluth. "Electron Heat Transport in a Tokamak with Destroyed Magnetic Surfaces". In: *Phys. Rev. Lett.* 40 (1 Jan. 1978), pp. 38–41. DOI: 10.1103/PhysRevLett.40.38. URL: https://link.aps.org/doi/10.1103/PhysRevLett.40.38.

[68] D.C. Robinson and K. McGuire. "Magnetic islands and disruptions in the TOSCA tokamak". In: *Nuclear Fusion* 19.1 (1979), p. 115. URL: http://stacks.iop.org/0029-5515/19/i=1/a=013.

[69] O. Sauter, C. Angioni, and Y. R. Lin-Liu. "Erratum: Neoclassical conductivity and bootstrap current formulas for general axisymmetric equilibria and arbitrary collisionality regime] [Phys. Plasmas 6, 2834 (1999)]". In: *Physics of Plasmas* 9.12 (2002), pp. 5140–5140. DOI: 10.1063/1.1517052. eprint: https://doi.org/10.1063/1.1517052. URL: https://doi.org/10.1063/1.1517052.

[70] O. Sauter, C. Angioni, and Y. R. Lin-Liu. "Neoclassical conductivity and bootstrap current formulas for general axisymmetric equilibria and arbitrary collisionality regime". In: *Physics of Plasmas* 6.7 (1999), pp. 2834–2839. DOI: 10.1063/1.873240. eprint: https://doi.org/10.1063/1.873240. URL: https://doi.org/10.1063/1.873240. Erratum: [69].

[71] Dalton Schnack. *Lectures in Magnetohydrodynamics*. Springer-Verlag Berlin Heidelberg, 2009. ISBN: 978-3-642-00687-6. DOI: 10.1007/978-3-642-00688-3.

[72] V. D. Shafranov. "Plasma Equilibrium in a Magnetic Field". In: *Reviews of Plasma Physics* 2 (1966), p. 103.

[73] V. D. Shafranov. "The stability of a cylindrical gaseous conductor in a magnetic field". In: *The Soviet Journal of Atomic Energy* 1.5 (Oct. 1956), pp. 709–713. ISSN: 1573-8205. DOI: 10.1007/BF01480907. URL: https://doi.org/10.1007/BF01480907.

[74] U.A. Sheikh et al. "Disruption avoidance through the prevention of NTM destabilization in TCV". In: *Nuclear Fusion* 58.10 (2018), p. 106026. URL: http://stacks.iop.org/0029-5515/58/i=10/a=106026.

[75] E. J. Strait et al. "Chapter 2: Magnetic Diagnostics". In: *Fusion Science and Technology* 53.2 (2008), pp. 304–334. DOI: 10.13182/FST08-A1674. eprint: https://doi.org/10.13182/FST08-A1674. URL: https://doi.org/10.13182/FST08-A1674.

[76] H. R. STRAUSS. "Reduced MHD in nearly potential magnetic fields". In: *Journal of Plasma Physics* 57.1 (1997), p. 83 V87. URL: https://www.cambridge.org/core/journals/journal-of-plasma-physics/article/reduced-mhd-in-nearly-potential-magnetic-fields/310B568A8C0B85732E99C89D7941D7E8/share/93ee83c05f276fd05af82a924871fca900e97cb6.

[77] H. R. Strauss. "Nonlinear, three-dimensional magnetohydrodynamics of noncircular tokamaks". In: *The Physics of Fluids* 19.1 (1976), pp. 134–140. DOI: 10.1063/1.861310. eprint: https://aip.scitation.org/doi/pdf/10.1063/1.861310. URL: https://aip.scitation.org/doi/abs/10.1063/1.861310.

[78] R. Sweeney et al. "Relationship between locked modes and thermal quenches in DIII-D". In: *Nuclear Fusion* 58.5 (2018), p. 056022. URL: http://stacks.iop.org/0029-5515/58/i=5/a=056022.

[79] R. Sweeney et al. "Statistical analysis of m / n $= 2/1$ locked and quasi-stationary modes with rotating precursors at DIII-D". In: *Nuclear Fusion* 57.1 (2017), p. 016019. URL: http://stacks.iop.org/0029-5515/57/i=1/a=016019.

[80] Ryan Sweeney. Private communication. Jan. 2019.

[81] A. Sykes and J. A. Wesson. "Major Disruptions in Tokamaks". In: *Phys. Rev. Lett.* 44 (18 1980), pp. 1215–1218. DOI: 10.1103/PhysRevLett.44.1215. URL: https://link.aps.org/doi/10.1103/PhysRevLett.44.1215.

[82] P. L. Taylor et al. "Disruption mitigation studies in DIII-D". In: *Physics of Plasmas* 6.5 (1999), pp. 1872–1879. DOI: 10.1063/1.873445. eprint: https://doi.org/10.1063/1.873445. URL: https://doi.org/10.1063/1.873445.

[83] Equipe TFR. "Tokamak plasma diagnostics". In: *Nuclear Fusion* 18.5 (1978), p. 647. URL: http://stacks.iop.org/0029-5515/18/i=5/a=004.

[84] Stefan Vorbrugg. Private communication. Mar. 2019.

[85] P. C. de Vries et al. "Requirements for Triggering the ITER Disruption Mitigation System". In: *Fusion Science and Technology* 69.2 (2016), pp. 471–484. DOI: 10.13182/FST15-176. eprint: https://doi.org/10.13182/FST15-176. URL: https://doi.org/10.13182/FST15-176.

[86] P.C. de Vries et al. "Scaling of the MHD perturbation amplitude required to trigger a disruption and predictions for ITER". In: *Nuclear Fusion* 56.2 (2016), p. 026007. URL: http://stacks.iop.org/0029-5515/56/i=2/a=026007.

[87] C. F. v. Weizsäcker. "Zur Theorie der Kernmassen". In: *Zeitschrift für Physik* 96.7 (July 1935), pp. 431–458. ISSN: 0044-3328. DOI: 10.1007/BF01337700. URL: https://doi.org/10.1007/BF01337700.

[88] J.A. Wesson. "Hydromagnetic stability of tokamaks". In: *Nuclear Fusion* 18.1 (1978), p. 87. URL: http://stacks.iop.org/0029-5515/18/i=1/a=010.

[89] J.A. Wesson et al. "Disruptions in JET". In: *Nuclear Fusion* 29.4 (1989), p. 641. URL: http://stacks.iop.org/0029-5515/29/i=4/a=009.

[90] John Wesson. *Tokamaks*. Clarendon Press, Oxford, 2004. ISBN: 978-0198509226.

[91] R. B. White, D. A. Monticello, and M. N. Rosenbluth. "Simulation of Large Magnetic Islands: A Possible Mechanism for a Major Tokamak Disruption". In: *Phys. Rev. Lett.* 39 (25 Dec. 1977), pp. 1618–1621. DOI: 10.1103/PhysRevLett.39.1618. URL: https://link.aps.org/doi/10.1103/PhysRevLett.39.1618.

A. Coordinates

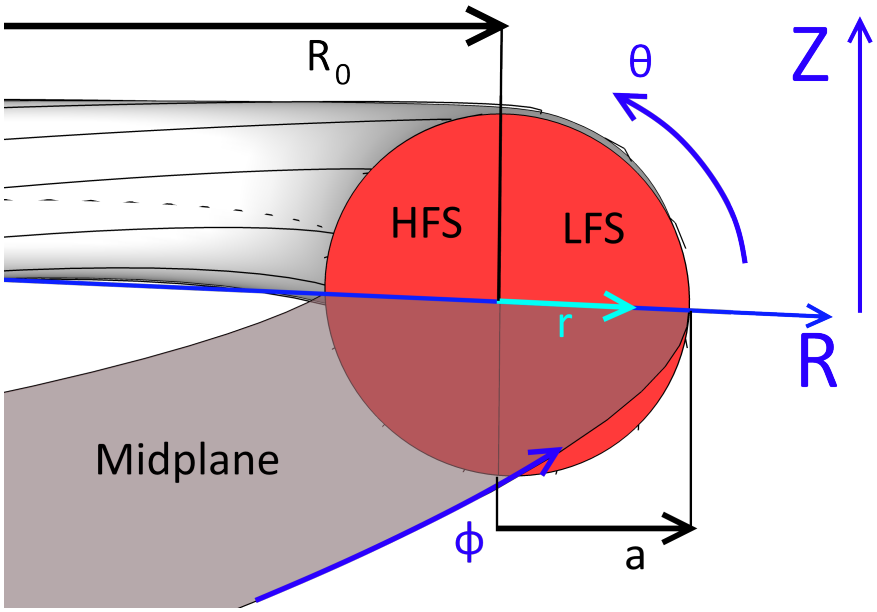

Figure 35: Major radius R_0 and Coordinate R are measured from the torus axis. a: minor radius. HFS: High field side. LFS: low field side.

An important definition is the normalized flux Ψ_N with Ψ_{sep} and Ψ_{axis} measured at the seperatrix respective magnetic axis:

$$\Psi_N = \frac{\Psi - \Psi_{\text{axis}}}{\Psi_{\text{sep}} - \Psi_{\text{axis}}} \tag{A.1}$$

Erklärung

Ich versichere hiermit, dass ich die von mir eingereichte Abschlussarbeit selbstständig verfasst und keine anderen als die angegebenen Quellen und Hilfsmittel benutzt habe.

München, der 15. März 2019